

Contacting Magnetic Nano-Objects for Quantum Transport Measurements

Bras, T.T.

DOI

[10.4233/uuid:925bc885-6967-422e-94fb-edf5c80edaff](https://doi.org/10.4233/uuid:925bc885-6967-422e-94fb-edf5c80edaff)

Publication date

2025

Document Version

Final published version

Citation (APA)

Bras, T. T. (2025). *Contacting Magnetic Nano-Objects for Quantum Transport Measurements*. [Dissertation (TU Delft), Delft University of Technology]. <https://doi.org/10.4233/uuid:925bc885-6967-422e-94fb-edf5c80edaff>

Important note

To cite this publication, please use the final published version (if applicable). Please check the document version above.

Copyright

Other than for strictly personal use, it is not permitted to download, forward or distribute the text or part of it, without the consent of the author(s) and/or copyright holder(s), unless the work is under an open content license such as Creative Commons.

Takedown policy

Please contact us and provide details if you believe this document breaches copyrights. We will remove access to the work immediately and investigate your claim.

Contacting Magnetic Nano-Objects for Quantum Transport Measurements

Contacting Magnetic Nano-Objects for Quantum Transport Measurements

Proefschrift

ter verkrijging van de graad van doctor
aan de Technische Universiteit Delft,
op gezag van de Rector Magnificus prof.dr.ir.T.H.J.J. van der Hagen,
voorzitter van het College voor Promoties,
in het openbaar te verdedigen op woensdag 18 juni 2025 om 12:30 uur

door

Tristan Thomas BRAS

Master of Science in Applied Physics,
Delft University of Technology, Delft, The Netherlands,
geboren te Amsterdam, Nederland.

Dit proefschrift is goedgekeurd door de promotoren.

Samenstelling promotiecommissie:

Rector Magnificus,
Prof. dr. ir. H. S. J. van der Zant,
Prof. dr. F. C. Grozema,

voorzitter
Technische Universiteit Delft, promotor
Technische Universiteit Delft, promotor

Onafhankelijke leden:

Prof. dr. L. D. A. Siebbeles,
Prof. dr. J. Ferrer Rodriguez,
Prof. dr. P. Gehring,
Prof. dr. T. Mallah,
Prof. dr. A. Mondal,
Prof. dr. A.F. Otte,

Technische Universiteit Delft
University of Oviedo, Spain
UC Louvain, Belgium
University Paris-Saclay, France
Indian Institute of Science Bengaluru, India
Technische Universiteit Delft (reserve)



Keywords: molecular electronics, single-molecule, mechanically-controlled break junction, spintronics, spin crossover, nanofabrication, quantum dot, nanoparticle

Printed by: Gildeprint B.V.

Front & Back: Front: Artistic impression of a nanoparticle contacted by two electrodes. Back: Artistic impression of a molecule contacted by two electrodes. Both images were generated using ChatGPT, model o3.

Copyright © 2025 by T. Bras

ISBN 978-94-6384-801-5

An electronic version of this dissertation is available at
<http://repository.tudelft.nl/>.

The associated experimental data and codes for this dissertation are available at
<https://doi.org/10.4121/14fb5699-879e-4632-b7cc-fcb04930d9f7>

Aan opa.

Contents

Summary	ix
Samenvatting	xi
1 Introduction	1
1.1 The need for energy-efficiency	1
1.2 The concept of spin	1
1.3 Spintronics: spin as the foundation of electronic devices	2
1.4 Nanoscale devices incorporating single molecules and nanoparticles	3
1.5 Thesis outline	5
References	7
2 Fabrication of Self-Aligned High Aspect-Ratio Nanogaps and Measurements on Gold Nanoparticles as a Reference System	11
2.1 Introduction	12
2.2 Device fabrication	14
2.2.1 Chip design and fabrication process	14
2.2.2 Encountered problems and the impact of different parameters on the fabrication process	17
2.3 Reference measurements	26
2.3.1 Trapping of a single gold nanoparticle	26
2.3.2 Low-temperature measurements	27
2.4 Conclusion and outlook	29
References	31
3 Trapping and Characterization of Prussian Blue Analogue Nanoparticles on Different Chip Geometries	33
3.1 Introduction	34
3.2 Experimental	37
3.3 Results	40
3.3.1 Room-temperature characterization and trapping	40
3.3.2 Low-temperature behaviour	42
3.4 Discussion	45
3.4.1 Coulomb blockade	45
3.4.2 Thermally activated transport	47
3.4.3 Reconciling the two observed behaviors	51

3.5	Conclusion	52
3.6	Appendix	53
3.6.1	Fabrication recipe point-contact nanogaps	53
	References	54
4	Electronic Characterization of a Mn(III) Spin Crossover Single-Molecule Junction	57
4.1	Introduction	58
4.2	Methods	60
4.3	Results and discussion	61
4.4	Conclusion and outlook	71
4.5	Appendix	72
4.5.1	Fast-breaking measurements on bare gold junctions	72
4.5.2	Fast-breaking measurements on the ligand	73
4.5.3	Shifting molecular orbitals as a function of electrode displacement and magnetic field	75
4.5.4	Examples of Fano fits on a Kondo resonance	77
4.5.5	Height of the Kondo peak in a magnetic field	78
	References	80
5	Mechanically Stable Kondo Resonance in an Organic Radical Molecular Junction	85
5.1	Introduction	86
5.2	Methods	87
5.3	Results and discussion	88
5.4	Conclusions	92
5.5	Appendix	93
5.5.1	Reference measurements on bare gold junctions	93
5.5.2	Two-dimensional histograms of <i>meta</i> -NNR at different bias voltages	94
5.5.3	Clustering of the <i>meta</i> -NNR fast-breaking measurements	94
5.5.4	Fits on Kondo peaks	95
5.5.5	Magnetic field measurements on <i>para</i> -NNR	97
5.5.6	Height of the Kondo resonances	98
	References	99
	Acknowledgements	103
	Curriculum Vitæ	107
	List of Publications	109

Summary

In this dissertation, we investigate charge transport in magnetic nano-objects. We use the mechanically-controlled break junction (MCBJ) technique to contact single molecules and use three different device geometries to optimize the process of contacting nanoparticles. We focus in particular on magnetic signatures in the quantum transport of these structures.

Chapter 1 gives a brief introduction to the field of spintronics. It provides a short history of the discovery of spin and highlights several important discoveries. Finally, it introduces the idea of nanoscale devices which incorporate nano-objects and describes the two techniques employed in the rest of this work.

In **chapter 2** we report on the optimization of the fabrication process of high aspect-ratio nanogaps. We investigate the impact of each parameter on the final structure of the nanogap. These nanogaps were then used to characterize charge transport in gold nanoparticles; a reference system for experiments on more complicated systems. We find that the current-voltage characteristics at cryogenic temperature can be described within the orthodox Coulomb blockade model.

Chapter 3 focuses on prussian blue analogue (PBA) nanoparticles, consisting of Co and Fe centers linked by cyanide groups. These particles are trapped in three different device geometries: point-contacts, high aspect-ratio contacts and overlapping contacts. We observe different transport characteristics for the different geometries. In the point-contacts we observe Coulomb blockade and see a gating effect. The other two geometries show an exponential dependence of the conductance as a function of temperature. We hypothesize that the different types of behavior are a result of how the nanoparticles are contacted by the electrodes.

In **chapter 4** we present experiments on a spin crossover (SCO) molecule with a Mn(III) center; a molecule which has two possible spin states: $S = 1$ or $S = 2$. We employ the MCBJ technique to perform fast-breaking measurements at room temperature, as well as to obtain current-voltage characteristics at cryogenic temperature. At room temperature, we compared the SCO molecule with its ligand (which lacks the Mn(III) center) and observed plateaus in the conductance as a function of electrode separation for the Mn SCO molecule, which is not the case for the ligand. At cryogenic temperature we observed transport phenomena which have been linked to a spin-state switch in SCO complexes in previous studies. We present and discuss each of these phenomena.

Chapter 5 reports on experiments on two open-shell organic radicals in an MCBJ setup: *para*-NNR and *meta*-NNR. At room temperature, we observe a plateau in the conductance for the *para* substituted molecule, which is only visible at higher bias voltages for the *meta* substituted molecule. At cryogenic temperature we found that *para*-NNR displays a Kondo resonance. Analysis of the Kondo peak reveals a constant width, independent of background conductance. This suggests an

asymmetric coupling between the molecule and the electrodes. Due to the absence of such a signature for ***meta*-NNR** we attribute this difference to the proximity of the radical group to the anchoring group in the case of ***para*-NNR**.

Samenvatting

In dit proefschrift onderzoeken we ladingstransport in magnetische nano-objecten. We gebruiken de mechanisch regelbare breekjunctie (MCBJ) techniek om individuele moleculen te contacteren en maken gebruik van drie verschillende devicegeometrieën om het contacteren van nanodeeltjes te optimaliseren. We richten ons in het bijzonder op magnetische signaturen in het kwantumtransport van deze structuren.

Hoofdstuk 1 geeft een korte introductie tot het vakgebied van spintronica. Het geeft een beknopte geschiedenis van de ontdekking van spin en belicht verschillende belangrijke ontdekkingen. Tot slot introduceert het het idee van nanoschaalapparaten die nano-objecten bevatten en beschrijft het de twee technieken die in de rest van dit werk worden gebruikt.

In **hoofdstuk 2** rapporteren we de optimalisatie van het fabricageproces van nanogaps met een hoog aspect-ratio. We onderzoeken de impact van elke parameter op de uiteindelijke structuur van de nanogap. Deze nanogaps werden vervolgens gebruikt om ladingstransport in goud nanodeeltjes te karakteriseren; een referentiesysteem voor experimenten op meer complexe systemen. We vinden dat de stroom-spanningskarakteristieken bij cryogene temperatuur beschreven kunnen worden binnen het orthodoxe Coulomb-blokkademodel.

Hoofdstuk 3 richt zich op pruisisch blauw-analoog (PBA) nanodeeltjes, bestaande uit Co- en Fe-centra die verbonden zijn door cyanidegroepen. Deze deeltjes worden gevangen in drie verschillende devicegeometrieën: puntcontacten, contacten met hoge aspect-ratio en overlappende contacten. We observeren verschillende transportkenmerken voor de verschillende geometrieën. In de puntcontacten observeren we Coulomb-blokkade en zien we een gating effect. De andere twee geometrieën vertonen een exponentiële afhankelijkheid van de geleiding als functie van de temperatuur. We veronderstellen dat de verschillende soorten gedrag het resultaat zijn van de manier waarop de nanodeeltjes worden gecontacteerd door de elektroden.

In **hoofdstuk 4** presenteren we experimenten op een spin crossover (SCO) molecuul met een Mn(III)-centrum; een molecuul met twee mogelijke spin-toestanden: $S = 1$ of $S = 2$. We gebruiken de MCBJ-techniek om snelle breukmetingen uit te voeren bij kamertemperatuur, en om stroom-spanningskarakteristieken te verkrijgen bij cryogene temperatuur. Bij kamertemperatuur vergeleken we het SCO molecuul met zijn ligand (dat het Mn-centrum mist) en observeerden we plateaus in de geleiding als functie van de afstand tussen de elektrodes voor het Mn(III) SCO-molecuul, wat niet het geval was voor het ligand. Bij cryogene temperatuur observeerden we transportverschijnselen die in eerdere studies zijn gekoppeld aan een transitie in de spin-toestand van het SCO-complex. We presenteren en bespreken elk van deze verschijnselen.

Hoofdstuk 5 rapporteert experimenten met twee open-shell organische radicalen

in een MCBJ opstelling: **para-NNR** en **meta-NNR**. Bij kamertemperatuur observeren we een plateau in de geleiding voor het *para*-gesubstitueerde molecuul, dat alleen zichtbaar is bij hogere voltages voor het **meta**-gesubstitueerde molecuul. Bij cryogene temperatuur vonden we dat **para-NNR** een Kondo resonantie vertoont. Analyse van de Kondo-piek toont een constante breedte, onafhankelijk van de achtergrondgeleiding. Dit suggereert een asymmetrische koppeling tussen het molecuul en de elektrodes. Door de afwezigheid van een dergelijke signatuur voor **meta-NNR** kennen we dit verschil toe aan de nabijheid van de radicale groep tot de verankeringsgroep in het geval van **para-NNR**.

1

Introduction

1.1. The need for energy-efficiency

Modern-day society critically relies on electronics, all of which require power to run. Not only do households have more devices on average than ever, with no signs of this increase stopping soon, but also chips are being pushed to be faster than ever. The modern world runs on data, which has to be transferred, processed and stored. The energy demand has become so large over the recent years that for example the energy grid in the Netherlands is running into problems [1]. Energy consumption is, however, not the only problem, in the push to accelerate processing speeds; the approach of the past 60 years has been to shrink the size of transistors such that more fit on a chip. With the process resolution currently being 3 nm [2], problems such as excessive heat generation arise. A solution which simultaneously allows for the amount of devices to grow, as well as chips to become even faster, is to find an alternative that is energy efficient. One such alternative would be to base devices on the manipulation of the spin state of electrons, instead of the absence and presence of charge.

1.2. The concept of spin

During the start of the 20th century, several phenomena were observed which could not be explained by classical physics. The famous Stern-Gerlach experiment, carried out in 1922, was the first evidence of electron spin. The experiment had the aim of determining whether an atom's magnetic moment was quantized or not. Classically, no quantization was expected: the atoms' magnetic moments should have a random orientation. When passed through an inhomogeneous magnetic field, each orientation would experience a different force and thus a different deflection, leading to a continuous distribution of deflections on the detector. However, quantum mechanically, the magnetic moments were predicted to be quantized. This quantization would lead to several discrete spots on the detector, as each value of the magnetic moment causes a specific degree of deflection. In the experiment, a

beam of silver atoms was sent through an inhomogeneous magnetic field, which led to two separate spots on the detector. This result proved that the magnetic moment, and thus the angular momentum was quantized.

The origin of this quantization was unclear: initially it was assumed that it was the orbital angular momentum which was quantized. However, this was later debunked when the same experiment was carried out with hydrogen atoms, where again two spots were observed, despite the atom possessing zero angular momentum. The degree of freedom which later came to be known as spin was first introduced by Wolfgang Pauli in 1924, who called it a 'two-valuedness not describable classically'. Initially, it was suggested that this two-valuedness could be due to an electron rotating around its own axis, producing an angular momentum. However, an electron having a finite radius instead of being a point particle, would mean that the surface of electrons moves faster than light, which violates the theory of relativity. When in 1926 a discrepancy between theory and experiment in the fine structure of the hydrogen spectrum was resolved by adding a relativistic correction to the spin-orbit coupling, known as the Thomas precession, electron spin came to be the accepted interpretation. Since its discovery, much research has been done into how to manipulate the spin degree of freedom and how it can be used in different types of applications. The field which aims to exploit the spin property for the encoding, processing and storing of information is called spintronics [3–7].

1.3. Spintronics: spin as the foundation of electronic devices

Traditional electronic devices rely on the manipulation of electric charge to encode, process and store information. The most important element, found in almost every electronic device, is the transistor [8], for which the Nobel prize in Physics of 1956 was awarded [9]. The transistor is a device which can switch and amplify electrical signals. It consists of three terminals: a source, a drain and a gate. When a sufficient voltage is applied to the gate, it allows for a current to flow from the source to the drain. This way a logical 0 and 1 can be encoded as respectively the absence and presence of a current. Furthermore, logical operations such as the OR, AND and NOT operations can be performed by a circuit consisting of two transistors. Currently, electronics are dominantly charge-based and are facing problems such as excessive power dissipation which hampers further miniaturization and efficiency. The field of spintronics aims to create devices which utilize the electron spin, a degree of freedom which requires much less energy to manipulate, and exists in structures at the atomic scale. Generally, the inception of the field is said to be the experiments on giant magnetoresistance, for which Albert Fert and Peter Grünberg were awarded the 2007 Nobel prize in Physics [10, 11]. By creating a sandwich of two ferromagnetic layers separated by a thin non-ferromagnetic layer, the orientation of the magnetization of the ferromagnetic layers is anti-parallel. In a magnetic field, the orientation becomes parallel, in which case an electron with a spin that is opposite to this orientation experiences a larger resistance than an electron with the same spin orientation when traveling through the structure. These experiments are

the first observations of spin-dependent transport. Shortly after these experiments, Supriyo Datta and Biswajit Das [12] published a paper in which they proposed a spin field-effect transistor: a device which manipulates electron spin through the application of an electric field. Since then, the field has matured significantly and many applications have been proposed: spin qubits for quantum computing, data storage, magnetoresistive random access memory and sensors [6, 13–16].

Using spin to encode information has a major advantage over using charge: it is a quantum property. Consider an electron, with a spin of either $\pm 1/2$. These states can be represented in bra-ket notation in the following manner: $|0\rangle = -1/2$ and $|1\rangle = +1/2$. In quantum mechanics, these are not the only two possible states, but combinations of these two are allowed as well. For example, $1/\sqrt{2}(|0\rangle + |1\rangle)$ is a valid state as well. Instead of the classical possibility of having only a zero and a one to encode and process information, now there is the possibility to have any combination of the two. Algorithms are being designed which exploit this property, leading to an exponential speedup for certain problems [17].

1.4. Nanoscale devices incorporating single molecules and nanoparticles

Another advantage of spin-based electronics is that spin is a property which exists at the nanoscale; single atoms, molecules and nanoparticles can have a net magnetic moment which can be manipulated. The intrinsically small size provides a natural way to create devices with a large amount of functional components, such as processing units, through a bottom-up approach, where a chip is built from the ground up by putting together billions of these structures.

However, incorporating spin into actual electronic devices is not easy [18]. One of the main challenges lies within the stability; at room temperature the available thermal energy is large enough to facilitate random spin-flips. Not only this, when placing these systems close together, they interact, and may as a result change for example their spin in a random fashion. The most straightforward approach to increase the stability of nanoscale devices is by reducing the temperature to a few degrees Kelvin. At this temperature the so-called spin coherence time, the time in which the spin state is predictable, is long enough to perform measurements.

In order to study molecules and nanoparticles which possess a net magnetic moment, several methods exist. In this thesis, we focus on the electronic transport of spin systems; hence a device geometry is required with at least two electrodes: one electrode to source a voltage or current and one electrode to read the resulting current or voltage. A third electrode can be added to act as a gate, changing the electrostatic potential of the molecule or particle with respect to that of the electrodes. For molecules, the distance between these electrodes should be of the order of 1 nm, whereas for nanoparticles the distance between the electrodes needs to be fine-tuned to the diameter of the particle, which can be of the order of 10-100 nm. We briefly explain the techniques which are used in this thesis: nanogaps and mechanically-controlled break junctions (MCBJs).

Nanogaps

For the study of nanoparticles we use a so-called nanogap: a device which consists of two electrodes separated by a gap with a size that is slightly smaller than the diameter of the nanoparticles under study. Not only the distance between the electrodes, but also the width and material of the electrodes are important. Wider nanogaps facilitate easier contacting of nano-objects through their larger contact area, whereas thinner, more point-like contacts are easier to fabricate with smaller gap sizes and are better suited for measurements incorporating a gate electrode due to their limited screening of the electric field [19]. For the fabrication of wider nanogaps with small gap sizes, special techniques are required such as creating a self-aligning physical mask through the oxidation of a Cr layer [20]. The material used for the electrodes depends on the nature of the nanoparticles that are being investigated. The most commonly used metal for the electrodes is gold, due to its excellent electrical conductivity and its resistance to oxidation. However, occasionally the particles have undesirable interactions with gold and merit the use of other noble metals such as platinum or palladium. In these devices, it is possible to shift the electrostatic potential of the nanoparticle either through the presence of a local gate electrode, or through applying a voltage to the back plane of the chip, which consists of heavily doped Si. The nanogap geometry makes this technology scalable and is therefore close to a real-world integrated chip.

Once proper nanogaps are fabricated, the nanoparticles have to be trapped. Unfortunately, due to their size, it is impossible to pick one up and place it inside an empty nanogap. Instead, we have to rely on chance: a suspension is made of the nanoparticles and this suspension is then either drop cast on the chip or the chip is submerged in the suspension, after which the chip is left to dry. By measuring a current-voltage (IV) characteristic of each nanogap before adding the nanoparticles and after doing so, we can detect the trapping of a particle: if the nanogap does not contain a particle, there should be no current flowing whereas if a particle has been trapped, there is a current. However, from this alone it is not possible to distinguish between a gap containing a single nanoparticle and a gap containing multiple. To confirm whether we trapped and measured a single particle, we need to look at its quantum transport characteristics or attempt to image the gap in the scanning electron microscope (SEM).

Mechanically-controlled break junctions

Mechanically-controlled break junctions (MCBJs) are used to investigate molecules [21–25]. This method uses a chip which consists of a phosphorous bronze substrate, coated with an electrically insulating poly-imide layer on top of which gold bridges are patterned using electron beam lithography. By fixating the sides of the chip, it can be bent by pushing in the middle with a rod. By bending the substrate, the gold bridges are stretched and eventually break. Gold is a malleable metal and as a result the bridges can be repaired by reversing the bending and pushing the ruptured ends into each other. The pushing rod is driven by a motor controlling a differential screw, resulting in micrometer precision. The MCBJ is designed in such

a way that this micrometer control translates to a sub-Angstrom precision over the separation of the gold bridge. In an MCBJ setup, either the conductance is measured as a function of separating the gold contacts (called a breaking trace), or IV characteristics are recorded. The MCBJ can be used at room-temperature (RT), together with a piezo element which can break and make the junction rapidly, to obtain large datasets and perform a statistical analysis. But the MCBJ can also be used at cryogenic temperature (CT), where the junction lifetimes are on the order of days due to the exceptional mechanical stability. This allows for the systematic study of IV characteristics, as well as the probing of vibrational modes through inelastic tunneling spectroscopy. The integration of a gate electrode to control the charge state has been demonstrated but is difficult because of the bending of the substrate [26]. It is important to note that there is no control over how a molecule is contacted; many different configurations of the molecule inside the junction exist, leading to different transport behaviors [27].

Molecules have been demonstrated to behave as for example rectifiers [28, 29], sensors [30, 31], transistors [32, 33] and memristors [34]. In this thesis, we focus on molecules which have a net magnetic moment and therefore exhibit spin-related behavior such as the Kondo effect [35, 36] and spin-state switching [37–39]. This is achieved by using either radicals, molecules with at least one unpaired electron, or using molecules containing a metal ion such as Fe(II) or Mn(III). In addition, these molecules are usually designed to possess so-called anchoring groups: a group which facilitates the binding of the molecule to the gold electrodes, either covalently or datively depending on the type of anchoring group [40]. The anchoring group also influences the overall molecular conductance [41, 42].

1.5. Thesis outline

This thesis investigates electronic transport in nano-objects which possess a net magnetic moment. These systems are either molecules or nanoparticles. The main objective of this work is to trap the particles and molecules to determine how the electron transport is influenced by the spin property of these objects, as well as to establish methods with which we can control either the spin-state or the way in which transport occurs. Measurements are performed on spin-crossover systems. These have two spin states between which can be switched by external stimuli such as light, pressure, temperature and electric field. Although many studies cover the properties and behavior of such materials in bulk systems, little has been done on the nanoparticle and molecular scale. The main goal here was to demonstrate the integration of these objects into devices and to drive the switch in spin-state with electric field, temperature or light. Finally, an organic radical, a molecule with a net magnetic moment, molecular system was investigated. We study the effect of quantum interference in the backbone on the overall transport properties by comparing two molecules.

This dissertation is structured as follows: in chapter 2 we discuss the fabrication process of high aspect-ratio nanogaps, a process which did yield 10-15 nm nanogaps over a width of 1 μm in the past but reproducing it turned out to be challenging. We change parameters in every step of the fabrication process and discuss the

1

impact of those parameters. We also trap gold nanoparticles in 25 nm gaps and characterize their electronic transport properties. In chapter 3 the electronic transport of 15 nm Prussian blue analogue nanoparticles is studied using three different nanogap designs. In chapter 4, single-molecule measurements are carried out in a mechanically-controlled break junction on a Mn complex. The molecule is expected to exhibit a switch in spin state and we aim to observe this switch in the electronic transport features. Finally, in chapter 5 we investigate how quantum interference in the molecular backbone affects the spin-related electronic transport in an organic radical.

References

- [1] Rijksoverheid, *Kabinet neemt maatregelen tegen vol elektriciteitsnet*, (2023).
- [2] TSMC, *3 nm Technology*, (2022).
- [3] S. A. Wolf, D. D. Awschalom, R. A. Buhrman, J. M. Daughton, S. von Molnár, M. L. Roukes, A. Y. Chtchelkanova, and D. M. Treger, *Spintronics: A Spin-Based Electronics Vision for the Future*, *Science* **294**, 1488 (2001).
- [4] I. Žutić, J. Fabian, and S. Das Sarma, *Spintronics: Fundamentals and applications*, *Reviews of Modern Physics* **76**, 323 (2004).
- [5] S. Bader and S. Parkin, *Spintronics*, *Annual Review of Condensed Matter Physics* **1**, 71 (2010).
- [6] A. Hirohata, K. Yamada, Y. Nakatani, I.-L. Prejbeanu, B. Diény, P. Pirro, and B. Hillebrands, *Review on spintronics: Principles and device applications*, *Journal of Magnetism and Magnetic Materials* **509**, 166711 (2020).
- [7] L. Bogani and W. Wernsdorfer, *Molecular spintronics using single-molecule magnets*, *Nature Materials* **7**, 179 (2008).
- [8] W. Brinkman, D. Haggan, and W. Troutman, *A history of the invention of the transistor and where it will lead us*, *IEEE Journal of Solid-State Circuits* **32**, 1858 (1997).
- [9] *1956 Nobel Prize in Physics*, *Physics Today* **10**, 16 (1957).
- [10] M. N. Baibich, J. M. Broto, A. Fert, F. N. Van Dau, F. Petroff, P. Etienne, G. Creuzet, A. Friederich, and J. Chazelas, *Giant Magnetoresistance of (001)Fe/(001)Cr Magnetic Superlattices*, *Physical Review Letters* **61**, 2472 (1988).
- [11] G. Binasch, P. Grünberg, F. Saurenbach, and W. Zinn, *Enhanced magnetoresistance in layered magnetic structures with antiferromagnetic interlayer exchange*, *Physical Review B* **39**, 4828 (1989).
- [12] S. Datta and B. Das, *Electronic analog of the electro-optic modulator*, *Applied Physics Letters* **56**, 665 (1990).
- [13] J. Puebla, J. Kim, K. Kondou, and Y. Otani, *Spintronic devices for energy-efficient data storage and energy harvesting*, *Communications Materials* **1**, 24 (2020).
- [14] V. Krizakova, M. Perumkunnil, S. Couet, P. Gambardella, and K. Garello, *Spin-orbit torque switching of magnetic tunnel junctions for memory applications*, *Journal of Magnetism and Magnetic Materials* **562**, 169692 (2022).
- [15] G. Burkard, T. D. Ladd, A. Pan, J. M. Nichol, and J. R. Petta, *Semiconductor spin qubits*, *Reviews of Modern Physics* **95**, 025003 (2023).

- [16] D. Loss and D. P. DiVincenzo, *Quantum computation with quantum dots*, *Physical Review A* **57**, 120 (1998).
- [17] A. Montanaro, *Quantum algorithms: an overview*, *npj Quantum Information* **2**, 15023 (2016).
- [18] D. D. Awschalom and M. E. Flatté, *Challenges for semiconductor spintronics*, *Nature Physics* **3**, 153 (2007).
- [19] S. S. Datta, D. R. Strachan, and A. T. C. Johnson, *Gate coupling to nanoscale electronics*, *Physical Review B* **79**, 205404 (2009).
- [20] A. Fursina, S. Lee, R. G. S. Sofin, I. V. Shvets, and D. Natelson, *Nanogaps with very large aspect ratios for electrical measurements*, *Applied Physics Letters* **92** (2008), 10.1063/1.2895644.
- [21] J. M. van Ruitenbeek, A. Alvarez, I. Piñeyro, C. Grahmann, P. Joyez, M. H. Devoret, D. Esteve, and C. Urbina, *Adjustable nanofabricated atomic size contacts*, *Review of Scientific Instruments* **67**, 108 (1996).
- [22] M. A. Reed, C. Zhou, C. J. Muller, T. P. Burgin, and J. M. Tour, *Conductance of a Molecular Junction*, *Science* **278**, 252 (1997).
- [23] C. A. Martin, R. H. M. Smit, R. van Egmond, H. S. J. van der Zant, and J. M. van Ruitenbeek, *A versatile low-temperature setup for the electrical characterization of single-molecule junctions*, *Review of Scientific Instruments* **82** (2011), 10.1063/1.3593100.
- [24] J. C. Cuevas and E. Scheer, *Molecular Electronics*, World Scientific Series in Nanoscience and Nanotechnology, Vol. 15 (WORLD SCIENTIFIC, 2017).
- [25] P. Gehring, J. M. Thijssen, and H. S. J. van der Zant, *Single-molecule quantum-transport phenomena in break junctions*, *Nature Reviews Physics* **1**, 381 (2019).
- [26] C. A. Martin, J. M. van Ruitenbeek, and H. S. J. van der Zant, *Sandwich-type gated mechanical break junctions*, *Nanotechnology* **21**, 265201 (2010).
- [27] L. Venkataraman, J. E. Klare, C. Nuckolls, M. S. Hybertsen, and M. L. Steigerwald, *Dependence of single-molecule junction conductance on molecular conformation*, *Nature* **442**, 904 (2006).
- [28] M. Elbing, R. Ochs, M. Koentopp, M. Fischer, C. von Hänisch, F. Weigend, F. Evers, H. B. Weber, and M. Mayor, *A single-molecule diode*, *Proceedings of the National Academy of Sciences* **102**, 8815 (2005).
- [29] I. Díez-Pérez, J. Hihath, Y. Lee, L. Yu, L. Adamska, M. A. Kozhushner, I. I. Oleynik, and N. Tao, *Rectification and stability of a single molecular diode with controlled orientation*, *Nature Chemistry* **1**, 635 (2009).

- [30] M. Tsutsui, S. Rahong, Y. Iizumi, T. Okazaki, M. Taniguchi, and T. Kawai, *Single-molecule sensing electrode embedded in-plane nanopore*, *Scientific Reports* **1**, 46 (2011).
- [31] G. Czap, P. J. Wagner, F. Xue, L. Gu, J. Li, J. Yao, R. Wu, and W. Ho, *Probing and imaging spin interactions with a magnetic single-molecule sensor*, *Science* **364**, 670 (2019).
- [32] J. Park, A. N. Pasupathy, J. I. Goldsmith, C. Chang, Y. Yaish, J. R. Petta, M. Rinkoski, J. P. Sethna, H. D. Abruña, P. L. McEuen, and D. C. Ralph, *Coulomb blockade and the Kondo effect in single-atom transistors*, *Nature* **417**, 722 (2002).
- [33] S. Kubatkin, A. Danilov, M. Hjort, J. Cornil, J.-L. Brédas, N. Stuhr-Hansen, P. Hedegård, and T. Bjørnholm, *Single-electron transistor of a single organic molecule with access to several redox states*, *Nature* **425**, 698 (2003).
- [34] T. Miyamachi, M. Gruber, V. Davesne, M. Bowen, S. Boukari, L. Joly, F. Scheurer, G. Rogez, T. K. Yamada, P. Ohresser, E. Beaurepaire, and W. Wulfhchel, *Robust spin crossover and memristance across a single molecule*, *Nature Communications* **3**, 938 (2012).
- [35] J. J. Parks, A. R. Champagne, T. A. Costi, W. W. Shum, A. N. Pasupathy, E. Neuscamman, S. Flores-Torres, P. S. Cornaglia, A. A. Aligia, C. A. Balseiro, G. K.-L. Chan, H. D. Abruña, and D. C. Ralph, *Mechanical Control of Spin States in Spin-1 Molecules and the Underscreened Kondo Effect*, *Science* **328**, 1370 (2010).
- [36] G. Mitra, J. Z. Low, S. Wei, K. R. Francisco, M. Deffner, C. Herrmann, L. M. Campos, and E. Scheer, *Interplay between Magnetoresistance and Kondo Resonance in Radical Single-Molecule Junctions*, *Nano Letters* **22**, 5773 (2022).
- [37] G. D. Harzmann, R. Frisenda, H. S. J. van der Zant, and M. Mayor, *Single-Molecule Spin Switch Based on Voltage-Triggered Distortion of the Coordination Sphere*, *Angewandte Chemie International Edition* **54**, 13425 (2015).
- [38] R. Frisenda, G. D. Harzmann, J. A. Celis Gil, J. M. Thijssen, M. Mayor, and H. S. J. van der Zant, *Stretching-Induced Conductance Increase in a Spin-Crossover Molecule*, *Nano Letters* **16**, 4733 (2016).
- [39] M. Ormaza, P. Abufager, B. Verlhac, N. Bachellier, M.-L. Bocquet, N. Lorente, and L. Limot, *Controlled spin switching in a metallocene molecular junction*, *Nature Communications* **8**, 1974 (2017).
- [40] L. J. O'Driscoll and M. R. Bryce, *A review of oligo(arylene ethynylene) derivatives in molecular junctions*, *Nanoscale* **13**, 10668 (2021).

- [41] W. Hong, D. Z. Manrique, P. Moreno-García, M. Gulcur, A. Mishchenko, C. J. Lambert, M. R. Bryce, and T. Wandlowski, *Single Molecular Conductance of Tolanes: Experimental and Theoretical Study on the Junction Evolution Dependent on the Anchoring Group*, *Journal of the American Chemical Society* **134**, 2292 (2012).
- [42] R. Frisenda, S. Tarkuç, E. Galán, M. L. Perrin, R. Eelkema, F. C. Grozema, and H. S. J. van der Zant, *Electrical properties and mechanical stability of anchoring groups for single-molecule electronics*, *Beilstein Journal of Nanotechnology* **6**, 1558 (2015).

2

Fabrication of Self-Aligned High Aspect-Ratio Nanogaps and Measurements on Gold Nanoparticles as a Reference System

In physics, you don't have to go around making trouble for yourself – nature does it for you.

Frank Wilczek

Abstract

A previously working fabrication recipe for high aspect-ratio nanogaps was found to produce gaps that were 30 nm with rough edges as opposed to the desired 10-15 nm with smooth edges. In this chapter we explore the impact of each step of the fabrication process on the final result with the goal of fabricating 10-15 nm gaps with a width of 1 μm . The fabrication process consists of the patterning of a central main electrode which is topped by a chromium layer. The oxidation of the chromium layer forms a self-aligning physical mask for the second step. Changes were made in the evaporation system, the thickness of the metal layers, the evaporation rates of the metal layers, the length of the oxygen plasma, the duration and temperature of the wet etching and the height difference between the ME and the AE. None

of these changes resulted in the desired nanogaps, however it was found that the evaporation system had a large impact on the size of the nanogaps. Using another system resulted in gaps which were 10-15 nm, but filled with particles.

A batch with nanogaps of around 25 nm was obtained and used for the measurement of 30 nm gold nanoparticles. These measurements serve as a reference for future experiments on more complex systems. Comparing the current-voltage (IV) characteristics before and after deposition of a solution containing the nanoparticles, we found that two junctions displayed a sizable current after deposition while they displayed no current before deposition. These junctions were cooled down to 10 K in a cryo-free probestation and IVs were found to display Coulomb blockade-like behavior. To confirm this, the orthodox Coulomb blockade theory model was fitted to these IVs and good correspondence was found. After the measurements the junctions were imaged in a scanning electron microscope and for sample 1 we observed a single nanoparticle trapped between the electrodes, which provides visual confirmation of our measurements.

2.1. Introduction

Chips are embedded in our society like never before. Every 'smart' device contains a chip which is needed to process and store information. The demand for chips is increasing and is expected to keep increasing. All these devices use power, leading to overcrowded electricity networks and a rapidly rising electricity usage. Additionally, heating problems are preventing chip manufacturers from putting more transistors on a chip. Therefore, low-power alternatives are an important area of research. One such alternative is the Single Electron Transistor (SET), first demonstrated by Likharev and Averin [1] in 1986. A SET consists of three electrodes and a conductive island. The island is isolated by the electrodes through tunnel junctions, each characterized by a capacitance C , and a resistance, R . Electron transport in a SET is dominated by single electron tunneling events, as long as the total resistance is much larger than the quantum resistance $R_q = h/2e^2 \approx 12.9$ k Ω where h is Planck's constant and e the elementary charge, and the charging energy of the island ($e^2/2C$) is a few times larger than the thermal energy [2]. Nanoparticles can be used as the island to form a SET. A metallic particle such as a gold nanoparticle will create a relatively simple SET, displaying Coulomb Blockade (CB) [3]. However, properties can be added to the SET by using for example spin crossover (SCO) nanoparticles, which can be switched between a low-spin and a high-spin ground state [4].

To facilitate measurements on nanoparticles, a gap between the two conducting electrodes is needed to trap them. This gap should be smaller than the diameter of the particle, which is generally on the order of 10-100 nm. Especially for smaller particles, fabrication becomes non-trivial because effects such as the proximity effect in the electron beam lithography step make it impossible to directly define your structure [5]. In our case, trapping a nanoparticle is a random process: a droplet containing the nanoparticles is drop-cast on top of the structure and there is a

small chance a particle will end up in the nanogap. This trapping probability can be increased through for example dielectrophoresis [3], but the most straightforward method is through increasing the area of the nanogap. Our ideal device has nanogaps of 10-15 nm, with a large area to trap the particles on. Such a design was made in 2008 by A. Fursina *et al.* [6], where oxidized chrome is used as a physical, self-aligning mask to define high aspect-ratio nanogaps with a gap size of 10 - 100 nm over a width of 1 μm . This design was later further optimized in the van der Zant group at the Delft University of Technology for this type of measurements by J. Houtman, who managed to achieve nanogaps with an average gap size of 13 nm with a yield of 90% [7]. Finally, J.A. Labra-Muñoz [8] implemented a local gate in this design.

This wide-gap design has also been used by F. Prins *et al.* [4] in their study on electronic transport measurements of a SCO nanoparticle where they observe the switching of the spin state through the conductance. One major difference in our device is the electrode material; we cannot use gold due to the nature of the nanoparticles we want to measure. These particles are so-called Prussian blue analogues (PBAs), which contain cyanide. Previous attempts by J. Houtman [7] to measure these particles with gold electrodes resulted in the etching of the electrodes through the formation of the cyano-complex $\text{Au}(\text{CN})_2$ [9]. Therefore, platinum is used as electrode material instead. However, following the fabrication process documented by J. Houtman [7] yielded unsatisfying results; gap sizes were around 30 nm, electrode edges were rough and contaminations were observed. To obtain nanogaps of sufficient quality which are needed for measurements on the 15 nm PBAs presented in the next chapter, we explored the impact of changing the different parameters in the fabrication process on the final result.

Additionally, PBA nanoparticles are expected to display a spin transition under external stimuli such as light, temperature and magnetic field, as well as an accompanying charge transfer. To properly investigate how these phenomena affect the electrical transport of the system, we need a reference system. To this end, 30 nm gold nanoparticles were trapped on chips which displayed gaps that were around 25 nm and electronic transport measurements were performed at both room- and low-temperature. The current-voltage (IV) characteristics at low temperatures were fitted to the Coulomb blockade model.

2.2. Device fabrication

2.2.1. Chip design and fabrication process

An overview of the device layout is shown in figure 2.1. The Main Electrode (ME) is shown in blue and the Auxiliary Electrodes (AE) are shown in red. At the interface between the ME and AE are nanogaps. A Local Gate (LG) is located underneath the nanogaps (green), which allows for the gating of nanoparticles inside the nanogaps.

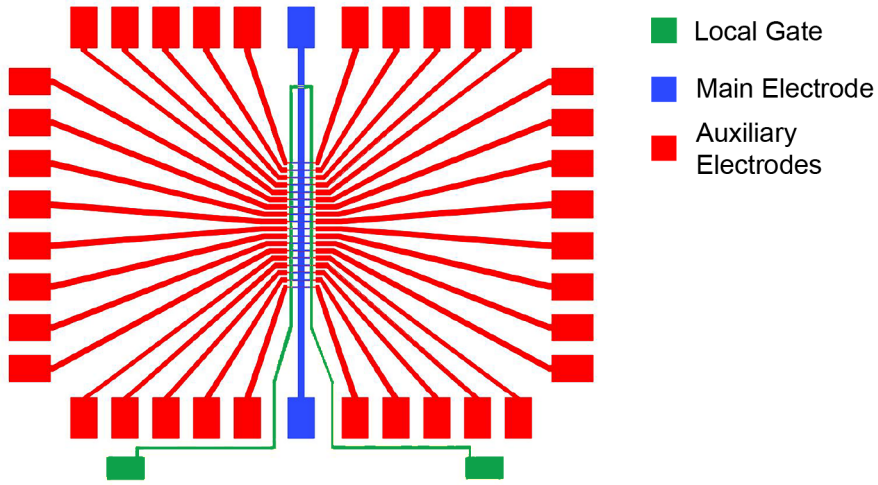


Figure 2.1: Overview of the device design. Green is the gate electrode, blue is the main electrode and red are the auxiliary electrodes.

The fabrication process to obtain these devices, which have been used in previous studies in the van der Zant group at the Delft University of Technology, is shown schematically in figure 2.2. A 19x19 mm, doped Si/SiO₂ substrate is first cleaned in fuming nitric acid (figure 2.2a). The cleaned substrate is either used immediately or stored in a desiccator for later use. If the substrate is stored in a desiccator, it is exposed to an oxygen plasma before spincoating e-beam resist. A layer of CSAR 4% (AR-P 6200.04) is spincoated at 4000 rpm and baked for 210 seconds at 180 °C (figure 2.2b). The resist is then exposed by the e-beam (Raith EBPG 5200 in the Kavli Nanolab). After exposure the pattern is developed by submerging the substrate in pentyl-acetate for 1 minute while gently agitating, followed by a descum in xylene for 5 seconds. The gate electrode (GE) is then evaporated by first evaporating a sticking layer of 3 nm titanium, followed by 12 nm platinum (figure 2.2c). The resist is stripped using AR 600-71, leaving only the GE (figure 2.2d). Atomic layer deposition (ALD) is performed to create a 22 nm thick layer of hafnium oxide (figure 2.2e).

Next, the Main Electrode (ME) is defined, following the same steps as before. Resist is spincoated, baked, exposed and developed. The electrode is made by evaporating 5 nm titanium, 25 nm platinum and 30 nm chrome after which lift-off is

performed (figure 2.2f). At the end of the day, the chip is put in a desiccator and left until the next morning. The chrome is then forcefully oxidized by exposing it to an oxygen plasma in the Tepla, created using a flow of 70 sccm O_2 and a power of 120 W for 3 minutes (figure 2.2g). The Auxiliary Electrodes are now patterned by again following the same steps: spincoating, baking, exposing, developing. This time a layer of 5 nm titanium and 20 nm platinum is evaporated, followed by a lift-off (figure 2.2h). At this point, the nanogaps are still covered by the oxidized chrome. This layer is removed by wet etching using TechniEtch Cr-01, which is a mixture of perchloric acid $HClO_4$ and ceric ammonium nitrate $(NH_4)_2[Ce(NO_3)_6]$ [10]. The chip is put in this chrome etchant for roughly 2 minutes during which it is lightly sonicated for 1 minute (figure 2.2i).

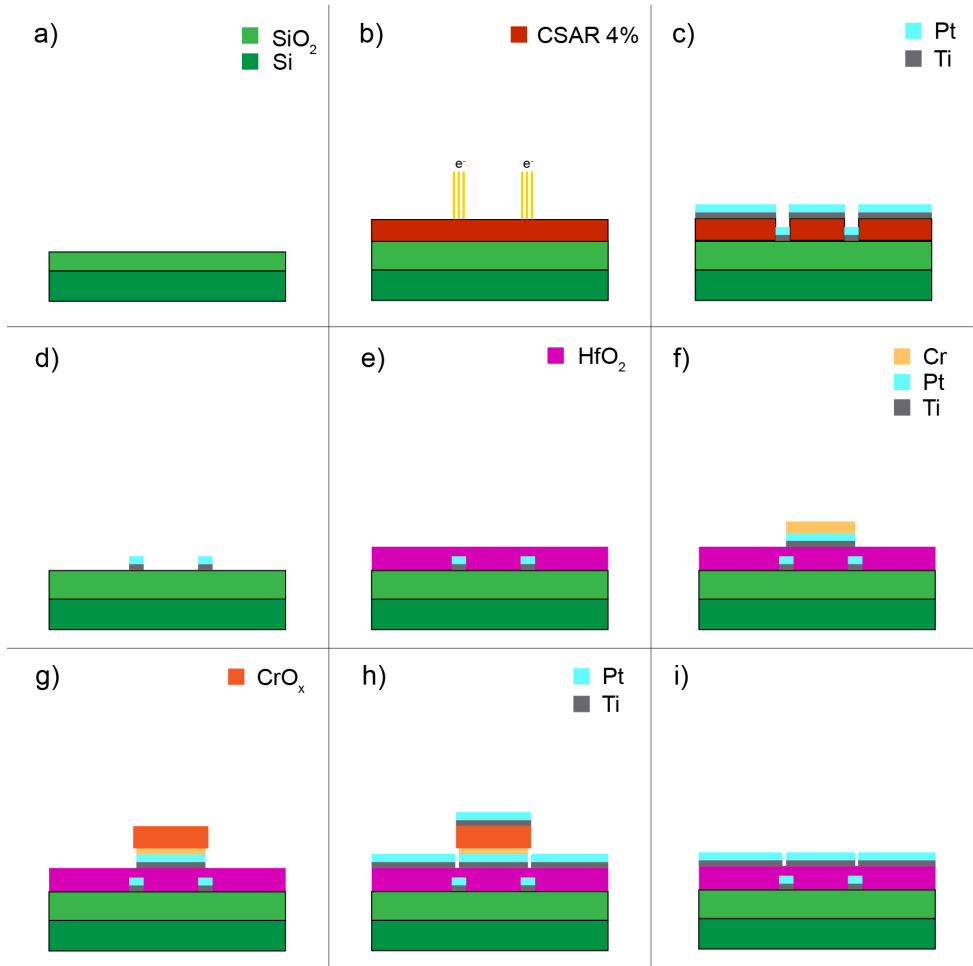


Figure 2.2: Schematic of the fabrication process (sideview). a) A 19 x 19 mm² silicon substrate with a 285 nm thick layer of silicon oxide which has been cleaned using fuming nitric acid. b) Spincoating and baking of a layer of CSAR 4% (AR-P 6200.04) e-beam resist, followed by e-beam exposure to define the gate electrode. c) Development in pentyl-acetate followed by a descum in xylene and evaporation of titanium (3 nm) and platinum (12 nm). d) Lift-off using AR 600-71. e) Atomic layer deposition of 22 nm of hafnium oxide. f) Definition of the main electrode by spincoating, baking, exposing, developing, evaporating 5 nm titanium, 25 nm platinum and 30 nm chromium, and lift-off. g) Oxidation of the chromium top layer by exposure to an oxygen plasma. h) Definition of the auxiliary electrodes by spincoating, baking, exposing, developing, evaporating 5 nm titanium and 15 nm platinum, and lift-off. i) Removal of the chrome and chrome oxide by wet etching using TechniEtch Cr-01.

2.2.2. Encountered problems and the impact of different parameters on the fabrication process

As mentioned in the introduction, following the recipe that J.A Labra-Muñoz used for her work, resulted in gaps of insufficient quality. Several problems were observed, illustrated with scanning electron microscopic (SEM) images in figure 2.3. This is somewhat surprising since the equipment and followed procedures have not changed. Apparently, uncontrolled parameters in the equipment or fabrication process are responsible for the low quality of the samples.

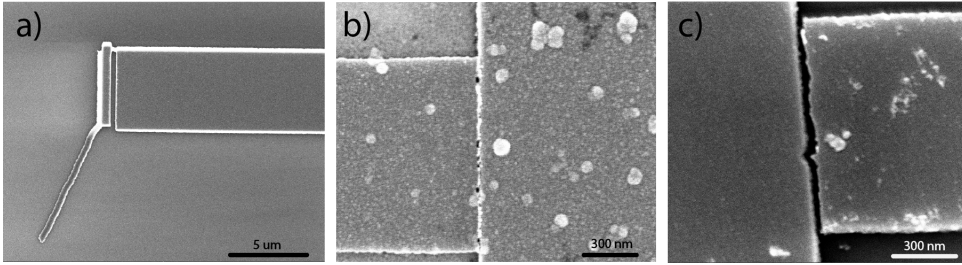


Figure 2.3: Scanning electron microscopic images showing different issues with the fabrication of the nanogaps. a) Tearing of the resist due to heat induced stress. b) Metal-like particles in the gap. c) Large gaps with rough edges.

In panel a, b and c three different problems are illustrated. In panel a, a chip is shown where only the ME was fabricated. The ME, which is the structure entering the picture from the right, displays broad, white edges. While the edges of a structure always appear bright in a SEM due to the edge effect [11], the edges in this case are very broad, indicating that the metal layer is not flat with a well-defined edge as expected. Additionally, separated from the ME we see an isolated structure. This structure has a broad edges which does not seem to match the structure itself, as well as an unwanted deposition in the form of a line going down and to the left from this isolated structure. This line suggests that either the resist has torn, opening a crevice where metal is deposited, or the resist below has cross-linked [12]. In the former case some process caused compressive stress in the resist layer resulting in a tear, in the latter case heating is the most likely culprit. A note should be made about the isolated structure, which is an artifact from a faulty ebeam pattern generator (EBPG).

In panel b we see a junction of a finalized chip where the gap size is around 15 nm, however, particles seem to be filling the gap between ME and AE. Measuring the current across this junction results in most cases in a short circuit, indicating that these particles are metallic in nature and bridge the two electrodes. The origin of these particles is unknown.

Finally, in panel c we see a junction of a finalized chip with a gap size of around 30 nm and rough electrode edges. Since the gaps are defined through the oxidation of the Cr layer on top of the ME, the cause of the large gap size is probably an excessive oxidation of the Cr. The edge roughness indicates that the oxidation of the Cr is inhomogeneous and needs to be more controlled.

To determine the cause of these problems and solve them, each parameter of the fabrication process was changed and its impact was investigated. Specifically, the parameters are: 1) the evaporation system, 2) the thickness of the Pt layer, 3) the thickness of the Cr layer, 4) the oxygen plasma duration, 5) the timing of the oxygen plasma, 6) the Cr etching, 7) the height difference between the ME and the AE and 8) the evaporation rate of the Cr. In the coming sections, SEM images are presented showcasing the impact of each parameter, followed by a short discussion.

Prior to the results that are presented below, several batches were fabricated using the recipe from J.A Labra-Muñoz [8]. Following this recipe resulted in severe problems related to excessive heating of the chip during evaporation, which turned out to be caused by a contaminated Pt crucible in the Temescal, which is an ebeam physical vapor deposition system. After this pocket was replaced, problems as depicted in figure 2.3a did not occur anymore, but the resulting junctions looked consistently as the one in panel c of the same figure. Therefore the problems depicted in panel a were most likely caused by excessive heating of the chip during evaporation.

Platinum is a relatively difficult metal to evaporate [13]. To investigate whether further reducing the heating of the chip during evaporation would increase the quality of the gaps we decided to reduce the thickness of the Pt layer by 5 nm for both the ME and the AE: from 25/20 nm to 20/15 nm. The results are shown in figure 2.4, with panel a showing a thickness of 25/20 nm and panel b showing the reduced thickness.

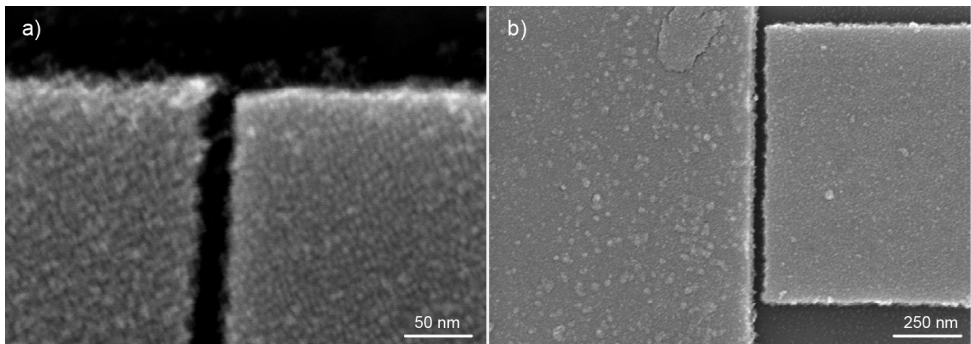


Figure 2.4: SEM images of chips fabricated with differing Pt thicknesses. a) A junction fabricated in the Temescal using 25 nm Pt for the main electrode and 20 nm Pt for the auxiliary electrode. b) A junction fabricated in the Temescal using 20 nm Pt for the main electrode and 15 nm Pt for the auxiliary electrode.

From the SEM images, no clear difference is observed; the gap size is still around 30 nm and the edges of the electrodes remain rough. Either the Pt thickness has no direct effect on the quality of the gap, or the effect of a 5 nm reduction is too small to observe. Due to lack of improvement, other evaporation systems were tested: the AJA-QT for Ti and Pt, and the AJA-MB for Cr. Because both systems

are required for the full fabrication process, we will refer to them as the AJAs from this point on. Initial tests using the AJAs produced nanogaps with a size of 5-15 nm, but with particles inside the gap as shown in figure 2.3b. However, due to the small gap size we decided to switch to the AJAs for the evaporation step and instead work on obtaining consistent gap sizes and removing the particles inside the gap.

Fursina *et al.* [6] report that the thickness of the Cr layer is the determining factor for the gap size when using oxidized chromium as a physical mask. Therefore the thickness of the Cr layer was varied between 20 and 35 nm with the goal of tuning the gap size. Figure 2.5 shows a representative gap for each thickness. No difference is observed; all gaps are approximately of the same size and have particles inside them. This is surprising because Fursina *et al.* [6] reported a gap size as large as 70 nm for a Cr thickness of 35 nm. The lack of any effect of the Cr thickness would indicate a lack of oxidation of the Cr layer, which is unexpected because chromium oxidizes in ambient conditions. Moreover, the oxygen plasma cleaning step before the fabrication of the AE should oxidize the Cr rapidly. J.Houtman reported in his thesis [7] that the addition of an oxygen plasma cleaning step decreased the gap size and improved the smoothness of the gap. He observed an upward curling of the ME at the edges as a result of the rapid oxidation of the Cr and argued that the resulting increased vertical space between the ME and AE and decreased horizontal extrusion of the Cr lead to the improved gap quality.

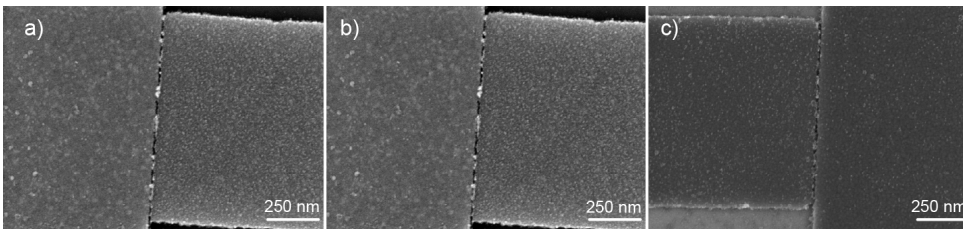


Figure 2.5: SEM images of chips with varying Cr thicknesses. a) A junction with a layer of 20 nm Cr. b) A junction with a layer of 25 nm Cr. c) A junction with a layer of 35 nm Cr.

In our process, the oxidation of the Cr layer is influenced by 3 steps: 1) the duration of the oxygen plasma, 2) whether the chip is exposed to an oxygen plasma at the end of the first day or at the start of the second day and 3) the resist baking step before the EBL exposure of the AE. The third step can only be changed by changing resist, but for example a double layer of polymethylmethacrylate (PMMA) and methylmethacrylate (MMA) requires baking at the same temperature, therefore the effect of the first two was investigated. The duration of the oxygen plasma was originally 10 minutes with a power of 120 W and a flow of 70 sccm and was used to remove organic residues. To investigate the effect of the oxygen plasma on the oxidation of the Cr and whether it is needed to remove organic contaminations, we fabricated the ME using no oxygen plasma, using a 3 minute plasma and using a 15 minute plasma. The results are shown in figure 2.6. First, the batch without

a plasma (panel a and b) displays protrusions at the intersection of the ME and the substrate. These protrusions are not present in panels c,d (3 minute plasma) and e,f (15 minute plasma), indicating that these protrusions are most likely resist residues which are removed in the plasma. This step is therefore essential and should not be omitted.

In the oxygen plasma, the surface chromium layer is expected to oxidize rapidly. How long is needed for the surface to completely oxidize is unknown but could have a large impact on the nanogaps. The original process by J. Houtman [7] used a 10 minute oxygen plasma, which was replicated in most of our batches. Here, we experimented with a plasma time of 3 minutes (panels c,d) and of 15 minutes (panels e,f). In both panels d and f a slight upward curling of the edge is present, which is the result of the oxidation of the Cr layer. No clear difference is observed, indicating that the oxidation takes place rapidly and has already taken place after 3 minutes of plasma. Surprising are the small structures lying on top of the ME at the edge, present in both panels d and f. These seem to be metallic, given their similar contrast as the electrode. Possible explanations for these structures could be a slight sidewall coverage during evaporation, resulting in collapsed metal structures after lift-off, or an inhomogeneous oxidation, causing a rough edge.

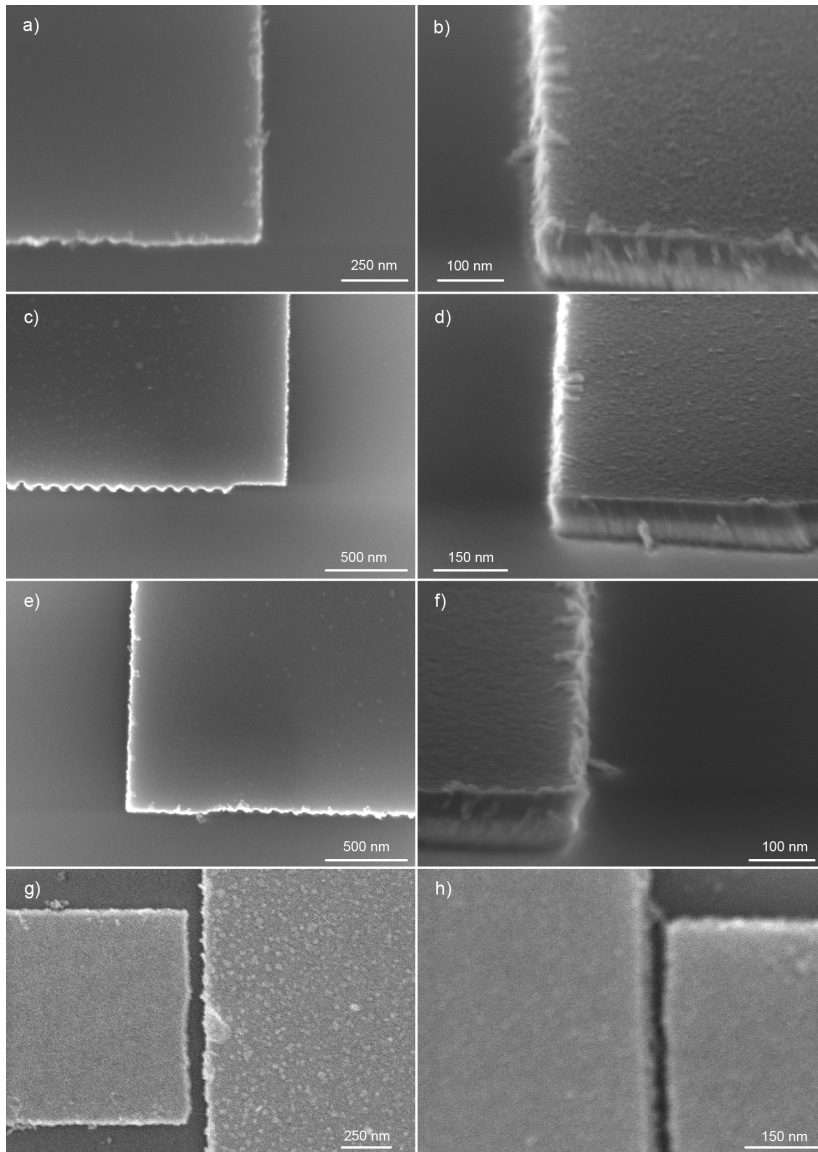


Figure 2.6: a,b) SEM images taken under an angle of the main electrode without exposure to an oxygen plasma. c,d) Top-view and view under an angle of a main electrode exposed to a 3 minute, 70 sccm, 120 W oxygen plasma. e,f) Top-view and view under an angle of a main electrode exposed to a 15 minute, 70 sccm, 120 W oxygen plasma. g) SEM image of a finalized junction where the oxygen plasma step was done immediately after finishing the main electrode. h) SEM image of a finalized junction where the oxygen plasma step was done before starting fabrication of the auxiliary electrode.

Not only the oxygen plasma has an impact on the oxidation of the chromium layer, but also the timing of the plasma: because the fabrication process of the ME and the AE spans two days, the oxygen plasma can either be done at the end of the first day, or at the start of the second day. In the former case, the oxygen plasma actively oxidizes the Cr layer and less oxidation in ambient conditions might take place, whereas in the latter case, the Cr layer first oxidizes passively in ambient conditions throughout the night, after which it is exposed to a plasma. Important in this regard is the fact that Cr is not expected to oxidize completely in ambient conditions, as for a complete oxidation a temperature of 300 °C is required [6, 14]. Results for the timing of the plasma are shown in figure 2.6 panels g (end of 1st day) and h (start of second day). Please note that these batches were fabricated using the Temescal for evaporation. The electrode roughness is higher for the chip which was exposed to the plasma on the 1st day. Moreover, the gap is slightly larger. We infer from this that the timing of the oxidation influences the quality of the gaps; exposing the chip to a plasma at the end of the 1st day results in large and rough gaps. Most likely, letting the Cr oxidize overnight results in an initial homogeneous oxidation and the effect of the subsequent plasma is reduced. In the rest of the batches, the plasma step was always done at the start of the second day.

Up to this point, the particles inside the gap have been a consistent feature through all iterations where the AJAs were used for evaporation. Aside from these particles, the gaps appear to meet our criteria; the gap size is around 10-15 nm and the edges of the ME and AE are smooth enough. Therefore, removing these particles might result in nanogaps with the desired gap size and smooth edges. The origin of these particles remains unknown, however, the Cr layer was regularly incompletely etched. As described in section 2.2, the final step in the process is the wet etching of the Cr layer using TechniEtch Cr-01, which is a mixture of perchloric acid HClO_4 and ceric ammonium nitrate $(\text{NH}_4)_2[\text{Ce}(\text{NO}_3)_6]$ [10]. The reported etching rate of Cr is 60-100 nm/min; hence the 2 minute etch employed in our process should be long enough to get rid of all Cr. As this was not the case, we tried an aggressive approach: the chip was first agitated in the etchant during 1 minute, followed by a 10 minute bath at 50 °C. The heated etchant with the chip was then gently sonicated for 7 minutes, agitated for 1 minute and finally left in a final bath at 50 °C for 7 minutes. The result is shown in figure 2.7. Panel a shows a chip with the old etching process, panel b a chip after the aggressive process. The particles are still present in the gaps and therefore are not chromium particles. Important to note is that the Cr layer is fully etched using the aggressive approach, whereas this is not always the case with the old process. The incomplete etching after 2 minutes is unexpected given the advertised etching rate and is problematic for the fabrication of devices with a LG. J.A. Labra-Muñoz has tested the breakdown voltage of the Hf oxide layer before and after the Cr etch and found that the breakdown voltage was lower as a result of the wet etching step. A balance should be found between getting rid of the sacrificial Cr layer while at the same time minimizing the etching time.

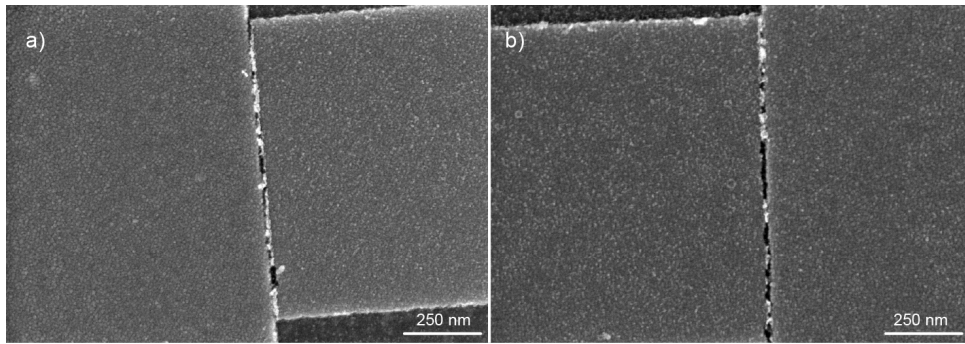


Figure 2.7: a) SEM image of a junction fabricated using the old etching method: 2 minutes at room temperature of which 1 minute sonication. b) SEM image of a junction fabricated using an aggressive etching method: 1 minute in the etchant while slowly moving the sample, 10 minutes in a beaker with etchant heated to 50 °C, gentle sonication for 7 minutes followed by a final bath at 50 °C for 7 minutes.

Still uncertain about the origin of these particles, we decided to study several finalized chips under a large angle in the SEM. Figure 2.8 shows two SEM images of chips from different batches. In both pictures, the AE is folding upward and lying on top of the ME. Based on this, the metallic particles are actually sharp protrusions from the metal of the AE, which appear extra bright in the SEM as a result of the edge effect [11]. The folding of the electrode is unexpected due to evaporation being a line of sight process. The overhang resulting from the oxidation of the Cr layer should create an area where no metal is deposited during evaporation; instead, it seems as though the metal was evaporated on top of something, allowing the protrusions to reach higher than the ME.

One possible explanation for this would be that the evaporation occurred under a small angle, allowing the coverage of the side of the ME. However, this folding was observed on both sides of the ME and the orientation of the stage was fixed throughout the evaporation, invalidating this scenario. Another scenario would be the presence of stress within the Cr layer. A study by Shaginyan *et al.* [15] reports that the grain size of Cr is expected to increase during evaporation as a result of the rising surface temperature. As a result of this increased grain size, a stress gradient exists within the Cr layer. It is possible for this stress gradient to cause the top to compress slightly with respect to the bottom of the layer, leading to a slight angle on top of which particles are deposited during evaporation. This is, however, speculation. More investigation is needed to determine the cause of this folding.

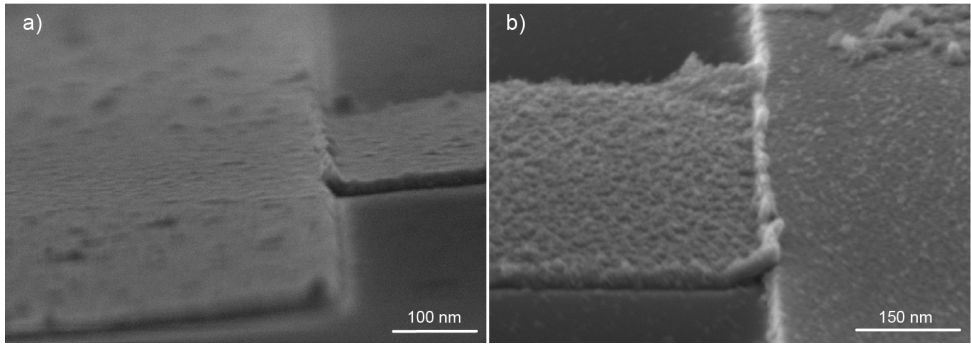


Figure 2.8: SEM images of finalized chips taken under an angle. a) Chip with a local gate electrode. b) Chip without a local gate electrode.

In order to prevent the folding of the electrode, we increased the height difference between the ME and the AE from 5 to 10 nm. During the evaporation of the AE, also a metal layer is deposited on top of the ME, i.e., on top of the Cr. The reasoning behind increasing the height difference was that these layers might get disconnected and we could get rid of the folding through this. The result is shown in figure 2.9, with panel a) showing a junction with a height difference of 5 nm and panel b) with a 10 nm difference. No difference is observed; the ME and AE remain connected. It would be of interest to investigate the effect of having no height difference in a future batch.

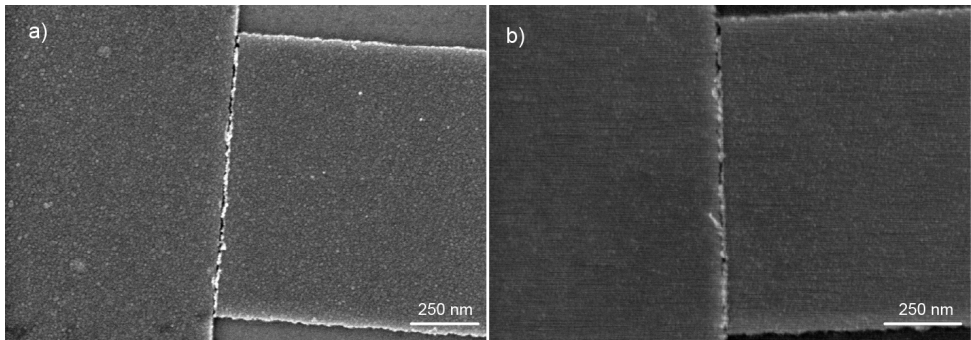


Figure 2.9: a) Junction with a height difference of 5 nm between main- and auxiliary electrodes. b) Junction with a height difference of 10 nm between main- and auxiliary electrodes.

Finally, to investigate whether stress within the Cr layer is the cause of the folding, we increased the Cr layer thickness to 40 Å, varied the evaporation rate between 0.5 Å/s and 2.0 Å/s and evaporated in cycles of 5 nm with a one minute pause between the cycles. The cyclic evaporation should reduce the effect of changing surface temperature during evaporation if that is indeed present. The results are shown in figure 2.10. Panel a shows a junction which was fabricated using 40 nm chrome and a rate of 0.5 Å/s, the rate which was used for most batches. Comparing this junction to the previous ones, we do not see a clear difference, which would mean that the effect of the cycles is negligible. Increasing the rate to 1.0 Å/s and 2.0 Å/s seems to decrease the amount of protrusions slightly, as well as increasing the edge roughness. A higher evaporation rate has been reported to lead to an increase in grain size for Al [16]. A larger grain size would explain the increased edge roughness.

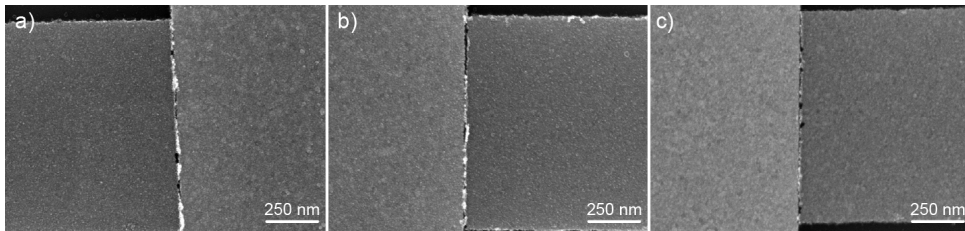


Figure 2.10: SEM images of chips where the Cr layer was 40 nm thick, as well as evaporated in 5 nm cycles with a pause in-between. a) Junction where the Cr was evaporated at a rate of 0.5 Å/s. b) Junction where the Cr was evaporated at a rate of 1.0 Å/s. c) Junction where the Cr was evaporated at a rate of 2.0 Å/s.

2.3. Reference measurements

Nanoparticles can be synthesized in many ways. Our goal is to measure nanoparticles with built-in functionalities, which combines the SET character of a particle between two electrodes with quantum transport features. To interpret measurement results, a set of reference data is needed for our device structure. The reference data should be recorded for a relatively simple system, namely a metallic nanoparticle. In prior research, gold nanoparticles were used as a reference system because of their relative simplicity [3, 17, 18]. For example, Khondaker *et al.* [3] report the observation of Coulomb Blockade, confirmed by the fitting of orthodox Coulomb blockade theory to the experimental data.

2.3.1. Trapping of a single gold nanoparticle

Despite the fabrication issues, some of the samples (especially the ones with a large gap) yielded devices that were suitable for further studies. Here, we report on the fabrication and measurement of reference samples containing gold nanoparticles with a diameter of 30 nm. The trapping of these nanoparticles is a probabilistic process. A solution containing the nanoparticles is drop-cast on top of the chip and left to evaporate, resulting in a small chance of a particle bridging the ME and AE. A solution of 30 nm gold nanoparticles suspended in citrate buffer from Sigma-Aldrich was used. The solution has a concentration of $\sim 1.8 \times 10^{11}$ particles/mL. Letting the solution evaporate resulted in a 'coffee stain' of nanoparticles on the chip, shorting all junctions. Therefore, on a next chip, the droplet was left on the chip for 1 minute and then the remaining liquid was removed by sucking it up with a tissue. Current-voltage (IV) characteristics were recorded on 2 different chips at room temperature in a vacuum; a total of 3 junctions were found to show a signature of a trapped nanoparticle.

Figure 2.11a shows a SEM image of sample 1 containing a single gold nanoparticle imaged after the measurements finished. Panel b) shows the corresponding IV characteristic before and after deposition of the nanoparticles. Before deposition no current is observed up to a bias voltage of 1.5 V (blue drawn line). After deposition a current of 1 nA is observed at a bias voltage of 350 mV (orange curve). This change is indicative of trapping a nanoparticle in the nanogap and is normally the only way of telling whether a particle has been trapped or not. However, because gold nanoparticles conduct well and, if they are large enough, they can be observed in a SEM as shown in figure 2.11a. Panel c) shows the IV characteristic before and after deposition of sample 2. This sample 2 has a current of 3 nA at a bias voltage of 350 mV, a factor 3 higher than Sample 1. The current displays switches; these seem to occur between two conductance levels. The size of these switches is much larger than the noise level and is therefore not caused by electrical noise. Finally, panel d) displays the IV characteristic before and after trapping of sample 3, where a current of around 12 pA was observed at a bias voltage of 350 mV. The difference in current compared to the other samples is most likely the result of a difference in the widths of the tunneling barriers between the nanoparticle and the platinum electrodes.

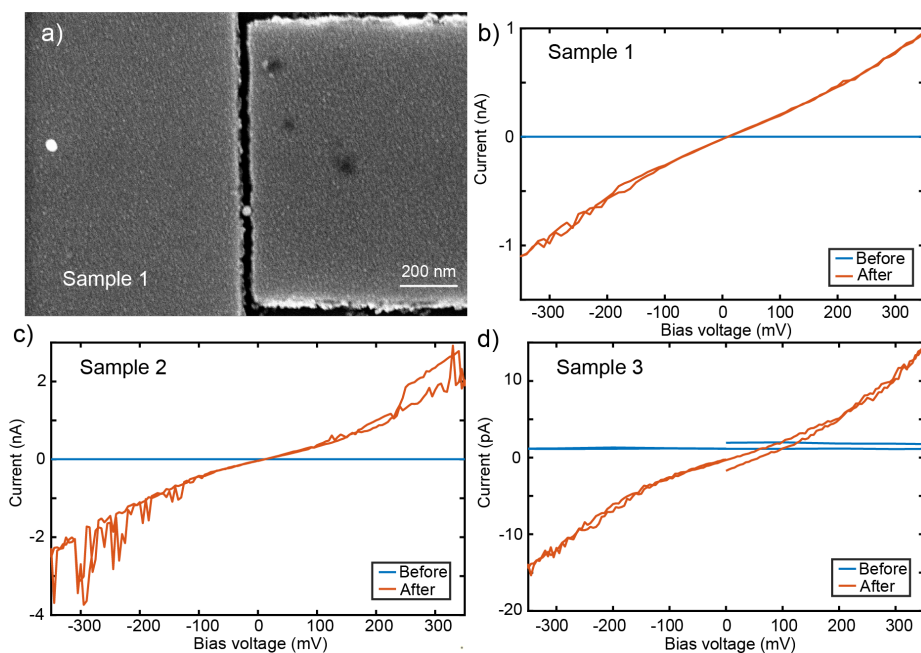


Figure 2.11: a) Zoomed in scanning electron microscopic image of a nanogap containing a single gold nanoparticle. b) Current-voltage characteristic of sample 1, measured at room temperature in a vacuum across a nanogap before and after deposition of a solution with gold nanoparticles; this characteristic corresponds with the sample whose SEM picture after measurements is shown in a). c) Current-voltage characteristic of sample 2, measured in the same conditions as sample 1. d) Current-voltage characteristic of sample 3, measured in the same conditions as sample 1.

2.3.2. Low-temperature measurements

The samples were cooled down to around 10 K in a cryo-free probestation and current-voltage (IV) characteristics were recorded. Two examples of IVs at base temperature are shown in figure 2.12a,b. IV characteristics were recorded for a bias voltage between -50 to +50 mV. Figure 2.12a,b show two IVs, one from Sample 1 and one from Sample 2. A consistent offset of 10 mV was observed in the measurements, therefore the plots were shifted by -10 mV and cut off at 40 mV. In panel a, around zero bias a flat region is observed until ± 10 mV, after which the current increases (decreases) with increasing (decreasing) bias voltage. Additionally, small steps are observed in the current. The current displays switches above a bias voltage of 20 mV. In panel b the same behavior is observed, although the steps are less visible.

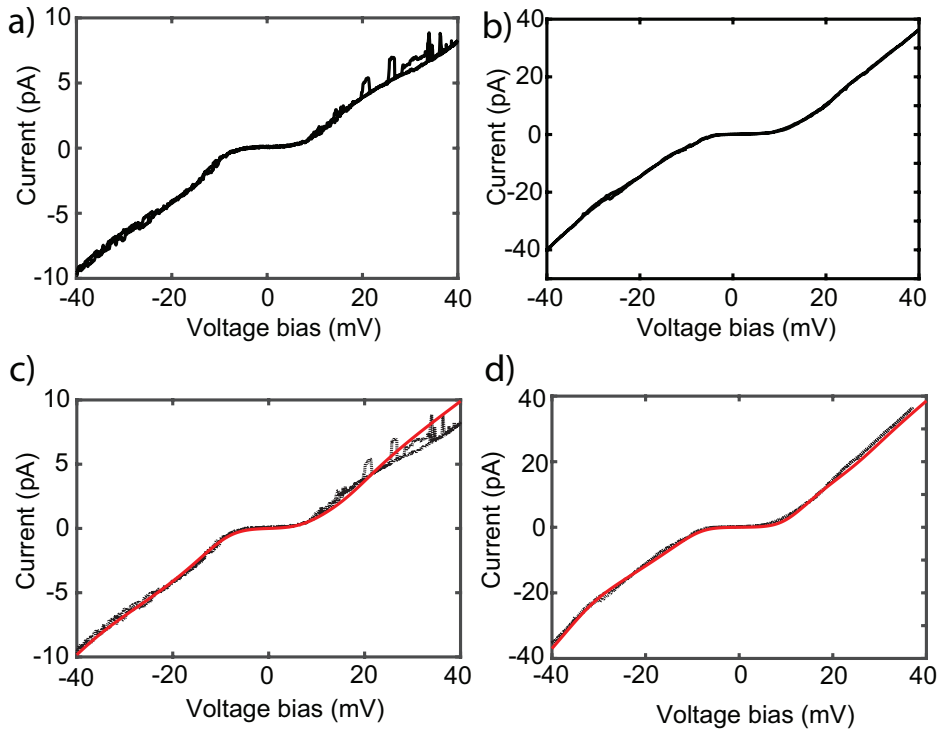


Figure 2.12: Current-voltage (IV) measurements on nanogaps containing a gold nanoparticle at 10 K. a) IV characteristic of Sample 1. b) IV characteristic of Sample 2. c) IV characteristic of Sample 1 to which the orthodox Coulomb blockade model was fitted (red). d) IV characteristic of Sample 2, to which the orthodox Coulomb blockade model was fitted (red).

In order for the junction to behave as a SET, Coulomb Blockade (CB) is needed. CB is a consequence of making a system very small and confining the electrons inside it. These electrons experience a strong Coulomb repulsion, leading to an energy cost, the charging energy E_C , associated with adding an electron to the system. If the thermal energy is small compared to E_C , no current can flow unless energy is provided by tunneling electrons through for example a bias voltage. If such a system is placed between two electrodes, isolated from them through tunneling barriers such that the resistance of the tunneling junction, $R \gg R_q = h/2e^2 \approx 12.9 \text{ k}\Omega$, we obtain a SET. In a SET, most electron transfer processes only involve a single electron. In IVs, CB can be recognized by two possible characteristics: a region of (close to) zero current around zero bias, and/or steps in the current as a function of bias voltage. The manifestation of these depends on parameters such as the alignment of the energy levels of the island with respect to the Fermi energy of the electrodes, charges in the proximity and the coupling of the island to the electrodes. In [3], CB is observed in a SET made with gold nanoparticles of 10 nm diameter. The classical CB model is fitted to their data and shows great correspondence. In order

to verify that we are observing CB, we fit the same model to our data. The model contains 6 parameters: two capacitances (one for each barrier), two resistances (one for each barrier), the temperature and the offset charge. The fitting is done by tweaking these parameters by hand in order to obtain a curve which follows the experimental data. The parameters for the fits in figure 2.12c,d are shown in table 2.1.

	C_1 (aF)	C_2 (aF)	R_1 (M Ω)	R_2 (M Ω)	T (K)	Q_0
Sample 1	8	5.8	600	2400	10	0.85
Sample 2	3.7	4.7	460	180	10	0.75

Table 2.1: Table displaying the fit parameters of the Coulomb Blockade model, fitted to the data presented in figure 2.12. $C_{1,2}$ are the capacitances of the tunnel barriers, $R_{1,2}$ the resistances of the tunnel barriers, T the temperature and Q_0 the offset charge.

The data can be fitted well by the orthodox CB model, confirming single electron transport. The two different junctions display similar behavior, with a blockade region between ± 10 mV after which the current goes up (down) for increasing (decreasing) bias voltage. In orthodox CB, the current is blocked between $V = \pm e/C = 2E_C/e$, which means that the charging energy is around 5 meV in our case for both samples. We can also compare this with the value we obtain from our fits, where $E_C = e/(2 * C)$ with $C = C_1 + C_2$. This yields a charging energy of 6 meV for Sample 1 and 10 meV for Sample 2. These values are close to each other and consistent with what is expected for particles of this size. The difference between the two can be explained by a difference in the contact between the particle and electrodes, resulting in a slightly different total capacitance. In this case, Sample 2 is contacted more symmetrically as seen from the values listed in table 2.1 for the capacitances. Comparing the values to Khondaker *et al.*[3] we see similar values for the capacitances, which is surprising considering we have 30 nm particles, whereas Khondaker *et al.* used 10 nm particles. The difference could be explained by the difference in chip geometry. Where they built a bridge with 20 nm nanoparticles, break it with a voltage and then deposit the 10 nm particles to obtain a SET, we have two platinum electrodes between which we trapped a single nanoparticle. For a full understanding of the CB behavior, a gate electrode should be added such that the Coulomb diamonds can be measured.

2.4. Conclusion and outlook

In this chapter we investigated the impact of different fabrication steps on the quality of the nanogaps in an effort to obtain 15 nm high aspect-ratio nanogaps following a formerly working process [6–8]. We changed parameters one by one to pinpoint the origin of the problems, but did not manage to obtain consistently good nanogaps. The thickness of the Pt did not have any impact on the final result. Surprisingly, this was also the case for the thickness of the Cr layer, which was reported by Fursina *et al.* [6] to directly control the gap size. Looking at the oxidation process of the Cr, which is done by leaving the sample in a desiccator for one

night and exposing it to an oxygen plasma, we found that the Cr seems to barely oxidize. The best order in which to do these two steps is to first leave the chip in the desiccator during which it will oxidize slowly and evenly. The oxygen plasma will then clean the substrate and oxidize the Cr layer a little more, but the oxidation will remain quite homogeneous. In most gaps fabricated in the AJAs the nanogaps seemed fine but filled with unwanted particles, shorting the two electrodes. To remove these particles, we first performed an extensive Cr etching step, which was found to have no effect at all. Imaging these particle-filled junctions under an angle in the SEM showed that these particles were in fact protrusions from the AE, which somehow had folded on top of the ME. First we increased the height difference between the ME and AE in an attempt to get rid of this folding, which was unsuccessful. A possible explanation for the cause of this folding is compressive stress within the Cr layer, which is a result of an increasing surface temperature during evaporation, leading to a change in grain size and thus in a stress gradient within the film. This hypothesis was tested by evaporating the Cr in cycles of 5 nm with a 1 minute pause between cycles. No difference was observed for a Cr rate of 0.5 \AA/s and 1.0 \AA/s , which indicates that stress is not the cause of the folding. However, the layer thickness of Cr was also increased to 40 nm, therefore it would be prudent to perform the same test with a thickness of 25 nm for a definitive conclusion. Also a rate of 2.0 \AA/s was tested: the gaps seemed cleaner, but also less smooth. This is probably the result of a larger grain size. Why this would lead to less protrusion from the AE is unclear. For future batches, we would first perform the above-mentioned test where cyclic evaporation of Cr is done for a thickness of 25 nm. Another batch should be made without the height difference between ME and AE to investigate whether this has any effect. Finally, the oxidation we observe seems to be taking place to a lesser extent than J. Houtman [7] observed. Therefore, we would investigate whether oxidizing at an elevated temperature (at least $300 \text{ }^\circ\text{C}$) yields different results.

We have also measured 30 nm gold nanoparticles on these chips to obtain a set of reference data. Trapping of the nanoparticles was found to be done optimally by first drop-casting $5 \mu\text{L}$ of solution on the chip and extracting the fluid after 1 minute, preventing all particles from precipitating on the sample. A current was observed after drop-casting in 2 junctions. Sample 1 was visually confirmed to contain a single nanoparticle through a SEM image. At 10 K, the IVs displayed a region of low current around zero-bias. The data could be fitted accurately by the orthodox CB model with similar values for the two samples and is consistent with those reported in literature. The observation of CB confirms that our system behaves as a SET and the measurements serve as a reference for the measurements performed in the next chapter. It would be interesting to add a gate electrode to the measurements and try to measure the Coulomb diamonds to obtain a full picture of the behavior of these SETs.

References

- [1] D. V. Averin and K. K. Likharev, *Coulomb blockade of single-electron tunneling, and coherent oscillations in small tunnel junctions*, *Journal of Low Temperature Physics* **62**, 345 (1986).
- [2] Y. V. Nazarov and Y. M. Blanter, *Quantum Transport* (Cambridge University Press, 2009).
- [3] S. I. Khondaker, K. Luo, and Z. Yao, *The fabrication of single-electron transistors using dielectrophoretic trapping of individual gold nanoparticles*, *Nanotechnology* **21**, 095204 (2010).
- [4] F. Prins, M. Monrabal-Capilla, E. A. Osorio, E. Coronado, and H. S. J. van der Zant, *Room-Temperature Electrical Addressing of a Bistable Spin-Crossover Molecular System*, *Advanced Materials* **23**, 1545 (2011).
- [5] RAITH, *Proximity effect correction – Getting your design precisely implemented on every sample*, <https://raith.com/technology/nanofabrication-software/proximity-effect-correction/>, accessed: 3-5-2024.
- [6] A. Fursina, S. Lee, R. G. S. Sofin, I. V. Shvets, and D. Natelson, *Nanogaps with very large aspect ratios for electrical measurements*, *Applied Physics Letters* **92** (2008), 10.1063/1.2895644.
- [7] J. Houtman, *Electrical characterization of Prussian blue analogue nanoparticles*, Master's thesis, Delft University of Technology (2018).
- [8] J. Labra-Muñoz, *Electrical and magnetic properties of ferritin: electron transport phenomena and electron paramagnetic resonance*, Ph.D. thesis, Leiden University (2023).
- [9] T. A. Green, *Gold etching for microfabrication*, *Gold Bulletin* **47**, 205 (2014).
- [10] Technic, *TechniEtch Cr:n1 Technical Data Sheet*, https://www.microchemicals.com/dokumente/datenblaetter/tds/tf/en/tds_tf_technietch_cr01.pdf, accessed: 2025-01-01.
- [11] JEOL, *Edge effect*, <https://www.jeol.com/words/semterms/20121024.012800.php#gsc.tab=0>, accessed: 3-5-2024.
- [12] G. Kostic, I., Vutova, K., Koleva, E., Andok, R., Bencurova, A., Konecnikova, A., Mladenov, *Polymer science: research advances, practical applications and educational aspects*, edited by A. Méndez-Vilas, A., Solano (Formatex Research Center, 2016) pp. 488–497.
- [13] Kurt J. Lesker, *Platinum Pt Evaporation Process Notes*, https://www.lesker.com/newweb/deposition_materials/deposition-materials-notes.cfm?pgid=pt1, accessed: 3-5-2024.

- [14] M. Graham and R. Hussey, *Characterization and growth of oxide films*, *Corrosion Science* **44**, 319 (2002).
- [15] L. Shaginyan, J. G. Han, and H. M. Lee, *Structural Nonuniformity and Internal Stress in Chromium Films Deposited by Magnetron Sputtering*, *Japanese Journal of Applied Physics* **43**, 2594 (2004).
- [16] K. BORDO and H.-G. RUBAHN, *Effect of Deposition Rate on Structure and Surface Morphology of Thin Evaporated Al Films on Dielectrics and Semiconductors*, *Materials Science* **18** (2012), 10.5755/j01.ms.18.4.3088.
- [17] L. Caillard, O. Seitz, P. M. Campbell, R. P. Doherty, A.-F. Lamic-Humblot, E. Lacaze, Y. J. Chabal, and O. Pluchery, *Gold Nanoparticles on Oxide-Free Silicon–Molecule Interface for Single Electron Transport*, *Langmuir* **29**, 5066 (2013).
- [18] Y. V. Kervennic, H. S. J. Van der Zant, A. F. Morpurgo, L. Gurevich, and L. P. Kouwenhoven, *Nanometer-spaced electrodes with calibrated separation*, *Applied Physics Letters* **80**, 321 (2002).

3

Trapping and Characterization of Prussian Blue Analogue Nanoparticles on Different Chip Geometries

Abstract

Prussian blue analogue nanoparticles have attracted interest due to their potential application as sensors, memory elements and spintronics devices. These particles have a diamagnetic low spin state and a paramagnetic high spin state, between which can be switched reversibly through for example light. This study investigates electronic transport through 15 nm Prussian blue analogue nanoparticles using three device geometries: point-contact nanogaps, chromium nanogaps, and overlapping-contact nanogaps, in order to optimize the trapping of a single nanoparticle. The chromium nanogaps were found to have the highest trapping rate (1.2%), followed by the point contacts (0.7%) and the overlapping electrodes (0.5%). Current-voltage measurements at 10 K show different behaviors for the different device geometries. The point-contact gaps exhibited Coulomb blockade-like behavior, while no signal was detected in the other two geometries; however, warming up the devices restored the signal. The Coulomb blockade-like behavior in the point-contact gaps is characterized by an asymmetric large suppression region around zero bias, followed by steps of different sizes. Additionally, a stability diagram reveals only two of the four lines making up Coulomb diamonds. These observations suggest that the electronic transport takes place through multiple particles in series, which are coupled asymmetrically to the electrodes. For the chromium and the overlapping-electrode nanogaps the temperature dependence of the current was investigated and Arrhenius behavior was observed, suggesting thermally

activated transport. We discuss our results in the context of the double Schottky barrier model, as well as the Mott and Efros-Shklovskii variable range hopping models. Due to the limited range of our current-voltage characteristic, fitting yields inaccurate estimates for the parameters. From an Arrhenius fit we extract activation energies of 0.52 and 0.35 eV, which are similar to the barrier energies found in another study in a conductive atomic force microscope setup. The average hopping length is estimated for both hopping models. For the Mott variable range hopping the estimate is around 1.1 nm, about the same size as the unit cell, which would be more in line with nearest neighbor hopping. For Efros-Shklovskii variable range hopping we obtain an estimate of $93/\epsilon$ pm, with ϵ the dielectric constant, which is smaller than the atomic radius. Based on our data, we cannot distinguish between the double Schottky barrier model and the nearest neighbor hopping model; more current-voltage measurements need to be recorded in a larger bias range. The two observed behaviors, Coulomb blockade and thermally activated transport, can be explained by larger effective tunneling barriers for the latter case. When the particle makes good contact with the electrodes, the tunneling barriers are small enough to observe Coulomb blockade at low temperatures. When the contact is poor however, the effective barriers are large and the transport becomes thermally activated, resulting in an exponentially decaying conductance with decreasing temperature. As a result, no current is observed at low temperatures.

3.1. Introduction

With the ever-increasing need for smarter and smaller devices, the idea of creating materials which exhibit specific functionality as a result of their intrinsic properties has grown in popularity. Spin crossover (SCO) is a phenomenon which has gained interest in this regard. SCO compounds have the fascinating property that they possess two spin states: a low-spin (LS) and a high-spin (HS) state, between which can be reversibly switched through external stimuli such as temperature, pressure, light or magnetic field. SCO occurs in octahedral complexes of first-row transition metal ions with 4-7 3d electrons [1, 2]. The d-orbitals of the central metal ion are distorted by the field of the ligands, causing a splitting between the d_{xy} , d_{yz} and d_{zx} orbitals and the d_{z^2} and $d_{x^2-y^2}$ orbitals. Due to the competition between the ligand field stabilization energy and the spin-pairing energy, many SCO compounds can undergo a thermal spin transition (ST), where at a critical temperature the ground state changes from LS to HS or vice versa. Additionally, a switch in spin state is often accompanied by a change in the physical properties such as color and size of the material. For example in Iron(II) complexes the Fe-N bond length changes from 2.0 to 2.2 Å [3]. Depending on the cooperativity of the crystal, thermal hysteresis can be present [4, 5], where the transition temperature for LS->HS is not the same as the one from HS->LS [6]. This bi-stability property paired with the thermal hysteresis opens up potential applications of these complexes as for example spintronics devices, sensors, or actuators and memory elements [7, 8].

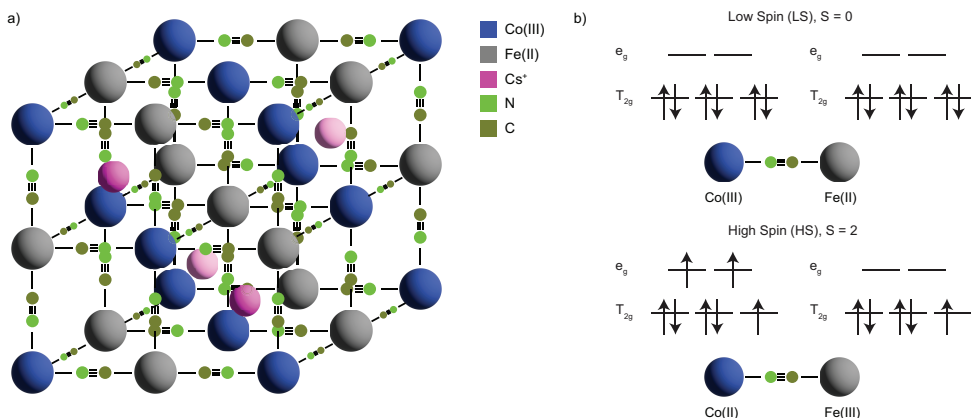


Figure 3.1: a) Sketch of the crystal structure of CsCoFe nanoparticles. Dark blue spheres denote cobalt atoms, grey spheres iron atoms, dark-green carbon atoms, light-green nitrogen atoms and pink the cesium cations. Each pair of cobalt and iron atoms is connected through a cyanide group. b) Energy level diagram showcasing the transition between the LS and HS states, which is caused by a charge-transfer process where Co(III) reduces to Co(II) by receiving an electron from Fe(II), which oxidizes to Fe(III).

A subset of SCO complexes is the so-called Prussian Blue Analogue (PBA) compounds, consisting of two metallic ions bridged by cyanide ligands. The name is derived from the infamous Prussian Blue (PB), or ferric hexacyanoferrite, which was used as a paint color in for example Vincent van Gogh's 'Starry Night'. PB nanoparticles (NPs) have a broad range of applications: from cancer treatment, to battery electrode material, to antidote for internal radioactive contamination [9–12]. Replacing one or both of the metallic ions by other transition metal ions (for example Zn, Mn, Co) leads to the creation of PBAs, see figure 3.1a for an example of a CsCoFe PBA [13]. PB and its analogues are of interest because of their magnetic properties. Particularly interesting about PBAs is that not only are they bistable, with a LS and a HS state, the ST goes paired with a Charge Transfer (CT) between the metal ions, changing their oxidation state (see Fig. 3.1b). Research has shown that upon light irradiation of the earlier mentioned CsCoFe nanoparticles, the ST is triggered, causing an elongation of the Co-N bonds, resulting in the transfer of an electron from the Co ion to the Fe ion [14, 15]. Another important matter is the presence of the cesium cations, which provide charge balance. Without these cations inserted in the crystal, a structure deficiency of hexacyanometallate is present and the coordination sphere of the cobalt centers neighboring a vacancy is filled by water molecules [13]. This has an impact on the ST and photomagnetic properties of the particles since H_2O provides a weak ligand field compared to cyanide, leading to less distortion of the d-orbitals. Hence, it is possible to tune the ST and photomagnetic properties of PBA through the amount and type of inserted cations [16]. For a crystal with a higher H_2O content the ground state tends towards HS due to the weak ligand field, while for higher cation insertion the ground state tends towards LS.

Due to the ST and photo-magnetic properties of PBAs, potential applications in nanoscale devices are possible such as sensors, memory elements or spintronics devices. For these applications, the electronic transport properties of PBA nanoparticles are essential. Research has focused on the photo-magnetic properties at the nanoscale, but little is known about the transport characteristics. A few studies were done at the micro-scale for thin films and powders [17, 18]. More recently, two studies were performed on the same CsCoFe nanoparticles as studied here through conductive atomic force microscopy (C-AFM) measurements [19, 20]. In the first study electron transport through devices consisting of 1-3 nanoparticles was investigated. They observed an exponential dependence of the current on distance with low decay factors. In the second study different particle sizes are measured and they observe an almost size-independent electron injection barrier. Additionally, no correlation between conductance and particle size is found. Bulk PBAs have been shown to behave as a semiconductor with a band gap of around 2 eV [21, 22]. Therefore, they argue that the system can be modelled by a double Schottky barrier with barrier heights in the range of 0.28 - 0.43 eV and they are able to accurately fit this model to their data. However, in their C-AFM setup it is not possible to tune the electrostatic potential due to the lack of a gate electrode, nor can the temperature dependence of the electronic transport be studied.

In this chapter we study CsCoFe nanoparticles with the chemical formula $\text{Cs}_{0.7}\text{Co}[\text{Fe}(\text{CN})_6]_{0.9}(\text{H}_2\text{O})_{0.6}$, synthesized by the group of Prof. Dr. T. Mallah [23] and shown in figure 3.1a. They consist of pairs of Co and Fe ions, linked through cyanide ligands. Cesium cations are present for charge balance [13, 24]. Important to note is that the particle contains vacancies: around 10% of $\text{Fe}(\text{CN})_6$ sites are empty and water molecules coordinate to the Co atoms; this is not shown in the figure. The Co(III)Fe(II) LS state (Fig. 3.1b) is diamagnetic, whereas the Co(II)Fe(III) HS state is paramagnetic with the total spin of a Co-Fe pair being $S = 2$. The goal is to characterize the transport properties of the nanoparticles with on-chip devices and investigate how the ST affects these properties. To this end, we trap these nanoparticles using three different device geometries to optimize the trapping process. Current-voltage (IV) measurements are performed at room- and low temperature for different gate voltages. We observe different behaviors for different device geometries and fit these into a picture that is coherent with the C-AFM measurements.

3.2. Experimental

We trap and perform charge transport measurements on 15 nm CsCoFe PBA nanoparticles. The synthesis of the particles was done by the group of Prof. Dr. T. Mallah in Paris and is reported in a publication by Trinh *et al.* [23]. The trapping process of nanoparticles within a nanogap is a matter of chance, with generally low trapping rates ($< 1\%$). In order to optimize this process, three different chip designs were tested: the point-contacts, the high-aspect ratio Cr gaps and the overlapping electrodes (see figure 3.2a,c,e). Fabrication was done in the Kavli Nanolab at the Delft University of Technology.

The point-contact nanogaps are shown in figure 3.2a, together with a scanning electron microscopic (SEM) picture in panel b. A junction consists of two contact pads with two platinum electrodes in-between. The electrodes are separated by a 5-15 nm gap. The point-contacts are fabricated by direct ebeam writing and electrode evaporation (see the recipe in the appendix section 3.6.1). The advantages of this design is the easy and quick fabrication process, which makes it possible to achieve the smallest gap sizes out of all three designs, as small as 5 nm. The downsides of the point-contact gaps are their narrow electrodes and the absence of a local gate. The trapping of nanoparticles can only happen in a small area, leading to a low trapping yield. Due to the absence of a local gate, a gate voltage can only be applied to the silicon substrate, which is separated by 285 nm of silicon oxide from the electrodes, leading to a weak gate electric field at the junction.

The second design is the high-aspect ratio chromium (Cr) nanogaps described in Chapter 2. The design is shown in figure 3.2c, with a SEM image in panel d. The chip consists of a platinum main electrode (ME) in the middle, surrounded by platinum auxiliary electrodes (AEs), with the nanogaps at the points where they intersect. This design incorporates a local gate (LG), which is buried beneath a 20 nm HfO_x layer. The high-aspect ratio is expected to increase the trapping rates, but gap sizes are generally 15-25 nm. The main advantages of this geometry are the high aspect-ratio and the presence of a local gate. The trapping rate is expected to scale with electrode area, hence the high aspect-ratio should lead to more trapping events. The local gate allows for the effective application of an electric field at the junction. The disadvantage of the high aspect-ratio gaps is the elaborate fabrication process. As laid out in chapter 2, it has not been possible to achieve sub-15 nm gap sizes. This is expected to render trapping a particle difficult, as the particle are cubes with sides of 15 nm on average.

Finally, we have used overlapping contacts, which consist of two palladium electrodes patterned such that the last 120 nm is next to the other electrode, with a 15-20 nm gap between the two electrodes (see panel e and f of figure 3.2). The fabrication was done by following the procedure documented in section 3.4.1 of Dr. D. Bouwmeester's doctoral thesis [25], using palladium as material for the electrodes. No sticking layer is present, as this diminished the smoothness of the electrodes. As a result, extra care is required when drop-casting solution on the chip or immersing the chip. This design is a compromise between the two previously mentioned geometries: it possesses a relatively large junction width (120 nm), which should facilitate the trapping of a nanoparticle and the fabrication pro-

cess is relatively simple. Similar to the point-contacts, no local gate is present.

Trapping of the nanoparticles can be done in different ways. The main method employed in this chapter is the drop-casting of a solution on top of the chip and waiting for the liquid to evaporate. Due to the high surface tension of water, solutions were made with differing quantities of methanol, which reduces the surface tension and allows the droplet to cover a larger area. This method results in an aggregation of the particles towards the edges of the droplet and a lower concentration in the middle. Alternatively, some chips were submerged in solution, which results in a more homogeneous coverage of the particles on the chip.

Current-voltage (IV) measurements were performed in a lakeshore CRX-6.5 cryo-free probestation. It possesses six arms which can be freely moved. The probestation operates under a vacuum and can reach a base temperature of around 10 K. Two heaters are present in the system, allowing for precise temperature control over the full 10-300 K range. An IVVI rack built by DEMO at the Delft University of Technology was used to perform the measurements [26]. Two-probe IV measurements were done by applying a voltage bias and measuring the resulting current. The D5 bias-DAC module was used as a voltage source, connected to an S1d module to allow for amplification if needed. Measurement was done by passing the signal through the M1b module which acts as a current amplifier and readout was done with a Keithley 6500.

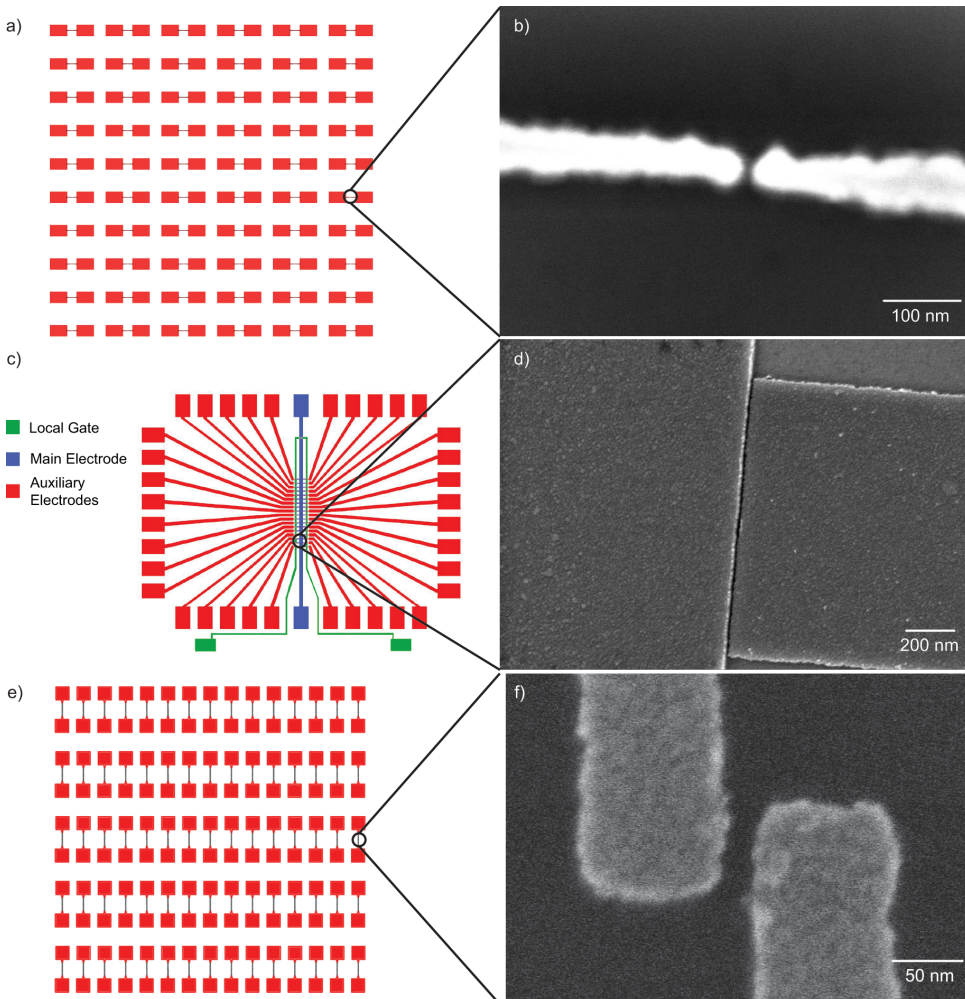


Figure 3.2: a) Sketch of the point-contact device geometry, where the electrodes consist of a Ti sticking layer with a Pt layer on top. b) SEM image of a point-contact nanogap of 11 nm. c) Device geometry for the Cr-based nanogaps, consisting of a local gate (shown in yellow) buried beneath an Hafniumoxide layer, a central main electrode (blue) and auxiliary electrodes (red). The electrodes consist of a Ti sticking layer and a Pt layer. d) SEM image of a high aspect-ratio nanogap of 20 nm. e) Overview of the overlapping electrodes geometry, with the electrodes consisting of only a layer of Pd. f) SEM image of a single nanogap of 19 nm.

3.3. Results

3.3.1. Room-temperature characterization and trapping

Before any particles are deposited on a chip, all junctions have to be characterized. To this end, an IV is recorded at room-temperature in a vacuum for every junction from -1.5 to 1.5 V bias. In the case of an empty junction, no current should be observed. Junctions which displayed a current higher than 2 pA at ± 1.5 V are not used in any measurements.

After this initial characterization step, a solution is prepared by diluting the original solution (a colloidal suspension of the particles in de-ionized water with 400×10^{14} NPs/L) 2-50 times in either de-ionized water or methanol. Deposition is done by either drop-casting a droplet of 5 μ L on top of the chip or immersing the chip in the solution for around 10 seconds. After deposition the chip is left in ambient conditions to dry, after which it is loaded in the probestation and the chamber is pumped to a vacuum by a turbopump.

All junctions which did not display a current before (we refer to them as being 'open') are now measured again. This time in a smaller bias voltage range to reduce the risk of losing a trapped particle. If something has been trapped in a junction, a current is observed. See figure 3.3 for examples of IVs that were recorded on junctions where something has been trapped. Panels a), b) and c) represent measurements on the point-contacts. The panels represent different junctions on the same chip. Panels d) and e) were recorded on two different chips with the Cr nanogap geometry and f) was recorded on a chip with the overlapping-electrode geometry. In all panels, a clear difference in the IV characteristic is observed before and after deposition of the nanoparticles, which indicates that something has been trapped in the junction. Interesting is the high resistances (defined as $V_{\max}/I_{@V_{\max}}$) we observe: 400 M Ω (panel a) up to as high as 500 G Ω (panel f). Important to note is that the resistances for the point-contact gaps are the lowest: 400, 800 and 125 M Ω , whereas the resistance for the other geometries are much higher: 350, 2.3 and 500 G Ω . Different line-shapes are observed: in panels a), b) and c) the current increases non-linearly with increasing bias voltage with a slight asymmetry between positive and negative bias voltage in a), panel d) shows a linear IV, in panel e) we observe a current that saturates at around 150 pA and in f) the current increases linearly with increasing bias voltage, but shows a suppressed region around zero bias.

For the point-contact nanogaps, 11 chips were measured, with 60 junctions on each chip. On one chip something was trapped at room-temperature; 5 junctions displayed a current after deposition. This chip was completely immersed in the solution, as opposed to the drop-casting of solution on top of the chip.

16 chips were measured with the Cr nanogap geometry, each chip has 36 junctions. In 7 junctions across 3 chips something was trapped at room-temperature.

For the overlapping nanogaps, 2 chips were measured, with 96 junctions per chip. 1 junction displayed a current after deposition. Also here, deposition was done by submerging the chip in the solution, instead of drop-casting.

From these numbers, it is clear that the trapping rate is low. The most success was

achieved on the Cr nanogaps with a yield of 1.2%. For the point-contacts the yield was 0.7% and for the overlapping electrodes 0.5%. The Cr gaps having the highest trapping rate was expected due to their high aspect-ratio. However, the overlapping contacts were expected to have a higher trapping rate than the point-contact gaps. The low rate might be a result of the small sample size (only 2 chips) and the method of deposition: for one chip we drop-cast the solution, for the other we immersed the sample in the solution.

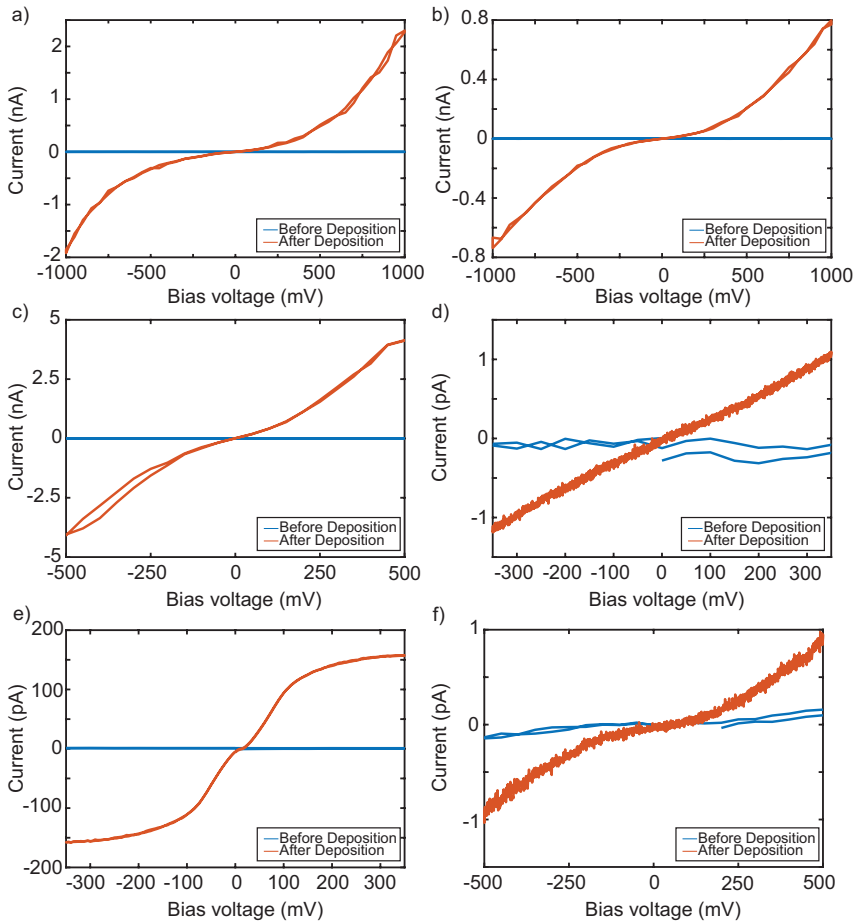


Figure 3.3: Current-voltage (IV) characteristics recorded at room-temperature before (blue) and after (orange) deposition of the nanoparticle solution. a,b,c) IV characteristics recorded on the point-contact gaps. The panels show 3 different junctions located on the same chip. d,e) IV characteristics recorded on the Cr nanogaps, on two separate chips. f) IV characteristic recorded on an overlapping electrode gap.

3.3.2. Low-temperature behaviour

All samples where something had been trapped, were cooled down to around 10 K and again IV characteristics were recorded. A representative example for each device geometry is shown in figure 3.4. Panel a) shows an IV which was recorded on a point-contact nanogap. A region with approximately zero current is observed between -7 and $+80$ mV. At positive bias, a large step in current occurs, while at negative bias several smaller steps are observed. These steps are not equally spaced: the first one is at -7 mV, the second one at -48 mV and the third at -105 mV. The overall line-shape is similar to Coulomb-Blockade (CB). On this chip, 3 junctions displayed the behavior showcased in panel a). The IV shown in panel b) was recorded on a Cr nanogap and the one in panel c) on an overlapping electrode nanogap. In both cases, no signal is observed above the noise level, up to a bias voltage of 1 V. All junctions on the Cr and overlapping geometries in which something was trapped, i.e., a signal was observed at room-temperature, did not display a current at low-temperature. Warming up the sample again restores the signal, and in the case of the sample in figure 3.3e even changes the line-shape.

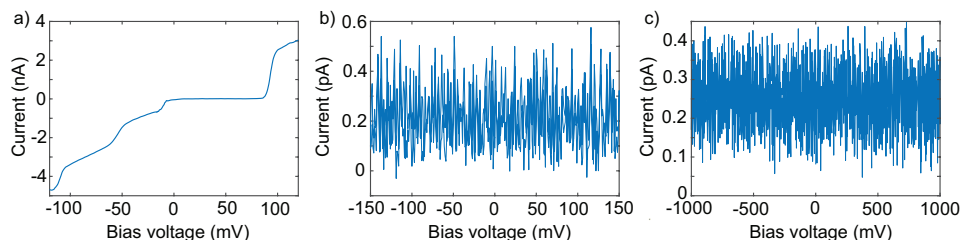


Figure 3.4: Low-temperature IVs for different device geometries, measured on chips where a particle was trapped. All IVs were recorded around 10 K. a) IV characteristic recorded on a point-contact nanogap. b) IV characteristic recorded on a Cr nanogap. c) IV characteristic recorded on an overlapping nanogap.

The junctions displaying CB-like features were gated by applying a voltage to the Si back-plane of the chip. By measuring IVs as a function of gate voltage we construct a stability diagram of the differential conductance as a function of bias and gate voltages. Figure 3.5 shows two stability diagrams in panels b) and d), together with an IV from each stability diagram. The IV in panel a) was recorded at a gate voltage of 5.5 V and exhibits a region with approximately zero current between -80 mV and $+160$ mV. After this region, steps in the current are observed: one step at negative bias and two steps at positive bias. The stability diagram in panel b) does not display a current between -50 and $+125$ mV; the steps in the IV correspond to the bright diagonal lines in the stability diagram. The bias voltage at which the step occurs shifts symmetrically towards lower bias voltages for increasing gate voltage. Figure 3.5c shows an IV recorded at a gate voltage of 3.0 V and also exhibits a region with approximately zero current between a bias voltage of 0 mV and $+75$ mV. Outside this region, steps in the current are observed with a spacing of about 50 mV. The stability diagram shown in panel d) shows current blockade between 0 mV and $+30$ mV. The bright diagonal lines correspond to the steps in the current

in the IVs, which shift symmetrically towards lower bias voltages with increasing gate voltage. Between a gate voltage of -4 and $+4$ V we vaguely observe diamond shapes, which is expected for CB.

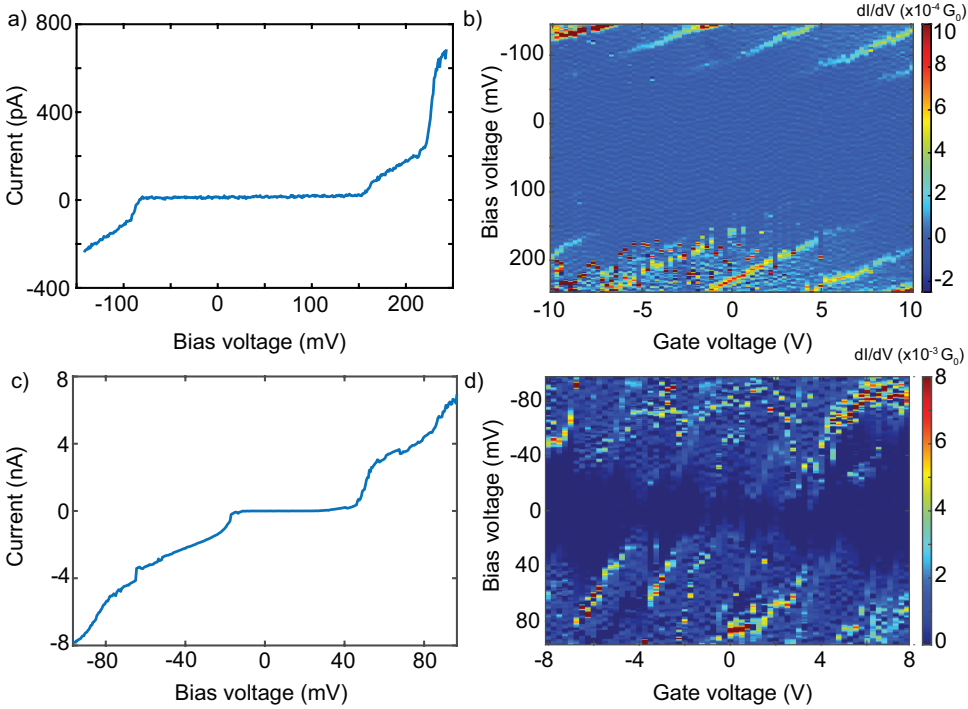


Figure 3.5: a) IV measured on a point-contact nanogap displaying Coulomb blockade-like features at a gate voltage of 5.5 V. b) Stability diagram recorded on the same junction as a). c) IV measured on a point-contact gap displaying Coulomb blockade-like features at a gate voltage of 3.0 V. d) Stability diagram recorded on the same junction as c).

As mentioned above, for the Cr gaps and the overlapping gaps, when a junction in which something had been trapped was cooled down the current vanished. Warming up the junction recovered the signal, which indicates that the particle is still inside the junction. A current which vanishes at low temperature usually indicates some type of thermally activated transport, where an electron must overcome an energy barrier. To investigate this further, we measured IVs as a function of temperature, as shown in figure 3.6a,c. Both measurements were performed on a Cr nanogap, on two different chips. A seemingly exponential decay of the current as a function of temperature is observed. Note that the current levels are at least two orders of magnitude smaller than the CB IV displayed in figure 3.5a,c.

In order to better display the decrease in current with decreasing temperature, we determine the conductance by fitting a linear function to the IVs in panels a)

and c) between -100 and +100 mV. The conductance obtained this way is plotted against inverse temperature in figure 3.6b,d. An exponential function of the form: $G \propto \exp(-E_a/k_B T)$ is fitted to the data, where E_a is the activation energy, k_B the Boltzmann constant and T the temperature. Good fits are obtained this way, with activation energies of respectively 0.52 and 0.35 eV.

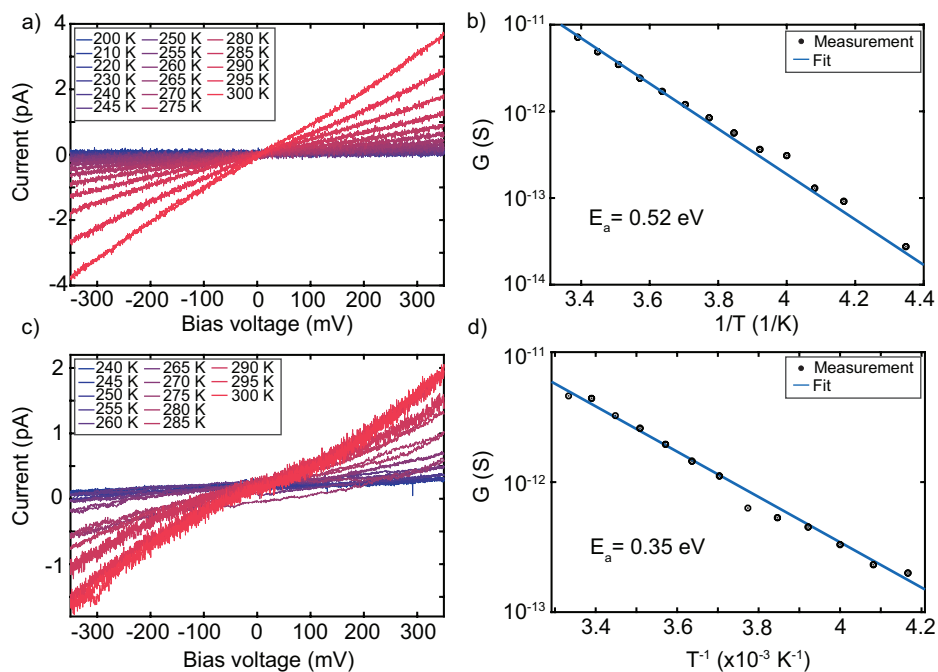


Figure 3.6: a) IVs recorded at different temperatures ranging between 200 K and 300 K in a Cr nanogap. b) Arrhenius fit of the differential conductance estimated from a) as a function of inverse temperature. c) Temperature dependence of another Cr nanogap in which a particle was trapped, measured on a different chip. d) Arrhenius fit of the differential conductance estimated from c) as a function of inverse temperature.

3.4. Discussion

The measured IV characteristics displayed two distinct behaviors: Coulomb blockade and thermally activated transport. We will discuss each separately and then discuss whether they can be reconciled into one coherent picture.

3.4.1. Coulomb blockade

In the point-contact nanogaps the observed current at room-temperature was significantly higher than for the other two geometries. Upon cooldown to around 10 K, the samples became even more conductive in most cases and the IVs started displaying a region around zero bias where the current was approximately zero, together with steps in the current as a function bias voltage. This behavior is expected in the case of CB: a small conducting island is separated from the two electrodes by a sufficiently large tunneling barrier, such that the tunneling conductances are much smaller than the conductance quantum: $G \ll G_0 = 2e^2/h$, with e the elementary charge and h Planck's constant. In this case the system behaves like a single-electron transistor (SET): the electron transport is dominated by single electron transfers [27]. In the case of a single conducting island sandwiched between two electrodes, the IV will display a region of zero current between $V = \pm e/C = \pm 2E_C/e$, with C the total capacitance of the island, E_C the charging energy of the conducting island and e the elementary charge ($1.6 \times 10^{-19} \text{ C}$). When the island is coupled asymmetrically to the electrodes, steps in the current are observed outside the suppressed region: the Coulomb staircase. These steps occur at intervals of e/C . Through a gate electrode it is possible to apply an electric field to the island, causing its chemical potential to shift. In a so-called stability diagram, the conductance is displayed as a function of bias voltage and gate voltage, resulting in diamond-shaped regions where current is blocked: Coulomb diamonds. The size of these diamonds and the slope of the edges provides information about how the island is coupled to the electrodes. When the coupling is asymmetric, the diamonds are skewed, meaning the IVs are asymmetric around zero bias.

Looking at the low temperature IVs which displayed CB-like behavior we distinguish two features: 1) a region with approximately zero current. This region is asymmetric around zero bias: the bias voltage value for which the current is suppressed is larger for positive bias voltage than it is for negative values, 2) steps in the current outside this suppressed region. These steps are not equidistant and the magnitude of the steps can be different. The two stability diagrams in figure 3.5 show that these steps move towards lower bias voltage values when the gate voltage is increased. In figure 3.5d it seems as though a couple of segments are present where the opposite happens and diamonds are formed. When the island is coupled asymmetrically, it is possible for only two of the four edges of the diamond to be visible. An asymmetric coupling, where the coupling with one electrode is much stronger than the coupling with the other electrode, is also the cause for the asymmetry of the region where the current is suppressed in the IVs.

The bias values at which the steps occur are not spaced equidistantly. Because the values at which these steps occur are related to the charging energy, this would suggest the presence of (at least) two different charging energies. This is the case when there are two or more particles in series, as has been observed, for example, in ferritin SETs [28]. When transport occurs through two or more particles in series, the current is blocked unless at least one energy level of each particle is within the bias window. In a stability diagram, this leads to non-closing diamonds. Although we do see a clear effect of applying a gate voltage, we do not observe a closing of the diamonds.

The presence of islands in series may be related to the core-shell structure that has been proposed as a model for PBA nanoparticles [23]. In such a structure, Trinh *et al.* [23] propose that the 11 nm CsCoFe nanoparticles consist of a well-crystallized core of around 7 nm with almost no vacancies, and a shell around it consisting of $\text{Fe(II)Co(III)Co(II)(H}_2\text{O)}_x\text{Fe(III)}$. In this case we can imagine the existence of a tunneling barrier between the well-crystallized core and the 'defective' shell. An electron could first tunnel from the source to an impurity state on the shell, before tunneling to the core and finally to the drain, as illustrated in figure 3.7. In this case we should observe two different charging energies, one larger (corresponding with the shell) and one smaller (corresponding with the core), as well as non-closing diamonds. Such a scheme has also been proposed by Labra-Munoz *et al.* [28] in their study on ferritin SETs, which have a core-shell structure as well; the core consists of the Fe ions whereas the shell is the protein-based container in which they are stored. It is important to note that we observed CB in three different junctions, all present on the same chip. Therefore, more measurements are needed to gain a better insight into the exact mechanism responsible for CB in these particles.

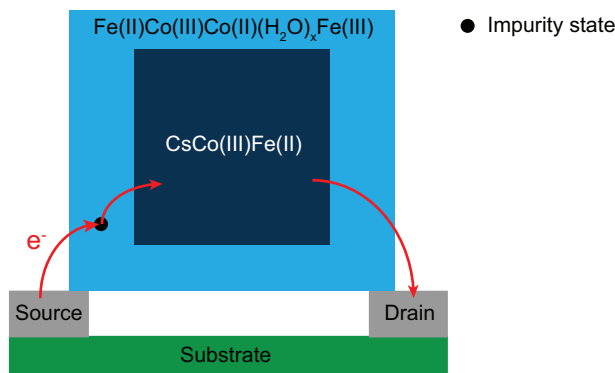


Figure 3.7: Schematic drawing of the core-shell structure and the electron tunneling process which would lead to the observed non-closing Coulomb diamonds: an electron first tunnels from the source electrode to an impurity state in the shell, before tunneling to the core and finally tunneling to the drain electrode.

3.4.2. Thermally activated transport

In both the Cr and the overlapping-electrode nanogaps, thermally activated transport was observed, as evidenced by the exponential decrease of the conductance as a function of temperature. This observation indicates the presence of an energy barrier. Within the context of our measurements, two scenarios are likely: either there is an energy barrier located between the electrodes and the particle, or the energy barrier is located in the particle itself due to disorder. In the former case, we have a barrier between a metal and a semiconductor, leading to a Schottky barrier. As discussed in the paper by Therssen *et al.*[20] the metal-CsCoFe-metal system can be modelled by a double Schottky barrier model. In the latter case we are dealing with a disordered semiconductor, such that an electron travelling through the particle has to overcome several energy barriers in a multi-step hopping process. In this context, we will discuss Efros-Shklovskii and Mott variable range hopping.

Double Schottky barrier

In the double Schottky barrier (DSB) model, two back-to-back Schottky diodes are considered. Each diode is characterized by a tunneling barrier $\phi_{1,2}$ and an ideality factor $n_{1,2}$ which accounts for the low dimensionality of the metal-semiconductor interfaces [29]. In the paper by Therssen *et al.*[20] a resistor is added in between the Schottky diodes which accounts for the intrinsic resistance of the nanoparticle. Within this model, the tunneling current I_T between the two electrodes is given by:

$$I_T = \frac{2I_{S1}I_{S2}\sinh\left(\frac{eU}{2k_B T}\right)}{I_{S1}\exp\left(-\frac{eU}{2k_B T n_1}\right) + I_{S2}\exp\left(\frac{eU}{2k_B T n_2}\right)}; \quad U = V - RI_T, \quad (3.1)$$

with e the elementary charge (1.6×10^{-19} C), k_B the Boltzmann constant (1.38×10^{-23} J K⁻¹), T the temperature, V the applied bias voltage, R the intrinsic resistance of the nanoparticle and $I_{S1,S2}$ the reverse saturation currents of the Schottky diodes, given by:

$$I_{S1,S2} = S_{1,2} A^* T^2 \exp\left(-\frac{\phi_{1,2}}{k_B T}\right), \quad (3.2)$$

with $S_{1,2}$ the area of the junctions, A^* the Richardson constant (1.2×10^6 Am⁻²K²) for free carriers [30]) and $\phi_{1,2}$ the effective Schottky barriers.

Therssen *et al.*[20] performed room temperature conductive AFM (C-AFM) measurements in ambient conditions. Their IVs were fitted to the DSB model with $\phi_{1,2}$, $n_{1,2}$ and R as fit parameters. Good fits were obtained, with values for $\phi_{1,2}$ between 0.28 and 0.43 eV, for $n_{1,2}$ between 1.21 and 1.5 and for R between 20 M Ω and 1.75 G Ω . The asymmetry between the barrier height is explained by their setup: the particle is located on top of an HOPG substrate and contacted at the top with a PtIr needle. Due to the different work functions, different barrier heights are expected.

Our setup differs in a few ways from the conducting atomic force microscope (C-AFM) setup: both electrodes are made of Pt, the contact area can be symmetric or asymmetric depending on how the particle is positioned in the gap and no mechanical contact (as with the needle in the AFM) is made, leading to worse contacts and thus larger tunneling barriers between particle and electrodes. In our case the nanogaps were all at least 15 nm wide, which is the size of the cubic particle. Therefore a configuration where the particle is inside the gap for the Cr nanogaps and on top for the overlapping-electrode nanogaps is likely, and the contact area with both electrodes is expected to be relatively symmetric. Under the assumptions that $S_1 = S_2 = S$ and $\phi_1 = \phi_2 = \phi$, equation 3.1 simplifies to:

$$I_T = \frac{2I_S \sinh\left(\frac{eU}{2k_B T}\right)}{\exp\left(-\frac{eU}{2k_B T_{n1}}\right) + \exp\left(\frac{eU}{2k_B T_{n2}}\right)}; \quad U = V - RI_T. \quad (3.3)$$

Due to stability reasons, our IVs were mostly measured up to 350 mV. As a result, the fitting of the IVs does not yield accurate estimates for the parameters. From equation 3.3 we see that the main scaling of the current with temperature is due to the exponential factor with $1/T$. Therefore we can obtain an estimate for the barrier heights from the temperature dependence in figure 3.5c,e. The values obtained this way are 0.52 and 0.35 eV, which are similar to the barrier heights that were measured with the C-AFM setup and determined from a detailed analysis of the IV characteristics.

While it is difficult to qualitatively compare our IVs to those of Therssen *et al.* due to our limited bias range, our samples do display a lower current than theirs. Since the particles are identical, we attribute this difference to our chip geometries. For the Cr gaps, the electrodes possess a height difference of 5-10 nm and a gap size of 15-25 nm. Given these parameters, it is most likely that the particle is located inside the gap, where it is unable to form a good contact with both electrodes due to its size. For the overlapping-electrode gaps, the gap size was 15-20 nm, leading to two possible contact configurations: one where the particle is inside the gap and does not make proper contact with both electrodes, and one where the particle is bridging the electrodes along its diagonal, which leads to a small contact area on both sides. In the case of the particle being located inside the gap, it cannot contact both electrodes properly due to the gap being larger than the particle. This poor contact leads to an additional tunneling barrier, resulting in a higher effective resistance.

We conclude that while our results can be explained within the DSB model, additional measurements are needed. These measurements should cover a larger bias range at different temperatures, allowing for the fitting of equation 3.1 to the data.

Mott variable range hopping and Efros-Shklovskii hopping

As described in the introduction, the CsCoFe nanoparticles possess a large amount of vacancies ($\sim 10\%$) [23]. Moreover, bulk PBAs have been shown to behave as a

semiconductor with a band gap of around 2 eV [21, 22]. Due to the large amount of vacancies, the particle can be considered a disordered semiconductor. Because disorder can lead to randomness, variable range hopping is a relevant transport mechanism to consider. Due to the disorder, bands are prevented from forming, which leads to localized charge carriers. Conduction then takes place through hopping between hopping centers [31]. Below a certain transition temperature these hops do not necessarily happen between nearest neighbors, but involve an optimization in energy difference between states and distance which maximizes the hopping probability. Here we will consider two models: Mott's variable range hopping (MVRH) in three dimensions and Efros-Shklovskii variable range hopping (ESVRH) [32, 33]. Within these models, the conductance is expected to decay as $\ln(G) \propto T^{-\beta}$ with $\beta = 1/2$ for ESVRH and $\beta = 1/4$ for 3D-MVRH. The difference between the two models is that within ESVRH electron-electron interactions are accounted for. For a more detailed explanation of the models, please refer to [32–34].

Within MVRH, different regimes are to be considered, depending on the applied electric field. In the low-bias regime, where $|e\bar{R}F| \ll k_B T$ with \bar{R} the average hopping distance and F the electric field, the conductance follows the relation:

$$G \propto \exp\left(-\frac{T_0}{T}\right)^{1/4}, \quad (3.4)$$

where T_0 is given by:

$$T_0 = \frac{24\alpha^3}{\pi k_B N_\mu}. \quad (3.5)$$

Here, α is the localization parameter, k_B the Boltzmann constant (8.617×10^{-5} eV K^{-1}) and N_μ the density of states around the Fermi level [33].

The average hopping distance is then given by:

$$\bar{R} = \frac{3}{4} \left(\frac{3}{2\pi\alpha N_\mu k_B T} \right)^{1/4}. \quad (3.6)$$

For the high-bias regime, the electric field provides enough energy for the hopping events and transport is field dominated. In this regime, the current is proportional to the electric field following:

$$I \propto \exp\left(\frac{F_0}{F}\right)^{1/4}, \quad (3.7)$$

with F_0 given by:

$$F_0 = \frac{81\alpha^4}{16\pi e N_\mu}. \quad (3.8)$$

Within ESVRH, electron-electron interactions are important and the temperature

dependence is adjusted. In this case, the conductance is expected to follow:

$$G \propto \exp\left(-\frac{T_0}{T}\right)^{1/2}, \quad (3.9)$$

with T_0 defined as:

$$T_0 \approx \frac{2.8e^2}{4\pi\epsilon\epsilon_0ak_B}, \quad (3.10)$$

where ϵ is the dielectric constant, ϵ_0 the vacuum permittivity and a the localization length [35].

We fitted a function of the form $\ln(G) = G_1 \exp(-T_0/T)^\beta$ to the conductance as a function of decreasing temperature for $\beta = 1/2$ and $1/4$ and obtain good fits as shown in figure 3.8. The values for T_0 are 5×10^5 and 14×10^9 K, corresponding with ESVRH and MVRH respectively. From the temperature dependence itself we cannot distinguish between Arrhenius behavior, MVRH or ESVRH. Therefore we try to estimate the localization length for both MVRH and ESVRH and determine whether these values are realistic.

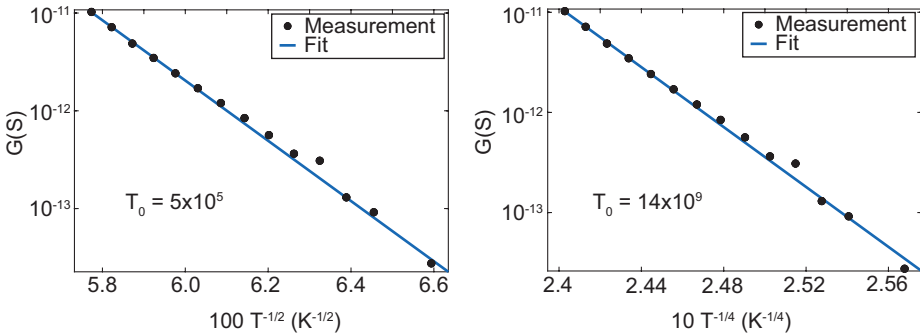


Figure 3.8: a) Differential conductance versus $T^{-1/2}$ for the sample in figure 3.5c. An exponential function of the form $\exp(-T_0/T)^{1/2}$ was fitted to the datapoints, resulting in the blue line. b) Differential conductance versus $T^{-1/4}$ for the sample in figure 3.5c. Here, an exponential function of the form $\exp(-T_0/T)^{1/4}$ was fitted to the datapoints.

In our measurements (fig. 3.5c,e) the current at ± 350 mV is temperature dependent, which means we are not in the high-bias regime. The conductance shown in figure 3.8a,b is determined by fitting a linear function to the IVs between ± 100 mV, hence we should approximately be in the low-bias regime. Therefore we use the equations for the low-bias regime to estimate the average hopping distance within the 3D-MVRH model. Equation 3.6 shows that we need an estimate for the density of states around the Fermi level. We can obtain a rough estimate for the density of states based on the stability diagram in figure 3.5b. In Coulomb diamonds, lines

parallel to the diamond edges at a distance of the level spacing are expected. As those are absent, the level spacing should be smaller than the resolution of that measurement. Because the resolution of this measurement was around 2 mV, we obtain a lower bound for the density of states:

$$N_{\mu} \approx \frac{1}{L^3 \Delta E} > \frac{1}{(15 \times 10^{-9})^3 \cdot 2 \times 10^{-3}} = 1.48 \times 10^{26} \text{ eV}^{-1} \text{ m}^{-3} \quad (3.11)$$

with L the size of the system and ΔE the level spacing. With this estimate and the fitted value for $T_0 = 14 \times 10^9$ we can use equation 3.5 and 3.6 to obtain an upper bound for the average hopping distance. The value for the average hopping distance obtained this way is 1.1 nm, which is around the same as the lattice constant of $\sim 10 \text{ \AA}$ [23]. This would indicate that electrons hop from unit cell to unit cell to cross the particle, which would be more in line with the nearest neighbor hopping model. For nearest neighbor hopping, the conductance is expected to scale with $\exp(-1/T)$, which we observe as shown in figure 3.5d,f. However, with our data we cannot distinguish between nearest neighbor hopping and the double Schottky barrier model.

For ESVRH we obtained a value for $T_0 = 5 \times 10^5 \text{ K}$, which we can use in equation 3.10. The obtained localization length is $a = 93/\epsilon \text{ pm}$. Considering the radius of atoms is of the order of 100 pm, we can conclude that the ESVRH model can be discarded as an explanation of the observed behavior.

3.4.3. Reconciling the two observed behaviors

Two different types of behavior are observed in different chip geometries. Coulomb blockade is observed in the point-contact nanogaps, and thermally activated transport is seen in both the Cr and the overlapping-electrode nanogaps. This indicates that depending on how the particle is contacted, the observed behavior changes. In the case of CB, tunneling barriers are present between the electrodes and the nanoparticle, which is a conducting island. At low temperature, such that $k_B T \ll E_C$, the conductance is still high enough to measure and we are able to observe a Coulomb staircase. In the case of the thermally activated transport, which was observed in the Cr and the overlapping-electrode nanogaps, the room-temperature conductance was much lower than that of the chips displaying CB. At low temperature no signal was observed. From this we can conclude that the tunnel barriers are smaller for the point-contact gaps. A possible explanation for this difference is the gap size: only for the point-contact geometry were we able to achieve gap sizes smaller than the size of the particle. In the two other geometries, a particle can be inside the gap or bridging the two electrodes over its diagonal. In both cases, the contact is poor and a larger effective tunnel barrier is expected.

3.5. Conclusion

In conclusion, we managed to trap one or more nanoparticles on all three device geometries with different rates of success. Immersing the sample in a diluted solution yields the highest trapping rates. The Cr nanogaps have the highest trapping rate, which is to be expected due to their large gap width. The overlapping-electrode nanogaps have the lowest trapping rate, which is unexpected because the gap width is large compared to that of the point-contacts. However, only two of these chips were measured; on one the solution was drop-cast, the other was submerged in solution. The low trapping yield is probably due to the small sample size and method of deposition.

The room-temperature measurements show that the point-contact gaps have the highest conductance. Upon cooldown, the point-contact gaps display CB, whereas the Cr and overlapping-electrode nanogaps do not display a current. The features of the observed CB indicate that we are not measuring a single nanoparticle, but rather two or more particles in series with different sizes. The temperature dependence of the IVs recorded on the two Cr nanogaps shows that the conductance decreases exponentially with $1/T$. Arrhenius fits yield activation energies of 0.52 and 0.35 eV. These values are compared to the ones obtained in a C-AFM study where the double Schottky barrier model is used to explain their findings [20]. The obtained values for the barrier are similar to the ones they obtain through fitting the model to their IVs. The data was also considered within Mott's and Efros-Shklovskii's variable range hopping models and good fits to the expected temperature dependence of the conductance were obtained. Within these models, estimations are made for the average hopping distance. For MVRH we obtain a value smaller than 1.1 nm and for ESVRH we obtain a value of $93/\epsilon$ pm. The value obtained for MVRH is about the size of the unit cell, which would be more in line with nearest neighbor hopping. The value for ESVRH shows that our data is not captured by the model. The different behaviors we observe for the different geometries can be explained by the difference in gap size between the geometries. The point-contact had gap sizes smaller than the particle, whereas the other two geometries had gaps larger than the particle. Due to poor contacting in the latter cases, larger effective barriers are expected between the nanoparticle and the electrodes, leading to a much lower conductance. For the point-contact devices the tunnel barriers are apparently thin enough to facilitate the observation of Coulomb blockade physics at the lowest temperatures that were probed in our measurements.

3.6. Appendix

3.6.1. Fabrication recipe point-contact nanogaps

These are the steps for fabricating the point-contact nanogaps used in this chapter:

1. Spincoat a layer of AR-P 6200.04 at a rate of 4000 rpm. Bake the resist at 185 °C for 3 minutes.
2. Expose the resist with the e-beam to lithographically define the point-contacts. We use an acceleration voltage of 100 kV and an aperture of 400 μm . For the coarse structures a beam current of 160 nA is used, for the fine structures a beam current of 918 pA. A dosetest is necessary to determine the optimal dose.
3. Cold development of the resist:
 - Pre-cool a beaker in the fridge for at least 1 hour.
 - Take pentyl acetate from the freezer and pour it in the pre-cooled beaker.
 - Submerge the substrate for 1 minute while moving it gently.
 - Put the substrate in xylene for 5 seconds as a liquid descum.
 - Spray the substrate with IPA while moving it to a beaker with IPA and soak it for at least 30 seconds.
 - Blow-dry with an N_2 gun.
4. Evaporate metals in an e-beam evaporator such as the Temescal or MB-AJA. We do not rotate the stage while evaporating. First evaporate 5 nm Ti at 0.5 $\text{\AA}/\text{s}$, followed by 30 nm Pt at 1.0 $\text{\AA}/\text{s}$.
5. Lift off using anisole heated to 80 °C or AR-600-71 heated to 70 °C. Leave it for an hour, when taking it out, first sonicate at P=5 for 5 minutes. Then spray with IPA while taking it out and soak in IPA for 1 minute.

References

- [1] P. Gütlich, *Spin Crossover – Quo Vadis?* *European Journal of Inorganic Chemistry* **2013**, 581 (2013).
- [2] A. Bousseksou, G. Molnár, L. Salmon, and W. Nicolazzi, *Molecular spin crossover phenomenon: recent achievements and prospects*, *Chemical Society Reviews* **40**, 3313 (2011).
- [3] G. Molnár, S. Rat, L. Salmon, W. Nicolazzi, and A. Bousseksou, *Spin Crossover Nanomaterials: From Fundamental Concepts to Devices*, *Advanced Materials* **30** (2018), 10.1002/adma.201703862.
- [4] P. Gütlich and H. Goodwin, eds., *Spin Crossover in Transition Metal Compounds I*, Topics in Current Chemistry, Vol. 233 (Springer Berlin Heidelberg, Berlin, Heidelberg, 2004).
- [5] K. Kaushik, S. Mehta, M. Das, S. Ghosh, S. Kamilya, and A. Mondal, *Stimuli-responsive magnetic materials: impact of spin and electronic modulation*, *Chemical Communications* **59**, 13107 (2023).
- [6] P. Gütlich, Y. Garcia, and H. A. Goodwin, *Spin crossover phenomena in Fe(ii) complexes*, *Chemical Society Reviews* **29**, 419 (2000).
- [7] J.-F. Létard, P. Guionneau, and L. Goux-Capes, *Towards Spin Crossover Applications*, in *Spin Crossover in Transition Metal Compounds III* (Springer-Verlag, Berlin/Heidelberg) pp. 221–249.
- [8] N. Amin, S. Said, M. Salleh, A. Afifi, N. Ibrahim, M. Hasnan, M. Tahir, and N. Hashim, *Review of Fe-based spin crossover metal complexes in multiscale device architectures*, *Inorganica Chimica Acta* **544**, 121168 (2023).
- [9] Y. Huang and S. Ren, *Multifunctional Prussian blue analogue magnets: Emerging opportunities*, *Applied Materials Today* **22**, 100886 (2021).
- [10] N. Kitchamsetti, *A review on recent advances in Prussian blue, its analogues, and their derived materials as electrodes for high performance supercapacitors*, *Journal of Energy Storage* **73**, 108958 (2023).
- [11] Z. Qin, Y. Li, and N. Gu, *Progress in Applications of Prussian Blue Nanoparticles in Biomedicine*, *Advanced Healthcare Materials* **7** (2018), 10.1002/adhm.201800347.
- [12] K. Tang, X. Li, Y. Hu, X. Zhang, N. Lu, Q. Fang, J. Shao, S. Li, W. Xiu, Y. Song, D. Yang, and J. Zhang, *Recent advances in Prussian blue-based photothermal therapy in cancer treatment*, *Biomaterials Science* **11**, 4411 (2023).
- [13] L. Catala and T. Mallah, *Nanoparticles of Prussian blue analogs and related coordination polymers: From information storage to biomedical applications*, *Coordination Chemistry Reviews* **346**, 32 (2017).

- [14] M. Cammarata, S. Zerdane, L. Balducci, G. Azzolina, S. Mazerat, C. Exertier, M. Trabuco, M. Levantino, R. Alonso-Mori, J. M. Glowia, S. Song, L. Catala, T. Mallah, S. F. Matar, and E. Collet, *Charge transfer driven by ultrafast spin transition in a CoFe Prussian blue analogue*, *Nature Chemistry* **13**, 10 (2021).
- [15] D. Aguilà, Y. Prado, E. S. Koumoussi, C. Mathonière, and R. Clérac, *Switchable Fe/Co Prussian blue networks and molecular analogues*, *Chemical Society Reviews* **45**, 203 (2016).
- [16] V. Escax, A. Bleuzen, C. Cartier dit Moulin, F. Villain, A. Goujon, F. Varret, and M. Verdaguer, *Photoinduced Ferrimagnetic Systems in Prussian Blue Analogues $C I x Co 4 [Fe(CN) 6] y$ ($C I =$ Alkali Cation). 3. Control of the Photo- and Thermally Induced Electron Transfer by the $[Fe(CN) 6]$ Vacancies in Cesium Derivatives*, *Journal of the American Chemical Society* **123**, 12536 (2001).
- [17] D. M. Pajerowski, T. Watanabe, T. Yamamoto, and Y. Einaga, *Electronic conductivity in Berlin green and Prussian blue*, *Physical Review B* **83**, 153202 (2011).
- [18] S. Cobo, G. Molnár, F. Carcenac, P. Á. Szilágyi, L. Salmon, C. Vieu, and A. Bousseksou, *Thin Films of Prussian Blue: Sequential Assembly, Patterning and Electron Transport Properties at the Nanometric Scale*, *Journal of Nanoscience and Nanotechnology* **10**, 5042 (2010).
- [19] R. Bonnet, S. Lenfant, S. Mazérat, T. Mallah, and D. Vuillaume, *Long-range electron transport in Prussian blue analog nanocrystals*, *Nanoscale* **12**, 20374 (2020).
- [20] H. Therssen, L. Catala, S. Mazérat, T. Mallah, D. Vuillaume, T. Mélin, and S. Lenfant, *Electronic properties of single Prussian Blue Analog nanocrystals determined by conductive-AFM*, *Nanoscale* **15**, 19128 (2023).
- [21] J. C. Wojdeł, I. de P. R. Moreira, S. T. Bromley, and F. Illas, *On the prediction of the crystal and electronic structure of mixed-valence materials by periodic density functional calculations: The case of Prussian Blue*, *The Journal of Chemical Physics* **128** (2008), 10.1063/1.2824966.
- [22] S. Watanabe, Y. Sawada, M. Nakaya, M. Yoshino, T. Nagasaki, T. Kameyama, T. Torimoto, Y. Inaba, H. Takahashi, K. Takeshita, and J. Onoe, *Intra- and interatomic optical transitions of Fe, Co, and Ni ferrocyanides studied using first-principles many-electron calculations*, *Journal of Applied Physics* **119** (2016), 10.1063/1.4954070.
- [23] L. Trinh, S. Zerdane, S. Mazérat, N. Dia, D. Dragoe, C. Herrero, E. Rivière, L. Catala, M. Cammarata, E. Collet, and T. Mallah, *Photoswitchable 11 nm CsCoFe Prussian Blue Analogue Nanocrystals with High Relaxation Temperature*, *Inorganic Chemistry* **59**, 13153 (2020).

- [24] J. Glatz, J.-R. Jiménez, L. Godeffroy, H. J. von Bardeleben, L. Fillaud, E. Maisonhaute, Y. Li, L.-M. Chamoreau, and R. Lescouëzec, *Enlightening the Alkali Ion Role in the Photomagnetic Effect of FeCo Prussian Blue Analogues*, *Journal of the American Chemical Society* **144**, 10888 (2022).
- [25] D. Bouwmeester, *Superconducting Contacts for Atomically Precies Graphene Nanoribbons*, *Ph.D. thesis*, Delft University of Technology (2024).
- [26] R. Schouten, *QT Designed Instrumentation*, <https://raith.com/technology/nanofabrication-software/proximity-effect-correction/>, accessed: 3-5-2024.
- [27] Y. V. Nazarov and Y. M. Blanter, *Quantum Transport* (Cambridge University Press, 2009).
- [28] J. A. Labra-Muñoz and H. S. J. van der Zant, *Ferritin Single-Electron Transistor*, *The Journal of Physical Chemistry B* **128**, 6387 (2024).
- [29] A. Grillo and A. Di Bartolomeo, *A Current–Voltage Model for Double Schottky Barrier Devices*, *Advanced Electronic Materials* **7** (2021), 10.1002/aelm.202000979.
- [30] C. Crowell, *The Richardson constant for thermionic emission in Schottky barrier diodes*, *Solid-State Electronics* **8**, 395 (1965).
- [31] V. Janssen, *Electronic Properties of (Pseudo-) Two-Dimensional Materials*, *Ph.D. thesis*, Delft University of Technology (2020).
- [32] B. I. Shklovskii and A. L. Efros, *Electronic Properties of Doped Semiconductors*, Springer Series in Solid-State Sciences, Vol. 45 (Springer Berlin Heidelberg, Berlin, Heidelberg, 1984).
- [33] J. Hapert, *Hopping Conduction and Chemical Structure: a study on Silicon Suboxides*, *Ph.D. thesis*, Utrecht University (2002).
- [34] N. F. Mott, *Conduction in non-crystalline materials*, *Philosophical Magazine* **19**, 835 (1969).
- [35] D. Yu, C. Wang, B. L. Wehrenberg, and P. Guyot-Sionnest, *Variable Range Hopping Conduction in Semiconductor Nanocrystal Solids*, *Physical Review Letters* **92**, 216802 (2004).

4

Electronic Characterization of a Mn(III) Spin Crossover Single-Molecule Junction

Abstract

Single-molecule electronic transport measurements are presented on a Manganese(III) spin crossover (SCO) complex with a total spin, $S = 1$, low-spin (LS) and a high-spin (HS) state with $S = 2$. A mechanically-controlled break junction (MCBJ) setup was used to perform measurements at both room temperature and at 6 K. The fast-breaking measurements at room temperature show a molecular plateau in the conductance as a function of electrode separation at a conductance of $3 \times 10^{-5} G_0$, with $G_0 = e^2/h$ the conductance quantum. Comparison with the ligand of the molecule which shows tunneling behavior, indicates that the Mn center changes the electronic transport characteristics of the molecule. At cryogenic temperature, current-voltage (IV) characteristics are recorded while the conductance of the junction is lower than $1 G_0$ and above the noise level. Three features can be distinguished in the IVs: a large, wide conductance peak which is observed in around half of all IVs, a zero-bias conductance peak, also known as a Kondo resonance, which is observed in about 6% of all IVs, and a step in the conductance, observed in around 7% of all IVs, which is indicative of inelastic tunneling spectroscopy (IETS) and is observed when the bias voltage is large enough to excite a vibrational mode or facilitate a spin-flip. The large, wide conductance peak was found to shift as much as 50 mV in a single breaking trace and is therefore attributed to a molecular orbital close to the Fermi energy (mechanical gating). The behavior of the Kondo resonance in a magnetic field was compared to what is expected for a spin-1/2 system. We found that the splitting, as well as the suppression of the peak was significantly stronger than one would expect for a spin-1/2 system. Looking at the IVs which display IETS, we observe a characteristic width of 10 - 30 mV.

High-voltage IVs were recorded in an attempt to drive the spin-state switch through an electric field. The bias voltage was swept from -1 V to +1 V and back. Jumps in the current were observed at high bias voltage, both positive and negative, indicating a switch in the conductance state. In around 10% of the high-voltage IVs the switch was reversible, also known as memristance.

4.1. Introduction

Molecular electronics is the field which aims to create molecular building blocks for integrated circuits. To this end, molecules are required to exhibit functionalities such as rectification [1, 2], switching [3, 4] and sensing [5, 6]. One such functionality is spin switching, where the molecule can reversibly switch between two distinct spin states through external stimuli such as light, temperature, magnetic field or mechanical stress [7–9]. Because a switch in spin state is often accompanied by a structural change, many of these compounds exhibit a hysteresis in the transition temperature. These properties allow for the use of these molecules as switches, sensors, transistors and memory devices. Two main methods can be distinguished for performing nanoscale experiments on single molecules: scanning probe experiments using a scanning tunneling microscope (STM) [10, 11] or using break junctions. The break junction experiments can be subdivided in mechanically controlled break junctions (MCBJs) [12, 13], electromigrated break junctions (EMBJs) [14] and electroburned graphene break junctions [15]. STM experiments allow for the molecule to be imaged, but the technique lacks scalability, which is required for applications. Break junctions allow for the integration of a gate electrode, thereby creating a spin transistor in which it is possible to reversibly oxidize / reduce the molecule. This technique is scalable and measures molecules in an environment that is most similar to an integrated device.

The first steps towards applications involve the determination of the spin state of the molecule. For bulk crystals this can be done through magnetic susceptibility studies, however at the nanoscale this is not possible and the spin state needs to be determined by analyzing the electronic transport. Several groups have reported on being able to distinguish the high-spin (HS) and low-spin (LS) state in Fe(II) complexes. Miyamachi *et al.* observed memristive behavior in the current-voltage (IV) characteristics, where the resistance depends on the history of the applied voltage, and used Kondo physics to show that the high conductance state corresponds with the HS state. They demonstrate that the spin state can be switched through the application of voltage pulses [16]. Another way to determine the spin state was reported by Bairagi *et al.*. In Fe(II) complexes, the metal-ligand bond length can change as much as 10% between the LS and HS state, which alters the vibrational spectrum of the molecule [17]. By looking at the differential conductance characteristics, vibrational modes (or other inelastic processes) can be recognized by a step, a phenomenon known as inelastic tunneling spectroscopy (IETS). When the bias voltage is equal or larger than the energy of such a vibrational mode, it is possible for an electron to excite this vibrational mode while still contributing to

transport, effectively opening an additional conductance channel which leads to a step-like increase of the conductance at both negative and positive bias voltage. In their study, density functional theory (DFT) calculations were used to calculate the vibrational coupling constants for both the LS and the HS state. The HS state was strongly coupled to two vibrational modes, whereas the LS state was not. Looking at IV characteristics, they were able to observe both conductance states and switch from the LS to the HS state using light [18]. Finally, a study by Burzuri *et al.* reported on the observation of two distinct IV curves: one with a small gap and one with a large gap, after this gap the differential conductance displayed a large peak, corresponding with the closest frontier orbital. DFT studies indicated a reconfiguration of the orbital energies upon switching between the two spin states, where the HS state corresponded with the small gap state [9].

In this study, we employ an MCBJ setup to perform electronic transport measurements at cryogenic temperature on a Manganese(III) SCO complex (shown in figure 4.1a). All studies mentioned in the previous paragraph involve SCO molecules based on Fe(II), which possesses an LS state with total spin $S = 0$ and an HS state with $S = 2$. No studies exist where similar measurements are performed on a Manganese(III) complex, which is known to exhibit SCO behavior when surrounded by ligands in an octahedral symmetry. The key difference between the two lies in the spin states: the LS state of Mn has $S = 1$ and the HS state $S = 2$ (see figure 4.1b). We investigate how the charge transport is affected and whether the spin switch can be observed by looking at the earlier-mentioned phenomena: Kondo physics, IETS, memristance and orbital reconfigurations. The molecules in this chapter were synthesized by the group of Prof. Dr. A. Mondal in Bangalore, India. We characterize the molecule with fast-breaking measurements at room temperature, record IV characteristics at cryogenic temperature and discuss the different types of behavior we observe.

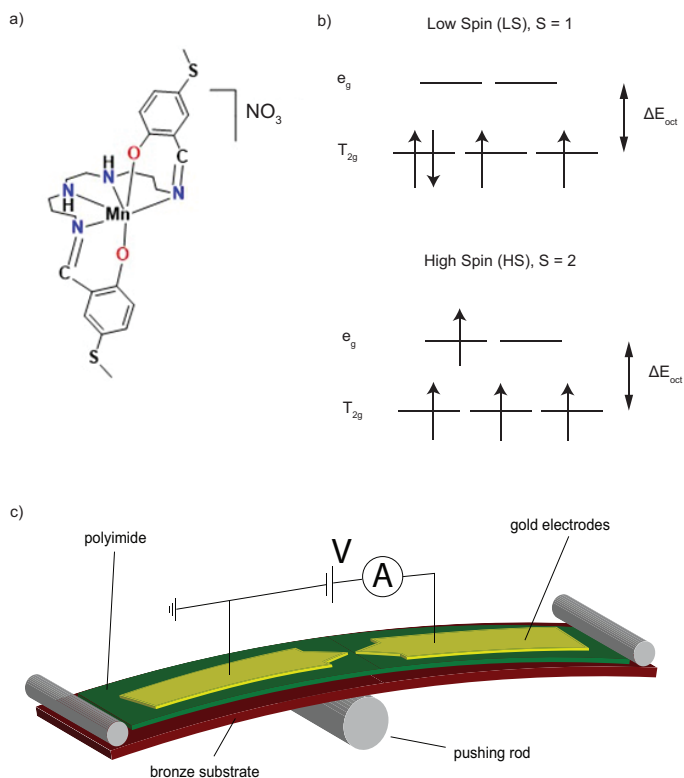


Figure 4.1: a) Structure of the Manganese complex; the thiol groups on both ends act as anchoring groups. b) Energy diagrams of the low-spin (LS) and high-spin (HS) state of the Mn complex. The LS state has a net spin of 1 and the HS state a spin of 2. c) Schematic of the two-terminal mechanically controlled break junction setup.

4.2. Methods

A Manganese(III) SCO complex (see figure 4.1a) was measured in an MCBJ setup at both room- and cryogenic temperature. In the MCBJ setup (see figure 4.1c), a gold wire is gradually stretched by bending the bronze substrate. Eventually the gold wire ruptures, leading to a snap-back of the electrodes after which a sub-nm gap remains; this gap can be bridged by one or more molecules, leading to a molecular junction [19]. At room temperature, the molecule was characterized through fast-breaking measurements, where the conductance is measured while opening the gap. At a certain point the gap becomes too large to bridge for a molecule and the junction breaks, causing the conductance to drop below the noise level. One such measurement is called a breaking trace. In fast-breaking measurements, sets of thousands of breaking traces are obtained, from which characteristics such as the molecular conductance can be derived. Prior to drop-casting a solution containing the Mn complex on the chip, the bare gold junctions were characterized to confirm their cleanliness (see Appendix figure 4.9). A solution is made with a molecular

concentration of approximately 0.1 mMol, of which a 3 μ L droplet is drop-cast on the chip. After the solution has dried, the sample space is closed off and, in the case of cryogenic temperature measurements, pumped to a vacuum.

At room temperature, fast-breaking measurements are performed, which are then analyzed by using a machine learning algorithm to separate different types of behavior [20]. At cryogenic temperature, the increased junction stability allows for the measuring of current-voltage (IV) characteristics, as well as magnetic field measurements. Due to the lack of a piezo element at cryogenic temperatures, the breaking of the junction is done with the motor, allowing us to open the gap in steps of around 0.15 μ m. Breaking traces are measured, but when the conductance drops below $1 G_0$, IVs are recorded for each electrode separation: the bias voltage is varied and the resulting current is measured. Afterwards, a Savitzky-Golay filter was applied to the IVs to obtain differential conductance vs. bias voltage traces.

4.3. Results and discussion

Fast-breaking measurements were performed on the Mn(III) complex, as well as its ligand (shown in appendix figure 5.8a). Figure 4.2a shows a dataset of 10,000 traces measured at a bias voltage of 100 mV. No clear molecular feature is present, therefore a machine learning algorithm [20] is used to filter out the tunneling traces. Panel b shows a two-dimensional histogram of the breaking traces which were labeled as containing no molecule. Panel c displays the remaining traces (around 5%), which are labeled as being molecular. In the histogram of this molecular class, a high density of counts is observed around $3 \times 10^{-5} G_0$, where $G_0 = 2e^2/h$ with e the elementary charge 1.6×10^{-19} C and $h = 4.136 \times 10^{-15}$ eV/Hz the Planck constant. On the right the one-dimensional histogram is shown, which is obtained by summing the data over all electrode displacements. A peak is present at $3 \times 10^{-5} G_0$, which is the molecular conductance. The same analysis is done for the ligand in order to compare the data and determine whether the presence of the Mn center affects the electronic transport. For comparison, the one-dimensional histogram of the ligand is shown as the drawn green line in figure 4.2c. The fast-breaking measurement of the ligand is discussed in the appendix in section 4.5.2. Important to note is the peak just below $10^{-6} G_0$ for both molecules; this is an artifact of the amplifier and not a molecular feature. For the ligand, no molecular plateau is observed; breaking traces are observed which decay exponentially in conductance with increasing electrode displacement, suggesting that single-barrier electron tunneling is the dominant transport mechanism. However, the decay of the conductance is slower than the one observed for a bare gold junction. Most likely, the presence of the ligand on the gold influences the work function and thereby the barrier for direct tunneling across the gap formed by the two gold electrodes [21]. A new chip was prepared with the Mn(III) complex for the low temperature setup. The sample space was pumped to a vacuum below 10^{-4} mbar, after which it is submerged in liquid helium. The increased junction stability at cryogenic temperature leads to the observation of molecular plateaus between 1 and $10^{-5} G_0$; three examples of breaking traces are shown in figure 4.3. Each point represents a step in the electrode separation of around 15 μ m. As can be seen in the graph, the

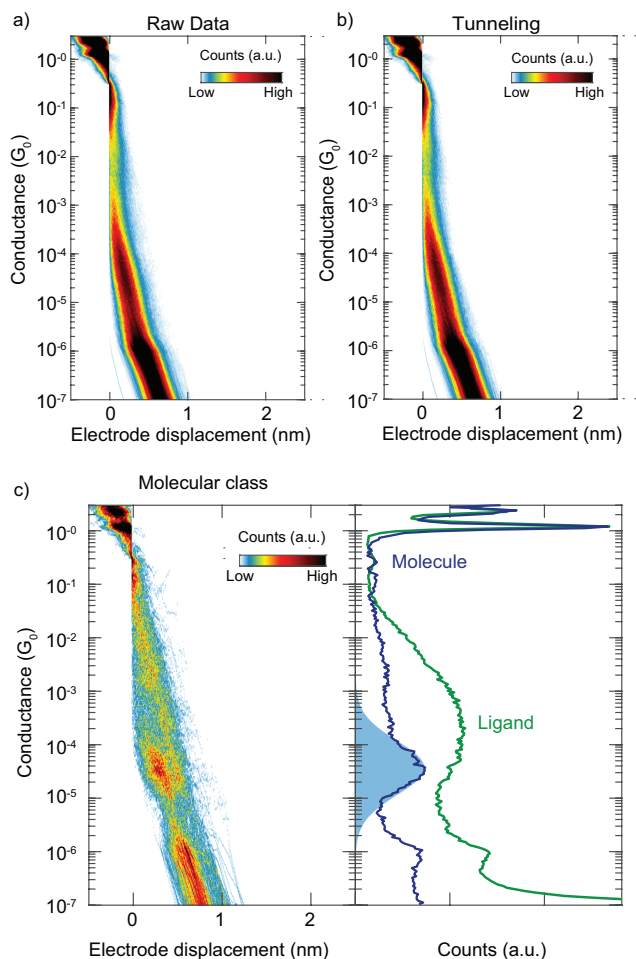


Figure 4.2: Two-dimensional histogram of the fast-breaking measurements on the Mn complex. a) Histogram constructed from 10.000 traces showing the raw data measured at a constant bias voltage of 100 mV. b) Two-dimensional histogram of the traces which were classified as tunneling by a neural networks model. c) Two-dimensional histogram of the data labeled as molecular by a neural networks model, with a one-dimensional histogram on the right. A peak is observed at $3 \times 10^{-5} G_0$. For reference, the one-dimensional histogram of the ligand (see also fig 4.10) is also shown here as the green line. The peak just below $10^{-6} G_0$ is an artifact of the amplifier and not a molecular feature.

conductance displays a sharp drop around $1 G_0$, after which a molecular junction forms and the conductance remains relatively constant with increasing electrode separation. For each of the points after this sharp drop, IVs were recorded: in total 2164 obtained in 109 breaking traces.

In these IVs, three different features were distinguished, as shown in figure 4.4. On the left, the IV is characterized by a low-conductance region around zero bias, followed by an abrupt drastic increase at -30 mV. This is reflected in the differential

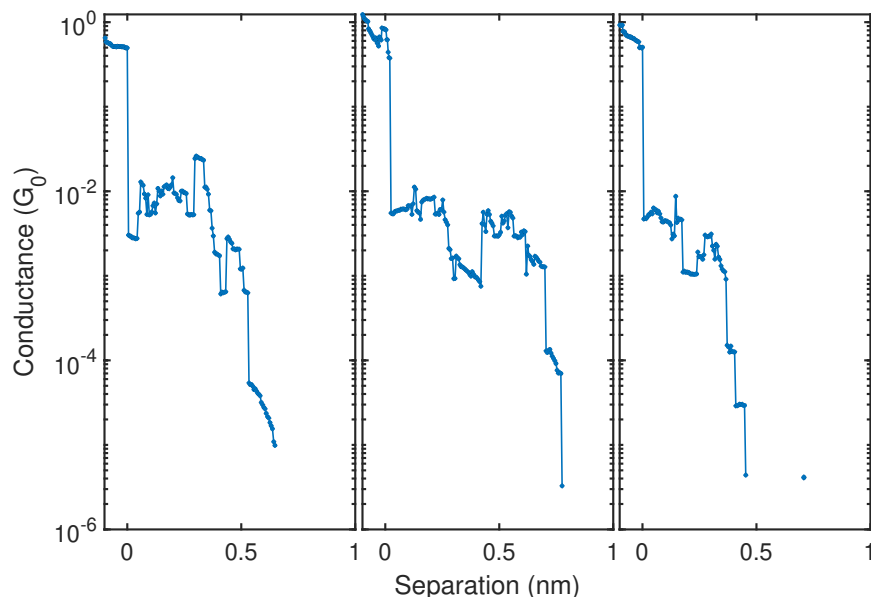


Figure 4.3: Three examples of breaking traces which display a molecular plateau measured in a vacuum at cryogenic temperature. Dots represent measurement points. At each dot below a conductance of $1 G_0$ a current-voltage characteristic was recorded.

conductance as a sharp peak, which is often larger than one order of magnitude. In some cases, two peaks were observed, symmetric around zero bias. Large-amplitude peaks were observed in approximately half of all IVs and are the most prevalent feature. These peaks often shifted with increasing electrode separation. An example is discussed in the appendix section 4.5.3.

The second characteristic behavior is shown in the middle panels: the differential conductance displays a zero-bias peak. Such a zero-bias peak was observed in around 130 IVs and may indicate the presence of a Kondo resonance, as this has been reported before for similar molecules [22–29]. The observation of a Kondo resonance would confirm that the non-zero spin character of the Mn(III) complex persists when captured in the break junction.

Finally, on the right a flat region in the conductance is observed around zero bias voltage, followed by a step in the conductance. Such a step-like feature is usually the result of an inelastic process being energetically accessible and is called inelastic tunneling spectroscopy (IETS). In the case of a system with a spin, it is possible that this is a spin-flip (SF) excitation, also called SF-IETS. Alternatively, coupling to vibrational modes may also lead to a similar IETS feature, where the position of the step reflects the energy of the vibrational mode involved. Such a line shape is observed in around 150 IVs.

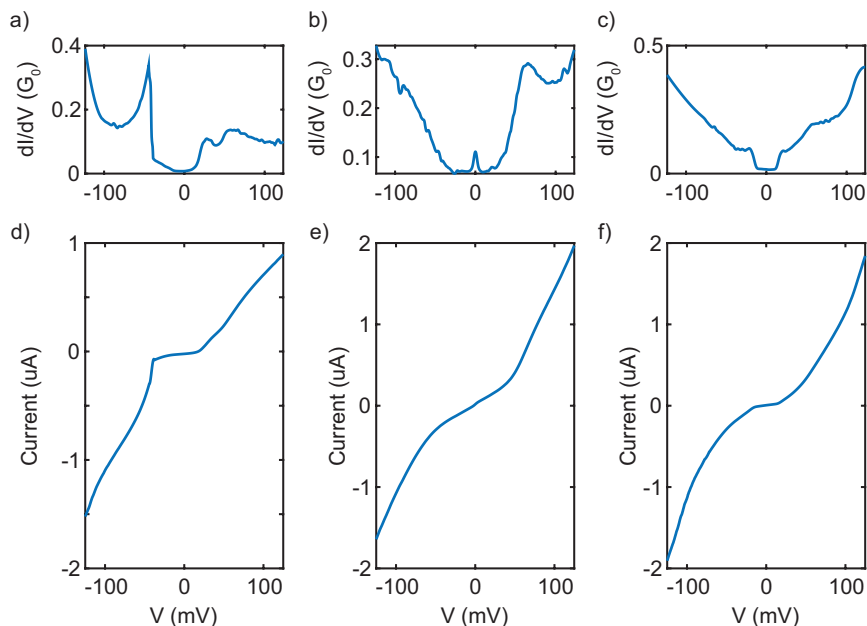


Figure 4.4: Three examples of different behaviors observed in the current-voltage (IV) characteristics. The upper row displays the differential conductance obtained from the IV below it. On the left a sharp peak is observed in the differential conductance at -50 mV, this peak is interpreted as an orbital due to its size and width. In the middle a Kondo resonance is observed at zero bias voltage, followed by an increase in conductance. On the right a flat region followed by a step in the conductance is observed, this is attributed to inelastic tunneling spectroscopy.

As mentioned in the introduction, the Mn(III) complex possesses two spin states, one with $S = 1$ and one with $S = 2$. Previous studies have been able to identify the spin state through phenomena such as Kondo physics and IETS. Because both states possess a non-zero spin, we first focus on these spin-related phenomena. A Kondo resonance is the result of the (partly) screening of the molecular spin by the electrons in the electrodes, leading to an enhanced conductance at the Fermi energy [30]. In order to observe the Kondo effect, the system temperature needs to be below the characteristic Kondo temperature, T_K . The higher the Kondo temperature, the stronger the coupling between the electrodes and the molecular spin, as can be seen from the Haldane relation [31]:

$$k_B T_K = \sqrt{\frac{U\Gamma}{2}} e^{\pi\epsilon_0(\epsilon_0 - U)/U\Gamma}, \quad (4.1)$$

where $\Gamma = \Gamma_L + \Gamma_R$ is the sum of the electronic coupling between the molecule and the left and right electrodes ($\Gamma_{L,R}$), U the Coulomb repulsion energy, ϵ_0 the energy of the level through which electron transport occurs and k_B the Boltzmann constant (8.617×10^{-5} eV/K). The universal scaling behavior of this zero-bias resonance as

a function of temperature is the best way to confirm that it is indeed a Kondo resonance [32]. Unfortunately, our setup has no temperature control, therefore we estimate the Kondo temperature by looking at the full-width at half-maximum (FWHM) of the peak. The width of the peak is related to the Kondo temperature according to:

$$\text{FWHM} = \frac{2}{e} \sqrt{(\pi k_B T)^2 + 2 (k_B T_K)^2}, \quad (4.2)$$

with T the system temperature and e the elementary charge (1.6×10^{-19} C). We fitted a Lorentzian to the conductance traces displaying a Kondo peak following the procedure outlined in Chapter 5 section 5.5.4 to obtain statistics about the width of the peak. From these fits we find an average FWHM of 9.2 meV with a standard deviation of 3.85 meV, which corresponds to a T_K of around 35 K at a system temperature of 6 K. The smallest FWHM we observed was around 5 meV, which corresponds with a T_K of 16 K.

The behavior of a Kondo resonance in a magnetic field can provide information about the ground state. When a Kondo resonance was observed in an IV, the breaking process was stopped, allowing us to record the evolution of a specific molecular configuration in a magnetic field. After such a magnetic field measurement, the breaking process is resumed. Figure 4.5a displays a Kondo resonance exposed to a magnetic field; a two-dimensional map of the same measurements is shown in panel b. As the magnetic field increases, the peak is suppressed and seems to become slightly wider. As a first-principles analysis, we compare this behavior to that of a spin-1/2 Kondo. In that case the peak at zero magnetic field can be described as two Lorentzians centered at zero bias, which in a magnetic field split according to Zeeman splitting. The peak corresponding with the energy level for spin up will move up, while the peak corresponding with spin down will move down in bias voltage. The inset of figure 4.5d shows a schematic of this splitting, where $\Delta E = g m_s \mu_B B$, with g the landé g -factor which we set to 2, m_s the spin quantum number (either $\pm 1/2$), μ_B the Bohr magneton and B the magnetic field. Panel c shows a two-dimensional map of a spin-1/2 Kondo resonance in a magnetic field, where the peak at zero magnetic field was scaled to be identical to the one in panel a. Comparing the two maps, we see that the measured resonance displays a stronger suppression than expected for a spin-1/2 Kondo. To analyze the width of the peak, we fit a Fano lineshape to every curve in panel a:

$$F_{\text{ano}}(V) \propto \frac{(q + \epsilon)^2}{1 + \epsilon^2}, \quad (4.3)$$

where V is the bias voltage, q the asymmetry factor, $\epsilon = (eV - \epsilon_0) / \Gamma_{\text{Fano}}$, with ϵ_0 the energy of the resonance and Γ_{Fano} half the FWHM. The asymmetry factor q leads to a Lorentzian for $q \rightarrow \infty$ and a dip for $q \rightarrow 0$. In the appendix section 4.5.4 a few examples of fits are shown. Figure 4.5d shows a comparison of the FWHM of the peak in panel a and the FWHM of the spin-1/2 Kondo peak. In the appendix section 4.5.5 the same comparison is shown for the height of the peak. In our measurement we observe a stronger splitting and a stronger suppression of

the Kondo resonance that what would be expected for a spin-1/2 system. These observations indicate the presence of a molecule with a spin higher than 1/2.

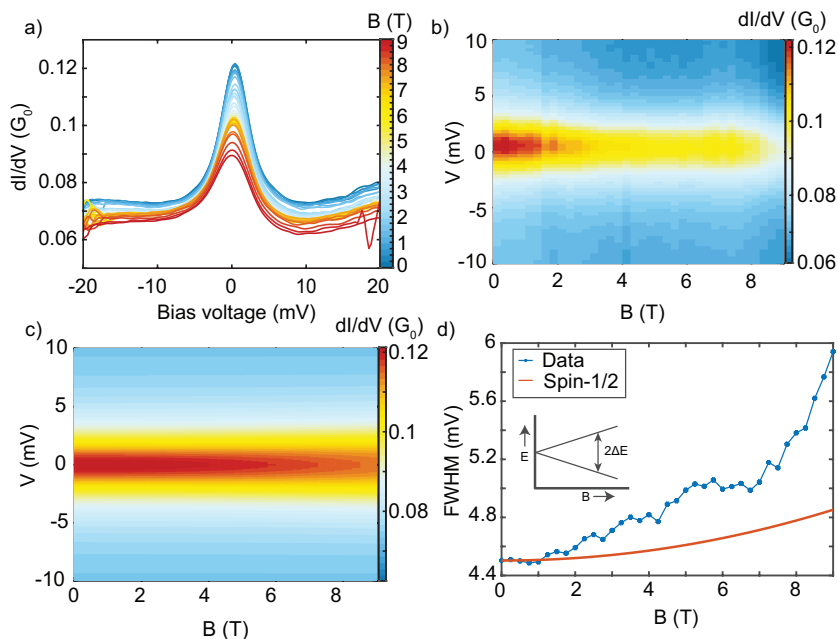


Figure 4.5: a) Kondo resonance measured as a function of magnetic field. b) Two-dimensional conductance map of a). c) Two-dimensional conductance map of the expected splitting of a peak similar in size as in a) for a spin-1/2 system. d) The width of the peak, defined as the difference in conductance between 0 and 10 mV, set out against the magnetic field strength. The blue dots show the peak heights as extracted from a); the solid red line shows the expected width for a spin-1/2 system. The inset displays how the energy levels of a spin-1/2 system split according to the Zeeman effect.

In an STM study, Bairagi *et al.* distinguished the two spin states of a Fe(II) SCO complex through a difference in their IETS spectra. In an IV characteristic, upon reaching a certain bias voltage, a new conduction channel opens up which manifests as an increased slope. In the conductance this inelastic tunneling spectroscopy feature is observed as a step. The origin of this new conduction channel can be either vibrational if the electron-phonon coupling of the system is strong enough, or a spin-flip excitation [33]. Figure 4.6 shows three examples of IETS curves we observed. As mentioned earlier, around 150 IVs displayed such a lineshape. In both panel a and b, the width of the valley is 30 mV, whereas the curve in panel c looks more like a dip, with a width of 10 mV. This width characterizes the energy of the vibrational mode or the spin excitation. The different widths or the presence and absence of a Kondo peak could be indicative of the spin state of the molecule, but theoretical calculations are needed to provide insight into the relevant vibrational energies for each spin state, as well as energies of the possible spin excitations.

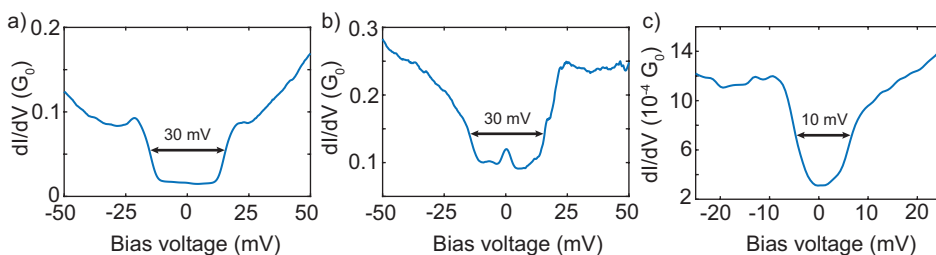


Figure 4.6: Three traces displaying an inelastic tunneling process. a) An IV with steps occurring at ± 15 mV. b) An IV with a Kondo resonance and steps occurring at ± 15 mV. c) An IV with steps occurring at ± 5 mV.

As mentioned in the introduction, studies have reported the observation of memristive behavior for Fe SCO complexes [7, 16]. To investigate whether our Mn(III) SCO complex displays memristive behavior and whether the spin switch can be induced by an electric field, high-voltage IV characteristics were recorded. In these measurements, we look for jumps in the IV, as well as changes in IETS and Kondo in the differential conductance, as this could reflect the change in spin state. As shown in figure 4.7a, memristive behavior was observed; the conductance state depends on the history of the applied voltage. Upon reaching around 900 mV a jump occurs to a state with a lower conductance, while at -950 mV the high conductance state is recovered. Such a reversible cycle is observed in around 10% of the high-voltage IVs, whereas just a switch to another conductance state is present in around 80% of all IVs.

Panel c shows the differential conductance of the IV in panel a. We see that the initial high conductance state has a narrow region where the conductance is suppressed; this region is larger for the low conductance state. This behavior is similar to that reported in a study on a Fe SCO complex in an electroburned graphene junction by Burzuri *et al.* [9]. They report a SCO-induced reconfiguration of the

orbital energies, which is reflected in the differential conductance as a state with a small gap (SG) and a state with a large gap (LG). A reconfiguration of the orbital energies is likely; several magneto-structural studies on similar bulk Mn(III) SCO complexes show a distortion of the coordination sphere which is stronger for the HS state than for the LS state [34–36]. This distortion has been studied extensively in Fe SCO systems and yields a change of the bond lengths between the metal ion and its ligands. This effect is also present in Mn(III) SCO systems, albeit to a lesser extent: the Mn-N bond lengths change by at most 0.1 Å, while the Mn-O bond lengths are roughly constant. These same magneto-structural studies also show that the nature of the substituents and the anions affect the spin transition and the degree of distortion. Therefore, the observed SG and LG states are likely due to a reconfiguration of the molecular orbitals, but density functional theory (DFT) calculations should be performed to provide a better insight in how the alignment of the molecular orbitals changes.

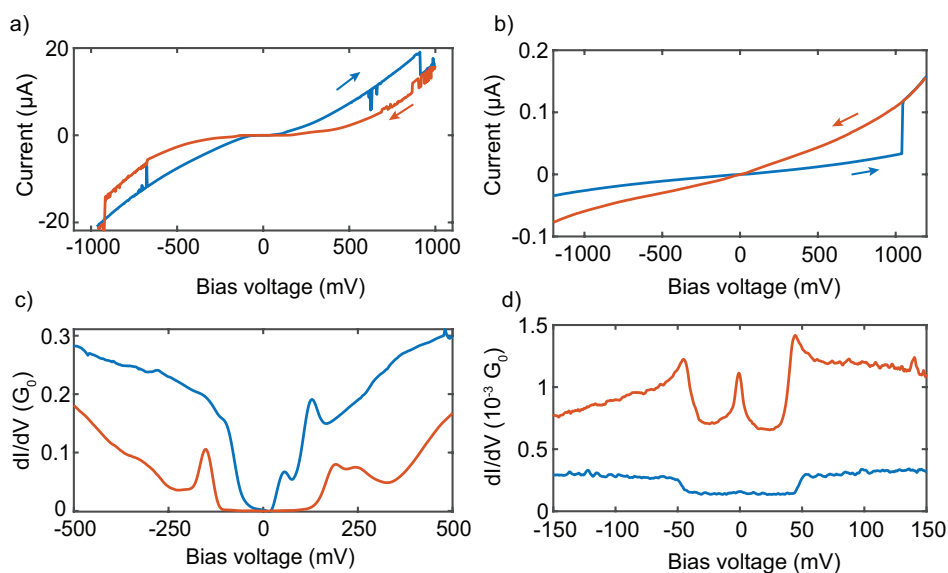


Figure 4.7: a) IV displaying a reversible switch at a bias voltage close to 1 V. The arrows indicate in which direction the bias voltage was swept. The system starts in the high conductance state. b) IV displaying a switch at a bias voltage of 1 V. The arrows indicate in which direction the bias voltage was swept. The system starts in the low conductance state. c) Differential conductance obtained from the IV in a). A low conductance valley is observed around zero-bias voltage, followed by a strong increase in conductance. The width of this valley increased after the system switched to the low conductance state. d) Differential conductance obtained from the IV in b). The low conductance state displays a conductance valley around zero bias voltage, followed by steps at ± 50 mV. The high conductance state shows more pronounced steps at the same bias voltage and a clear Kondo resonance.

In figure 4.7b another IV displaying a switch is shown; panel d displays the corresponding differential conductance. In this case, the system is initially in a low conductance state and switches to a higher conductance state at high bias. In the initial low conductance state, the differential conductance displays an IETS signature, with steps occurring at ± 50 mV. The high-conductance state displays steps at the same bias voltage, but larger in amplitude, as well as a Kondo resonance. Important to note is that this is the only high-voltage IV displaying this behavior out of almost 2000 IVs. Nevertheless, such a change in the conductance lineshape might be evidence of a spin switch. A possible scenario is that the low conductance state is only weakly coupled to the electrodes, therefore having a Kondo temperature which is too low for a resonance to be present. The high conductance state is more strongly coupled, resulting in a higher conductance, a larger IETS signal, as well as a T_K higher than 6 K which results in a Kondo resonance. Finally, the fact that both low- and high-conductance states are found as the starting point has been reported in other studies [16, 18]. Apparently, when SCO molecules are in close contact to surfaces, strain may lead to spin-switching even at low temperatures where only the LS state should be present.

During the high-voltage IV measurements, six consecutive IVs with memristor characteristics were found to display identical behavior, while the gap was opened by 15 pm between each IV. These consecutive IVs and their differential conductance traces are shown in figure 4.8. The conductance around zero bias is the same for the trace (-1 V to +1 V) and retrace (+1 V to -1 V), but we distinguish an SG and an LG state; the trace is the SG state with peaks occurring at around 100 mV; the retrace is the LG state with peaks occurring at around 270 mV. The peak on the right side is much larger for the LG state, while the peak on the left is about the same height for both the SG and LG states. Interestingly, this behavior remains as the electrode separation is increased. This suggests a configuration of the molecule inside the junction which remains stable upon stretching. As discussed in the appendix section 4.5.3, a mechanically-induced reorganization of the molecular orbitals can occur as the electrodes are separated.

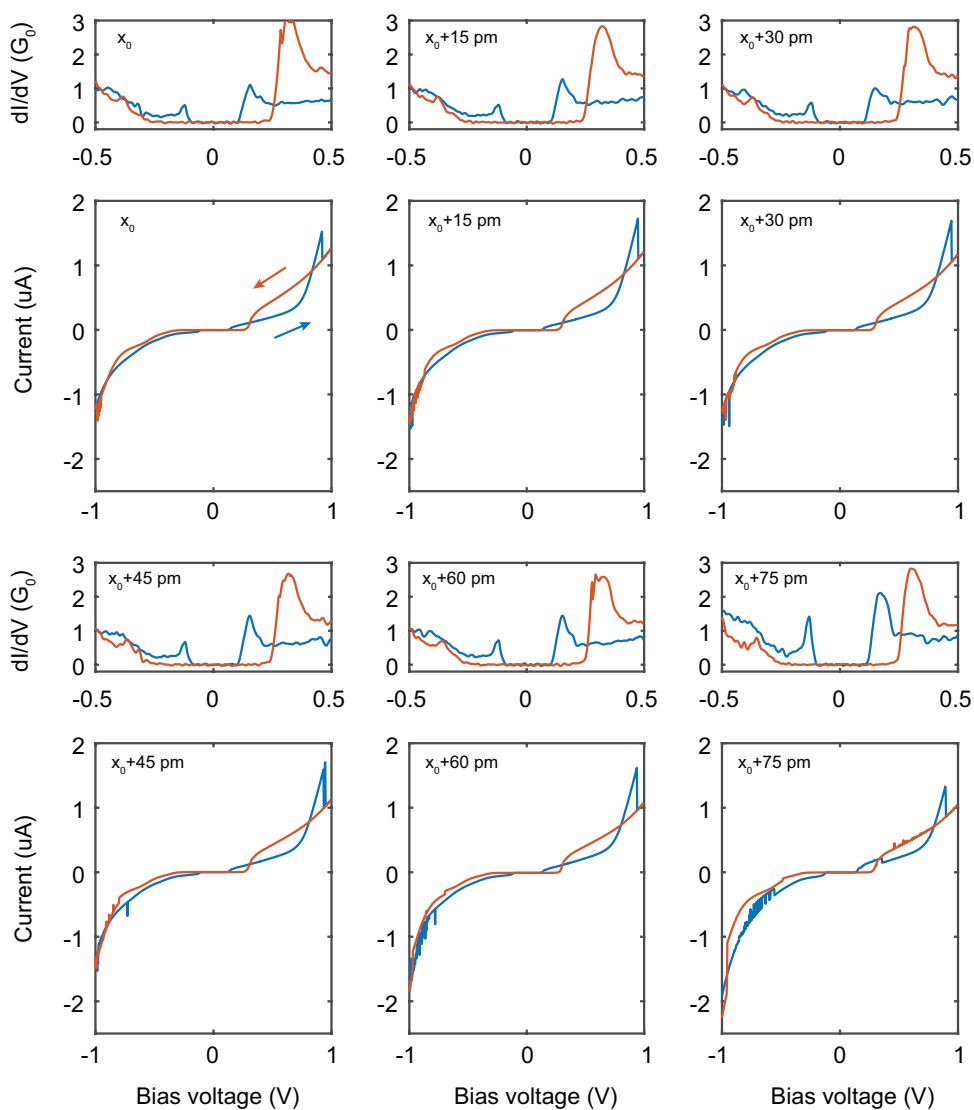


Figure 4.8: Differential conductance and current-voltage characteristics of six consecutive measurements within a breaking trace. Between each characteristic the electrode gap was opened by approximately 15 pm. Blue shows the trace, where the voltage is swept from -1 V to +1 V and orange shows the retrace, where the voltage is swept from +1 V to -1 V.

4.4. Conclusion and outlook

We have performed electronic transport measurements on a Manganese(III) SCO complex in an MCBJ setup. The room-temperature fast-breaking measurements showed a molecular plateau at a conductance of $3 \times 10^{-5} G_0$, while this plateau was absent in reference measurements on the ligand. This result shows that the molecule can be trapped and form junctions with a conductance that is within our experimental range. At cryogenic temperature, different behaviors were observed in the IV characteristics. A large peak in the differential conductance traces suggests the presence of a molecular orbital close to the Fermi energy. Increasing the electrode separation results in the shifting of this resonance, suggesting a mechanical gate effect, where distortion of the molecular structure induces a shift of the molecular orbitals. Additionally, a Kondo resonance was present in around 6% of IVs with a FWHM between 5 and 10 mV. In a magnetic field the peak was found to be suppressed, but not split due to its width. Comparing the observed behavior with that expected for a spin-1/2 Kondo resonance we found that the splitting of the peak, as well its suppression is stronger in our measurement. This indicates that we are most likely measuring a system with a spin $S \geq 1$. Moreover, IETS lineshapes were observed in around 7% of IVs. IETS can either be related to a vibrational mode if the electron-phonon coupling is sufficiently strong, or to a spin-flip process. The characteristic energy scales that we observed were 10 and 30 mV. In order to link these energies to either a vibrational mode or a spin-flip process, DFT calculations, as well as spectroscopic studies should be performed.

Finally, high-voltage measurements were performed with the goal of driving the switch in spin state through an electric field. Jumps in the IVs were observed at voltages above 800 mV and in some cases the IVs displayed memristive behavior. In the differential conductance an SG and an LG state can be distinguished, which is possibly linked to a reconfiguration of the molecular orbitals upon a switch of the spin state. Also, a series of six identical, consecutive IVs were observed while increasing the electrode separation in between each IV. This suggests the existence of mechanically stable configurations, where the transport through the molecule is not affected by stretching it.

We have observed phenomena which in previous studies have been linked to a spin-state switch in SCO complexes. Despite these indications of a switch within the Mn(III) SCO complex, we cannot link a specific behavior to either of the spin states. Therefore, theoretical studies are required, i.e., DFT calculations considering different configurations of the molecule inside the junction and the two spin states. These calculations should also look at the vibrational modes and possible spin-flip excitations. Additionally, single-crystal X-ray diffraction measurements are needed to gain insight in how the coordination sphere is distorted for both spin states.

4.5. Appendix

4.5.1. Fast-breaking measurements on bare gold junctions

Prior to depositing the molecular solution on top of the break junction, measurements are performed on the bare gold junctions to check whether they are of sufficient quality. Figure 4.9 shows a two-dimensional histogram for the samples used for the fast-breaking measurements with the Mn(III) SCO complex (panel a), measurements after deposition are presented in figure 4.2. The sample which was used for the ligand is shown in panel b, the measurements after deposition are presented in figure 4.10. In both cases, the conductance drops sharply below $1 G_0$ to a lower conductance level, after which it decays exponentially with increasing electrode displacement. This behavior is characteristic for direct electron tunneling between the two electrodes. The sample in panel a is of high quality, with a clean drop to below $10^{-3} G_0$. The sample in panel b displays a less clean drop in the conductance, which is most likely due to a less well-defined gold bridge. Nevertheless, the sample displays clean tunneling behavior: no plateaus are present in the conductance as a function of electrode displacement.

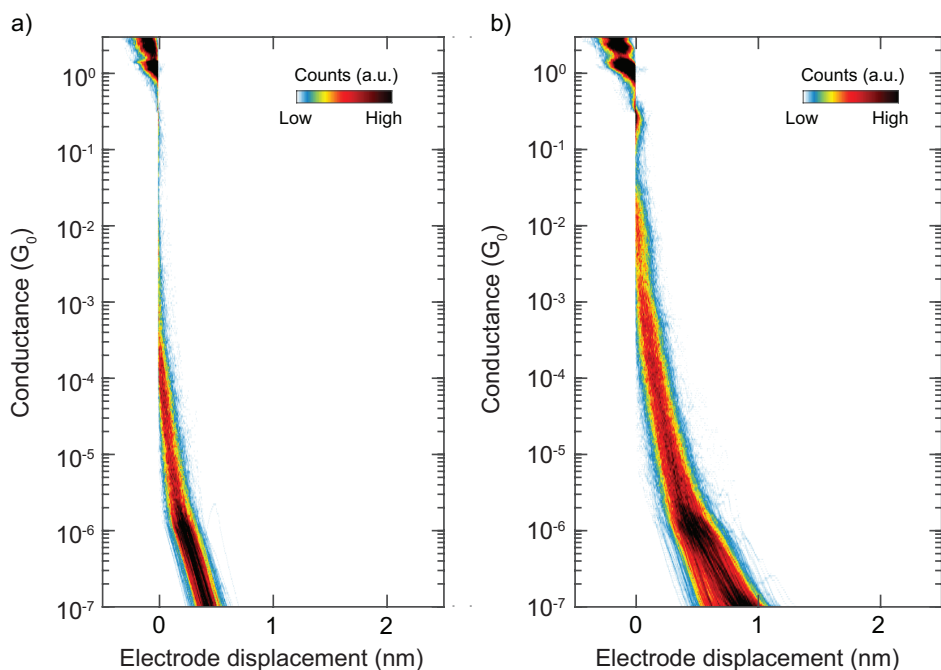


Figure 4.9: Two-dimensional histogram of the fast-breaking measurements on bare gold junctions. a) The characterization of the chip on which the Mn complex was measured. b) The characterization of the chip on which the ligand was measured.

4.5.2. Fast-breaking measurements on the ligand

In order to establish whether the Mn center actually influences the electron transport through the molecule, fast-breaking measurements were also carried out for the ligand. The molecular structure is shown in figure 4.10a. Panel b shows a two-dimensional histogram made from 10.000 consecutive breaking traces, recorded at a bias voltage of 100 mV. It is clear that compared to figure 4.9b, breaking traces are present where the conductance decays more slowly, but still exponentially with increasing electrode displacement. Panel c shows a histogram of the traces which were labeled as tunneling by a neural networks model [20] and panel d shows the traces which were not classified as tunneling. In panel d we do not see a molecular plateau, but rather tunneling behavior with a lower decay factor. The corresponding one-dimensional histogram on the right confirms this: there are no clear peaks visible in the sub- G_0 region. Most likely, multiple stable configurations are possible due to the gold electrodes being able to configure to the nitrogen atoms, as well as the sulphur anchoring groups. These configurations lead to a stabilization of the electrodes, resulting in a slower decay of the conductance compared a bare gold junction.

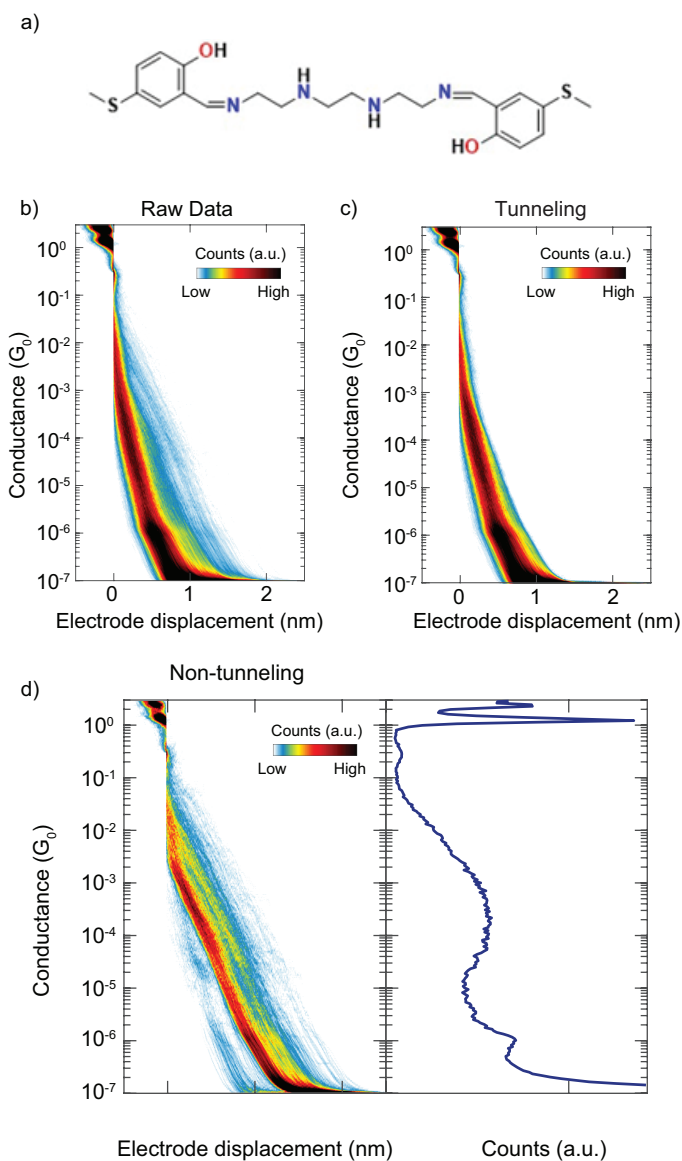


Figure 4.10: a) Molecular structure of the ligand. b) Two-dimensional histogram of the raw data of the fast-breaking measurements. c) Two-dimensional histogram of the traces which were labeled as tunneling by a neural network model [20]. d) Two-dimensional histogram of the traces which were not labeled as tunneling by the model with the corresponding one-dimensional histogram on the right. The peak around $10^{-6} G_0$ is an artifact of the amplifier and not a molecular feature.

4.5.3. Shifting molecular orbitals as a function of electrode displacement and magnetic field

While recording IVs, traces were observed which displayed a large peak in the differential conductance as a function of bias voltage. These peaks were generally larger than an order of magnitude. Vibrational and spin-flip processes usually lead to increases in the conductance of 1-10% of the baseline conductance[37–39], therefore, we attribute these peaks to the presence of a molecular orbital close to the Fermi energy [40]. Upon increasing the electrode separation, these peaks were found to shift to a different bias voltage; these shifts can be as large as 30 mV within a breaking trace (see figure 5.11a). Additionally, sudden changes in the spectrum are observed. A two-dimensional map of the conductance as a function of bias voltage and electrode separation is shown in figure 4.11a. The peak has the highest conductance and corresponds with yellow in the map. Three IVs from different places in this map are shown in panels b,c and d: the map displays a cross with a number corresponding to the IV with the same number. Initially, the differential conductance displays a large peak at -50 mV. As the electrodes are separated, this peak shifts to -40 mV and another peak becomes visible at +100 mV. Finally, a configuration is observed with a peak at -20 mV and one at +50 mV. The shifting of molecular orbitals is probably a result of a mechanical gating effect, where the distortion of the molecular symmetry induces a shift of the energies.

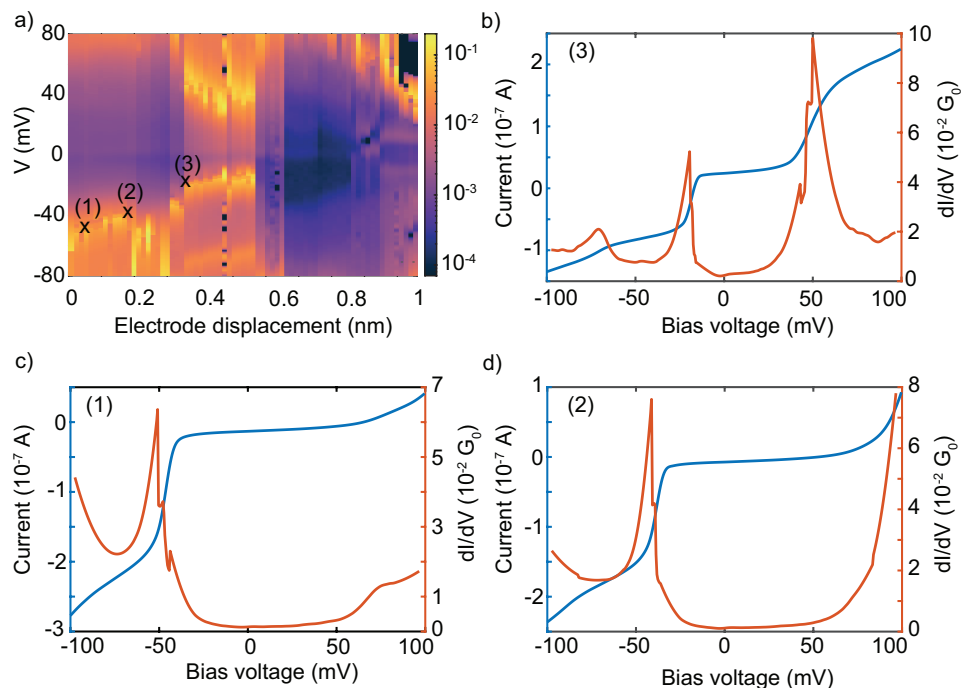


Figure 4.11: a) Two-dimensional map constructed from differential conductance measurements at each motor position within a single breaking trace. b, c, d) IV (blue) and differential conductance (orange) measured at three points indicated in a).

The peaks were found to shift not only with changing electrode separation, but also when applying a magnetic field. An example of such a measurement is shown in figure 4.12. The differential conductance traces in panel a display a zero-bias Kondo peak, as well as an orbital at a bias voltage of 50 mV. Panel b) displays a more detailed view of this peak in the differential conductance. At zero magnetic field, the peak is located at 47 mV. As the magnetic field strength increases, the peak position shifts towards higher bias voltages. At 9 T, the peak is located at 51 mV. Also, the height of the peak seems to decrease as the magnetic field increases, while at the same time the full-width at half-maximum of the peak increases by 1 mV.

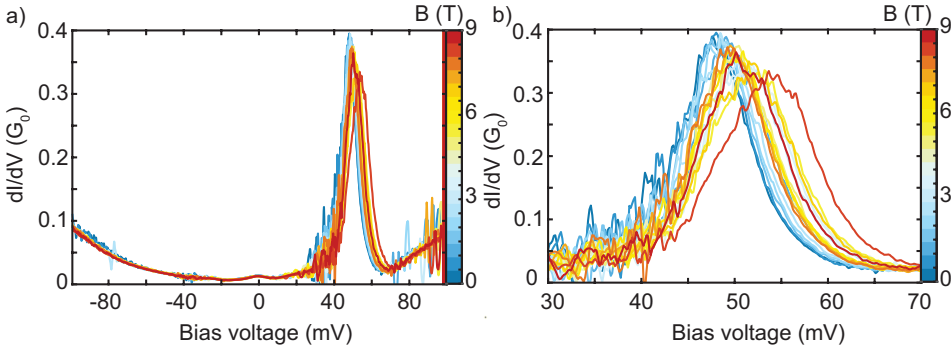


Figure 4.12: a) Differential conductance traces as a function of bias voltage at different magnetic field strengths. b) Zoom-in of the resonance seen in panel a) around a bias voltage of 50 mV.

4.5.4. Examples of Fano fits on a Kondo resonance

In figure 4.5a we show a Kondo resonance in a magnetic field, which we then fit with a Fano lineshape to analyze the width of the peak. The equation used to fit the Fano lineshape is the following:

$$F_{\text{ano}}(V) = d \left(\frac{q + \left(\frac{V - \epsilon_0}{\Gamma_{\text{fano}}} \right)^2}{1 + \left(\frac{V - \epsilon_0}{\Gamma_{\text{fano}}} \right)^2} \right) + e,$$

with d a scaling factor for the height of the peak, q the asymmetry factor, ϵ_0 the energy of the resonance, Γ_{fano} the half-width-half-maximum, V the bias voltage and e the background conductance. In figure 4.13 we present a few examples of the fits, together with the values of the fit parameters. Panels a, b, c and d are the Kondo resonances at respectively 0, 3, 6 and 9 T. The values of the fit parameters are shown in the panels.

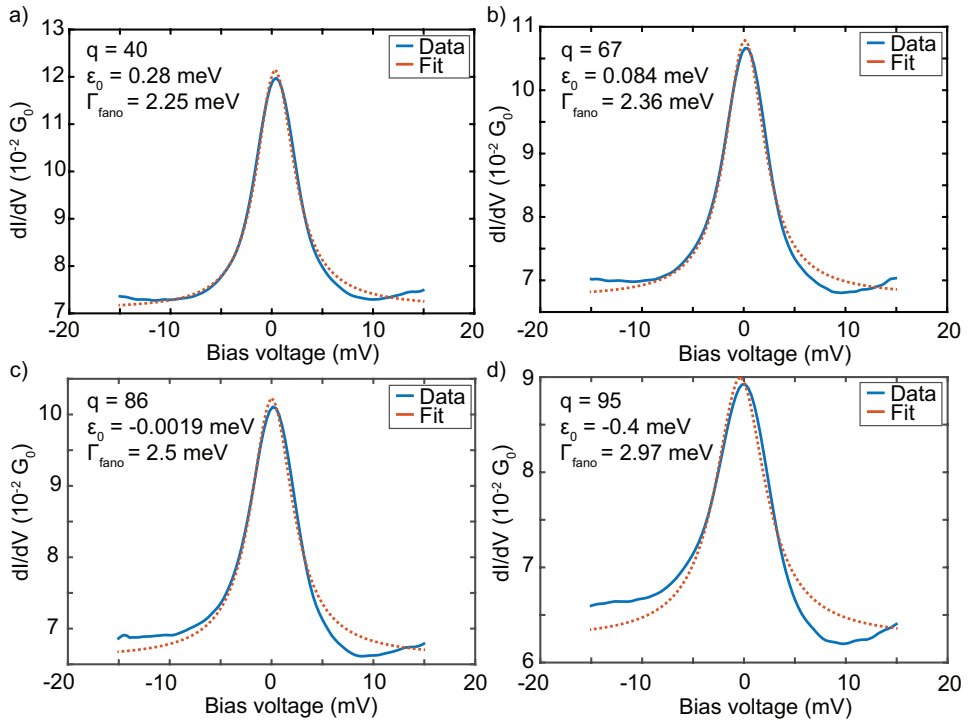


Figure 4.13: Fano lineshape fits of the magnetic field measurements in figure 4.5a. Panel a is at 0 T, panel b at 3 T, panel c at 6 T and panel d at 9 T. Blue drawn lines show the measured data while the dashed orange lines represent the fits.

4.5.5. Height of the Kondo peak in a magnetic field

In figure 4.5 we discuss the evolution of the zero-bias resonance in a magnetic field and compare the FWHM of the measurement to what is expected for a spin-1/2 Kondo peak. The splitting of the peak is found to be stronger than would be expected for a spin-1/2 system. In the same manner, the height of the resonance is compared to that which would be expected for a spin-1/2 Kondo peak. For the comparison, the peak at zero-bias is assumed to consist of the sum of two Lorentzians; these Lorentzians represent the two spin states up and down and their maxima will thus shift apart in a magnetic field. We scale the Lorentzians such that their sum is identical to the peak at 0 T. For each magnetic field strength, the Lorentzians are shifted according to Zeeman splitting and summed to obtain the peak at that magnetic field. This resulting peak is then fitted with a Fano lineshape to stay consistent with the analysis presented in figure 4.5. The height of the peak in the model is defined as the difference between the baseline of the fitted peak, which is the conductance value at ± 10 mV, and the conductance at 0 mV of the fitted peak. The comparison between the model and the data is shown in figure 4.14.

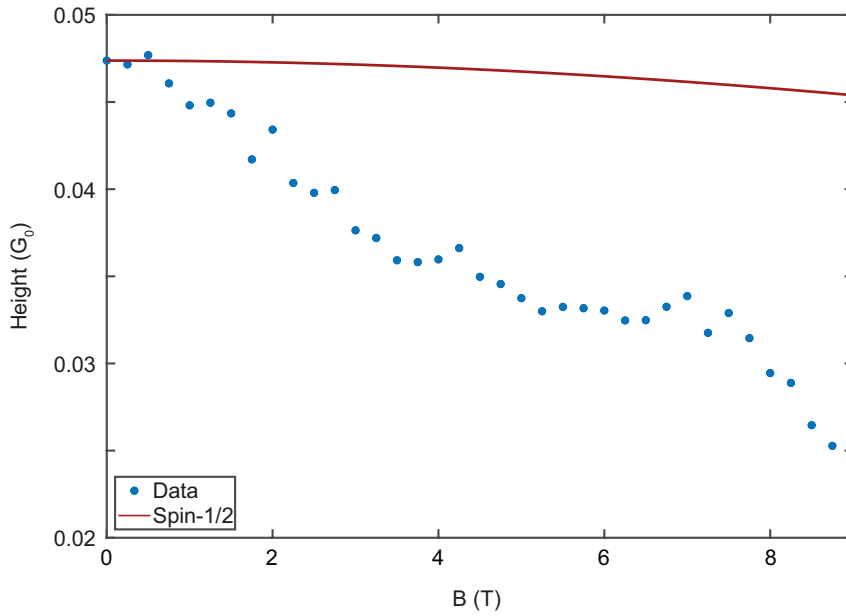


Figure 4.14: The height of the peak, defined as the difference in conductance between 0 and 10 mV, set out against magnetic field (blue dots represent the measured data). The solid, orange line shows the expected height for a spin-1/2 system (see text) for a zero-bias resonance with the same height at $B = 0$ T.

References

- [1] M. Elbing, R. Ochs, M. Koentopp, M. Fischer, C. von Hänisch, F. Weigend, F. Evers, H. B. Weber, and M. Mayor, *A single-molecule diode*, *Proceedings of the National Academy of Sciences* **102**, 8815 (2005).
- [2] I. Díez-Pérez, J. Hihath, Y. Lee, L. Yu, L. Adamska, M. A. Kozhushner, I. I. Oleynik, and N. Tao, *Rectification and stability of a single molecular diode with controlled orientation*, *Nature Chemistry* **1**, 635 (2009).
- [3] E. S. Tam, J. J. Parks, W. W. Shum, Y.-W. Zhong, M. B. Santiago-Berrios, X. Zheng, W. Yang, G. K.-L. Chan, H. D. Abruña, and D. C. Ralph, *Single-Molecule Conductance of Pyridine-Terminated Dithienylethene Switch Molecules*, *ACS Nano* **5**, 5115 (2011).
- [4] N. Darwish, A. C. Aragonès, T. Darwish, S. Ciampi, and I. Díez-Pérez, *Multi-Responsive Photo- and Chemo-Electrical Single-Molecule Switches*, *Nano Letters* **14**, 7064 (2014).
- [5] M. Tsutsui, S. Rahong, Y. Iizumi, T. Okazaki, M. Taniguchi, and T. Kawai, *Single-molecule sensing electrode embedded in-plane nanopore*, *Scientific Reports* **1**, 46 (2011).
- [6] G. Czap, P. J. Wagner, F. Xue, L. Gu, J. Li, J. Yao, R. Wu, and W. Ho, *Probing and imaging spin interactions with a magnetic single-molecule sensor*, *Science* **364**, 670 (2019).
- [7] G. D. Harzmann, R. Frisenda, H. S. J. van der Zant, and M. Mayor, *Single-Molecule Spin Switch Based on Voltage-Triggered Distortion of the Coordination Sphere*, *Angewandte Chemie International Edition* **54**, 13425 (2015).
- [8] R. Frisenda, G. D. Harzmann, J. A. Celis Gil, J. M. Thijssen, M. Mayor, and H. S. J. van der Zant, *Stretching-Induced Conductance Increase in a Spin-Crossover Molecule*, *Nano Letters* **16**, 4733 (2016).
- [9] E. Burzurí, A. García-Fuente, V. García-Suárez, K. Senthil Kumar, M. Ruben, J. Ferrer, and H. S. J. van der Zant, *Spin-state dependent conductance switching in single molecule-graphene junctions*, *Nanoscale* **10**, 7905 (2018).
- [10] B. Xu and N. J. Tao, *Measurement of Single-Molecule Resistance by Repeated Formation of Molecular Junctions*, *Science* **301**, 1221 (2003).
- [11] M. S. Hybertsen and L. Venkataraman, *Structure–Property Relationships in Atomic-Scale Junctions: Histograms and Beyond*, *Accounts of Chemical Research* **49**, 452 (2016).
- [12] J. M. van Ruitenbeek, A. Alvarez, I. Piñeyro, C. Grahmann, P. Joyez, M. H. Devoret, D. Esteve, and C. Urbina, *Adjustable nanofabricated atomic size contacts*, *Review of Scientific Instruments* **67**, 108 (1996).

- [13] L. Wang, L. Wang, L. Zhang, and D. Xiang, *Advance of Mechanically Controllable Break Junction for Molecular Electronics*, *Topics in Current Chemistry* **375**, 61 (2017).
- [14] H. Park, A. K. L. Lim, A. P. Alivisatos, J. Park, and P. L. McEuen, *Fabrication of metallic electrodes with nanometer separation by electromigration*, *Applied Physics Letters* **75**, 301 (1999).
- [15] F. Prins, A. Barreiro, J. W. Ruitenberg, J. S. Seldenthuis, N. Aliaga-Alcalde, L. M. K. Vandersypen, and H. S. J. van der Zant, *Room-Temperature Gating of Molecular Junctions Using Few-Layer Graphene Nanogap Electrodes*, *Nano Letters* **11**, 4607 (2011).
- [16] T. Miyamachi, M. Gruber, V. Davesne, M. Bowen, S. Boukari, L. Joly, F. Scheurer, G. Rogez, T. K. Yamada, P. Ohresser, E. Beaurepaire, and W. Wulfhekel, *Robust spin crossover and memristance across a single molecule*, *Nature Communications* **3**, 938 (2012).
- [17] P. Gütllich, Y. Garcia, and H. A. Goodwin, *Spin crossover phenomena in Fe(ii) complexes*, *Chemical Society Reviews* **29**, 419 (2000).
- [18] K. Bairagi, O. Iasco, A. Bellec, A. Kartsev, D. Li, J. Lagoute, C. Chacon, Y. Girard, S. Rousset, F. Miserque, Y. J. Dappe, A. Smogunov, C. Barreateau, M.-L. Boillot, T. Mallah, and V. Repain, *Molecular-scale dynamics of light-induced spin cross-over in a two-dimensional layer*, *Nature Communications* **7**, 12212 (2016).
- [19] W. Hong, D. Z. Manrique, P. Moreno-García, M. Gulcur, A. Mishchenko, C. J. Lambert, M. R. Bryce, and T. Wandlowski, *Single Molecular Conductance of Tolanes: Experimental and Theoretical Study on the Junction Evolution Dependent on the Anchoring Group*, *Journal of the American Chemical Society* **134**, 2292 (2012).
- [20] F. van Veen, L. Ornago, H. S. van der Zant, and M. El Abbassi, *A generalized neural network approach for separation of molecular breaking traces*, *Journal of Materials Chemistry C* **11**, 15564 (2023).
- [21] V. Fatemi, M. Kamenetska, J. B. Neaton, and L. Venkataraman, *Environmental Control of Single-Molecule Junction Transport*, *Nano Letters* **11**, 1988 (2011).
- [22] W. Liang, M. P. Shores, M. Bockrath, J. R. Long, and H. Park, *Kondo resonance in a single-molecule transistor*, *Nature* **417**, 725 (2002).
- [23] J. Park, A. N. Pasupathy, J. I. Goldsmith, C. Chang, Y. Yaish, J. R. Petta, M. Rinkoski, J. P. Sethna, H. D. Abruña, P. L. McEuen, and D. C. Ralph, *Coulomb blockade and the Kondo effect in single-atom transistors*, *Nature* **417**, 722 (2002).

- [24] L. H. Yu, Z. K. Keane, J. W. Ciszek, L. Cheng, M. P. Stewart, J. M. Tour, and D. Natelson, *Inelastic Electron Tunneling via Molecular Vibrations in Single-Molecule Transistors*, *Physical Review Letters* **93**, 266802 (2004).
- [25] A. Zhao, Q. Li, L. Chen, H. Xiang, W. Wang, S. Pan, B. Wang, X. Xiao, J. Yang, J. G. Hou, and Q. Zhu, *Controlling the Kondo Effect of an Adsorbed Magnetic Ion Through Its Chemical Bonding*, *Science* **309**, 1542 (2005).
- [26] X. Chen, Y.-S. Fu, S.-H. Ji, T. Zhang, P. Cheng, X.-C. Ma, X.-L. Zou, W.-H. Duan, J.-F. Jia, and Q.-K. Xue, *Probing Superexchange Interaction in Molecular Magnets by Spin-Flip Spectroscopy and Microscopy*, *Physical Review Letters* **101**, 197208 (2008).
- [27] J. J. Parks, A. R. Champagne, T. A. Costi, W. W. Shum, A. N. Pasupathy, E. Neuscamman, S. Flores-Torres, P. S. Cornaglia, A. A. Aligia, C. A. Balseiro, G. K.-L. Chan, H. D. Abruña, and D. C. Ralph, *Mechanical Control of Spin States in Spin-1 Molecules and the Underscreened Kondo Effect*, *Science* **328**, 1370 (2010).
- [28] T. Knaak, M. Gruber, C. Lindström, M.-L. Bocquet, J. Heck, and R. Berndt, *Ligand-Induced Energy Shift and Localization of Kondo Resonances in Cobalt-Based Complexes on Cu(111)*, *Nano Letters* **17**, 7146 (2017).
- [29] M. Ormaza, P. Abufager, B. Verlhac, N. Bachellier, M.-L. Bocquet, N. Lorente, and L. Limot, *Controlled spin switching in a metallocene molecular junction*, *Nature Communications* **8**, 1974 (2017).
- [30] J. Kondo, *Resistance Minimum in Dilute Magnetic Alloys*, *Progress of Theoretical Physics* **32**, 37 (1964).
- [31] F. D. M. Haldane, *Scaling Theory of the Asymmetric Anderson Model*, *Physical Review Letters* **40**, 416 (1978).
- [32] M. Žonda, O. Stetsovych, R. Korytár, M. Ternes, R. Temirov, A. Raccanelli, F. S. Tautz, P. Jelínek, T. Novotný, and M. Švec, *Resolving Ambiguity of the Kondo Temperature Determination in Mechanically Tunable Single-Molecule Kondo Systems*, *The Journal of Physical Chemistry Letters* **12**, 6320 (2021).
- [33] M. A. Reed, *Inelastic electron tunneling spectroscopy*, *Materials Today* **11**, 46 (2008).
- [34] S. Ghosh, S. Bagchi, M. Das, S. Kamilya, and A. Mondal, *Stepwise spin-state switching in a manganese(III) complex*, *Dalton Transactions* **49**, 14776 (2020).
- [35] S. Ghosh, S. Bagchi, S. Kamilya, and A. Mondal, *Effect of ligand substituents and tuning the spin-state switching in manganese(III) complexes*, *Dalton Transactions* **50**, 4634 (2021).

- [36] A. V. Tiunova, A. V. Kazakova, D. V. Korchagin, G. V. Shilov, L. V. Zorina, S. V. Simonov, K. V. Zakharov, A. N. Vasiliev, and E. B. Yagubskii, *Abrupt Spin-State Switching in Mn(III) Complexes with BPh 4 Anion: Effect of Halide Substituents on Crystal Structure and Magnetic Properties*. *Chemistry – A European Journal* **27**, 17609 (2021).
- [37] B. C. Stipe, M. A. Rezaei, and W. Ho, *Single-Molecule Vibrational Spectroscopy and Microscopy*, *Science* **280**, 1732 (1998).
- [38] N. Lorente and M. Persson, *Theory of Single Molecule Vibrational Spectroscopy and Microscopy*, *Physical Review Letters* **85**, 2997 (2000).
- [39] M. Ternes, *Spin excitations and correlations in scanning tunneling spectroscopy*, *New Journal of Physics* **17**, 063016 (2015).
- [40] J. Repp, G. Meyer, S. M. Stojković, A. Gourdon, and C. Joachim, *Molecules on Insulating Films: Scanning-Tunneling Microscopy Imaging of Individual Molecular Orbitals*, *Physical Review Letters* **94**, 026803 (2005).

5

Mechanically Stable Kondo Resonance in an Organic Radical Molecular Junction

Abstract

Organic radicals are promising candidates for molecular spintronics due to their intrinsic magnetic moment, their low spin-orbit coupling and their weak hyperfine interactions. Using a Mechanically Controlled Break Junction (MCBJ) setup at both room- and low-temperatures (6 K), we analyse the difference in charge transport between two Nitronyl-Nitroxide Radicals (**NNR**): one with a backbone in the *para* configuration, the other with a backbone in the *meta* configuration. We find that the **para-NNR** displays a Kondo resonance at 6 K, while the **meta-NNR** does not. Additionally, the observed Kondo peak in the differential conductance has a roughly constant width independent of the conductance, consistent with a scenario where the molecule is coupled asymmetrically to the electrodes.

Parts of this chapter have been published in *The Journal of Physical Chemistry C* **2025**, 129, 6, 3152-3157 [1]

5.1. Introduction

A major objective of the field of molecular spintronics is to use the spin property of magnetic molecules as a platform to implement logic, memory and sensing capabilities in electronics. Particularly, organic magnetic molecules stand out as an excellent candidate for spintronics applications as it offers several advantages over the currently used inorganic materials, including long spin decoherence times, a weak hyperfine interaction and their naturally small size [2–4]. Of special interest are radicals, molecules with an open shell, called the singly-occupied molecular orbital (SOMO). A half-filled orbital contributes one spin: a single radical thus has a total spin of $1/2$, whereas a di-radical can have a total spin of 0 (when the two spins are anti-ferromagnetically coupled), or 1 (when the two spins are ferro-magnetically coupled). Radicals can carry a net charge or they can be neutral. Being able to control the spin-degree of freedom in molecules allows to study spin transport phenomena at the molecular level, and could offer new functionalities as a result of built-in molecular properties. For example, recent studies have found radicals to display promising thermoelectricity properties [5, 6], rectifying behavior [7] and to function as a molecular wire where the conductance increases with length [8, 9].

5

Experiments on molecular junctions with organic radicals display Kondo physics at cryogenic temperatures [10–12]. Observation of a Kondo resonance in a molecular junction confirms the presence, as well as the radical character of the molecule in the junction. So far, research has focused on the observation and manipulation of the Kondo resonance [11, 12] and, more recently, other magnetic effects such as magnetoresistance [13, 14]. The configuration of the backbone of the molecule is known to affect the molecular conductance: a para configuration generally has a higher conductance than a meta configuration due to quantum interference [15, 16]. The effect quantum interference in the molecular orbitals has on spin-related phenomena such as the Kondo effect is unknown. Here, we study two all-organic single radicals in a mechanically controlled break junction (MCBJ) setup at both room and cryogenic temperatures. We find that the configuration of the molecular backbone affects the coupling of the radical to the electrode.

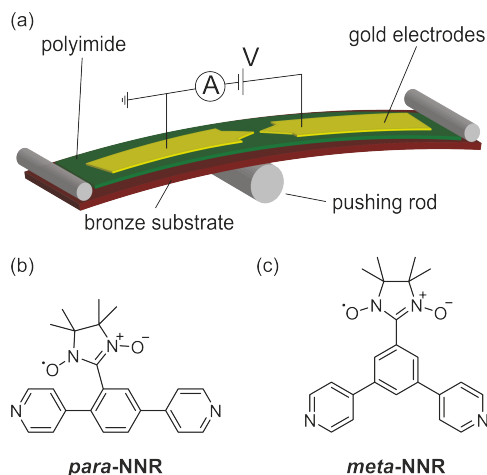


Figure 5.1: a) Schematic of the two-terminal mechanically controlled break junction setup. b) The chemical structure of the *para*-nitronyl-nitroxide radical. c) The chemical structure of the *meta*-nitronyl-nitroxide radical.

5.2. Methods

The conductance of the two molecules was characterized in an MCBJ setup (figure 5.1a), at both room-temperature and ~ 6 K. A gold nanowire is broken by slowly bending the bronze substrate with the pushing rod. Eventually, the wire ruptures and a molecular junction can form. More details on the MCBJ method can be found in prior work [17]. In short, before dropcasting the solution containing the molecule on the break junction, reference measurements were taken on the bare gold junctions (see appendix figure 5.5) to confirm they were clean. Afterwards, the molecule was dissolved in dichloromethane (DCM) to obtain a solution with a molecular concentration of 0.5 mMol for the ***para*-NNR** and 0.2 mMol for the ***meta*-NNR**. Approximately $5 \mu\text{L}$ of this solution was dropcast on the break junction, after which the sample space was closed and pumped to a vacuum below 10^{-4} mbar. Fast-breaking measurements were performed in vacuum at room-temperature, where thousands of conductance vs. electrode spacing (breaking) traces are recorded at a constant bias voltage of 100 mV. To measure at low temperatures, the insert with the sample was submerged in liquid helium, cooling the setup down to a temperature of ~ 6 K. In this case, current-voltage (IV) characteristics were recorded at different electrode displacements in a two-probe configuration: a varying bias voltage is applied across the junction and the resulting current is measured. Afterwards, a Savitzky-Golay filter was applied to the IVs in order to obtain differential conductance vs. bias voltage traces.

5.3. Results and discussion

At room temperature, fast-breaking measurements were performed in vacuum to obtain statistics on junction formation and molecular conductance. A two-dimensional histogram showing conductance versus electrode displacement is constructed from a set of consecutive breaking traces. Figure 5.2 displays the two-dimensional histograms for the **para**-NNR (figure 5.2a) and for the **meta**-NNR (figure 5.2b), together with the one-dimensional histogram of both (figure 5.2c); A log-normal distribution (shaded area) is fitted to the one-dimensional histogram of the **para**-NNR to obtain the most probable molecular conductance.

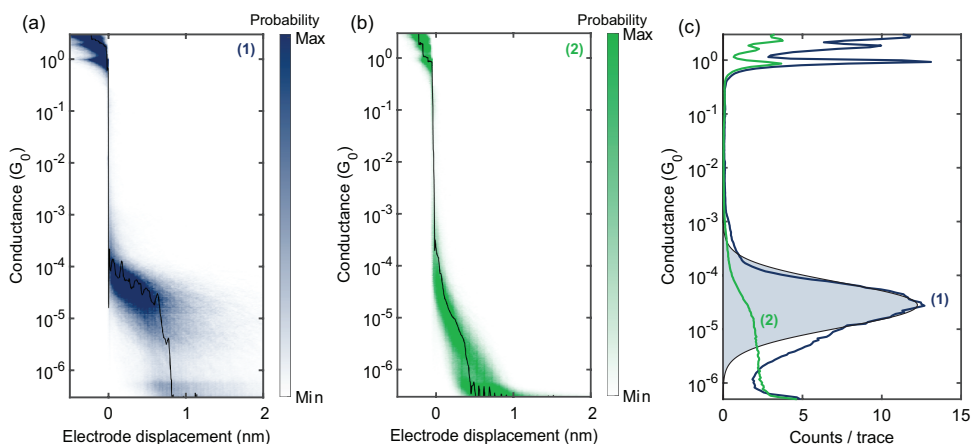


Figure 5.2: a) Two-dimensional histogram of the fast-breaking measurements recorded at room-temperature in a vacuum on **para**-NNR constructed from 7.490 consecutive traces measured at a bias voltage of 100 mV. The black line is a single trace from this set. b) Two-dimensional histogram of the fast-breaking measurements on **meta**-NNR constructed from 10.000 consecutive traces measured at a bias voltage of 100 mV. c) Corresponding one-dimensional histogram of the data in a) and b). A log-normal distribution (the shaded area) is fitted to the histogram of the **para**-NNR to extract the molecular conductance. For **para**-NNR a conductance of $2.8 \cdot 10^{-5} G_0$ is found.

The **para**-NNR displays a clear plateau in the conductance as a function of electrode displacement. The conductance is found to be $2.8 \cdot 10^{-5} G_0$, where $G_0 = 2e^2/h$ is the conductance quantum, e the elementary charge and h Planck's constant. The length of the plateaus is on average ~ 0.7 nm. Considering snapback of the gold contacts, this length corresponds with that of the molecule. [18]. The observation of these clear plateau indicates the formation of molecular junctions. The **meta**-NNR on the other hand, does not display clear plateaus at 100 mV, only at higher bias voltages plateau-like features start to appear (see appendix figure 5.6). This indicates that molecular junctions are formed, however at 100 mV the plateaus are not visible in the accessible measurement range. The lower conductance of the **meta**-NNR is consistent with the presence of quantum interference in the central *meta*-connected benzene ring; due to quantum interference, the *meta* connection of the central benzene ring blocks electron waves from passing through it,

leading to an overall lower conductance compared to the *para* connected benzene ring.[15, 16].

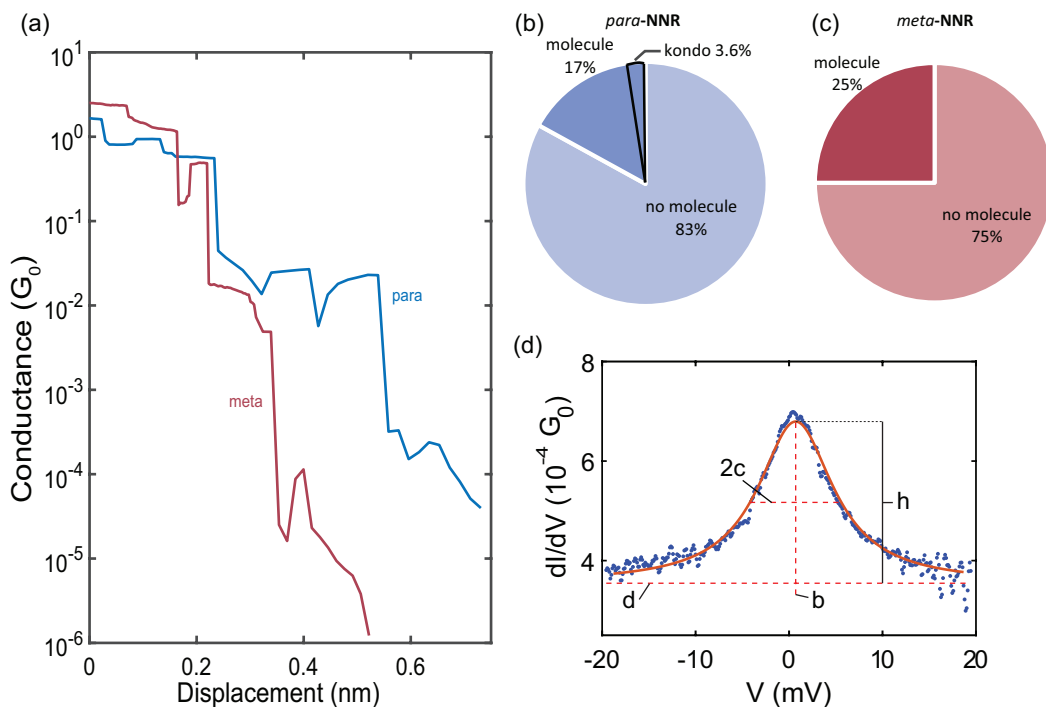


Figure 5.3: a) Example of two breaking traces at low temperatures where a molecular junction has formed. The conductance was recorded at a bias voltage of 50 mV. b,c) Statistics of the breaking measurements at 6 K, showing the percentage of traces which contained a molecular plateau and in the case of the *para*-NNR how many of those displayed a Kondo peak in the differential conductance. d) Example of a Kondo peak measured at 6 K with a Lorentzian fitted to it. The blue dots are the recorded data points and the orange line is the Lorentzian fit. The height h , as well as b , c and d are the fit parameters.

We have also studied the electronic transport of *para*- and *meta*-NNR at a temperature of around 6 K and recorded current-voltage (IV) characteristics while separating the electrodes from each other. For both molecules, plateaus (see figure 5.3a for an example) were observed in the conductance between 10^{-1} and $10^{-6} G_0$, which are attributed to the formation of a molecular junction. There is a large conductance range over which plateaus are observed, possibly due to the high junction stability at cryogenic temperature, which also leads to the observation of plateaus for *meta*-NNR. Furthermore, as shown in figure 5.3a, the conductance of the plateaus can fluctuate more than one order of magnitude within a breaking trace. This is in line with other low temperature MCBJ experiments and is attributed to the existence of more stable molecular configurations, including those where the

electrode distance is smaller than the molecule [12, 14, 19]. In the following analysis, we call a plateau molecular if the breaking trace contains more than three data points below a conductance of $1 G_0$ and above the noise level. Figure 5.3b) and c) show the statistics for the *para*- and *meta*-NNR. For the *para*-NNR, in 17% of the traces, a molecular plateau was observed. For the *meta*-NNR this was in 25% of the traces. Inside these plateaus, IVs were recorded to study charge transport through the molecule.

In the *para*-NNR, a small percentage (3.6%) of IVs showed a zero-bias peak in the differential conductance; an example is displayed in figure 5.3d. Such a peak has been observed before in molecular junctions where the molecule is a radical [10–12, 20–22] and is attributed to the Kondo effect. Interesting to point out is the study by Zhang *et al.*, where an identical molecule except for the anchoring groups is studied. They observed a Kondo resonance in the anti-ferromagnetic weak-coupling regime.[21] While the observed peak is too wide to be split with a magnetic field of 8 T, we did observe a slight suppression of the peak (see appendix figure 5.11), consistent with the expectations for a spin- $\frac{1}{2}$ Kondo. To study the width and height of the peak, we fitted a Lorentzian to the zero-bias peaks (figure 5.3d):

$$f(V) = \frac{a}{\pi b} \left(\frac{c^2}{(V-b)^2 + c^2} \right) + d, \quad (5.1)$$

where a is the scaling factor of the height of the peak, b is the bias voltage at the maximum of the peak, $2c$ is the Full-Width at Half-Maximum (FWHM) and d the baseline of the Lorentzian. To address a small degree of asymmetry in some resonances, they were also fitted using a Fano lineshape. Both lineshapes yielded good fits, but overall the Lorentzian lineshape resulted in a higher R^2 and is therefore used in the following discussion (see Supporting Information section S5 for a comparison between the two lineshapes). The width of the peaks was found to be consistently close to 10 meV, independent of the conductance of the molecular junction. This observation is consistent with other studies, where the constant resonance width is explained by an asymmetric coupling between the molecule and the electrodes.[11, 12, 14] No trend was observed in the height of the peaks (see appendix figure 5.12).

To observe a Kondo peak, the system temperature needs to be below the characteristic Kondo temperature, T_K , which is both related to the width of the zero-bias peak and the widths of the tunneling barriers between the gold electrodes and the molecule. The FWHM of the peak is related to this Kondo temperature:

$$\text{FWHM} = \frac{2}{e} \sqrt{(\pi k_B T)^2 + 2 (k_B T_K)^2}$$
, where T is the sample temperature and k_B the Boltzmann constant [23]. With the average FWHM of 10.3 meV (see figure 5.4a) and a temperature of 6 K, we obtain a Kondo temperature of 40.2 K.

Within the Anderson model, the Haldane relation [24] shows that

$k_B T_K = \sqrt{\frac{U\Gamma}{2}} e^{\pi\epsilon_0(\epsilon_0-U)/U\Gamma}$, where $\Gamma = \Gamma_L + \Gamma_R$, the sum of the electronic coupling to the left and right tunneling barriers ($\Gamma_{L,R}$), U the Coulomb repulsion energy and ϵ_0 the energy level of the orbital through which electron transport occurs. Under the assumption that only a single level contributes to transport and that the coupling Γ is independent of energy (wide-band limit), the conductance of the molecular junction is proportional to: $G \propto \frac{\Gamma_L \Gamma_R}{\Gamma_L + \Gamma_R} \approx \Gamma_L$ if $\Gamma_L \ll \Gamma_R$. A peak width (i.e. a Kondo temperature) that is constant across several orders of magnitude in the conductance thus suggests that the Γ on one side is much larger than the one on the other side, and that only the smaller Γ is sensitive to the separation of both electrodes [12, 14, 25]. The former determines the Kondo temperature whereas the latter determines the conductance of the molecule.

To some extent this strongly asymmetric coupling to both electrodes was expected for **para-NNR**. The nitronyl nitroxide radical group is much stronger interacting with the pyridyl anchor group in *ortho* position than to the other one to which it is in a *meta* relationship. However, the large difference in the mechanical stability of both anchor groups points at an additional stabilization of the *ortho*-pyridyl anchor group. The spatial proximity of the nitronyl-nitroxide radical to the *ortho*-pyridyl suggests that the nitronyl-nitroxide coordinates directly to the electrode. The hypothesized arrangement is sketched in 5.4b) and would explain the finding of a radical group coupling strongly to only one of the two electrodes, which is at the same time considerably less affected mechanically by variations in the electrode spacing. We thus argue that the conductance through the **para-NNR** is dominated on one side by the radical group, whose connection to the electrode is additionally stabilized by the proximity of the anchoring group (figure 5.4b).

Following these arguments, the complete absence of a Kondo peak in **meta-NNR** would indicate that the radical group is not in direct contact to any of the two electrodes (see sketch in figure 5.4c). Apparently, the electronic contact between the electrodes and the radical group is too weak to lead to observable Kondo features at the accessible temperatures. While this can easily be rationalized by the spatial distance between anchor group and radical group, it is noteworthy that the effect is additionally assisted by the poor communication through the *meta*-connections between radical and anchor groups in **meta-NNR**. Both effects lead to a much lower T_K , to a value that is below the 6 K reachable in the experiment.

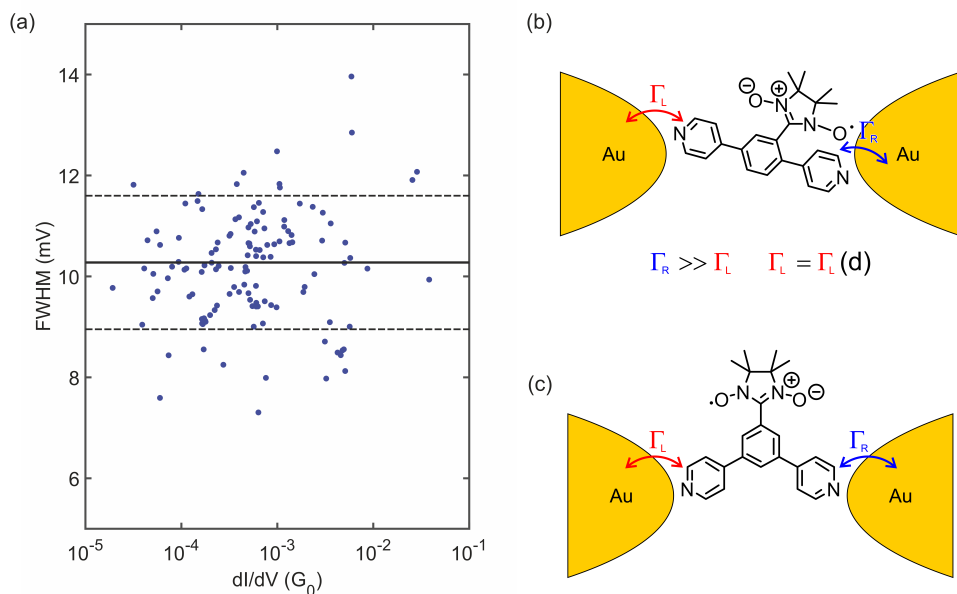


Figure 5.4: a) Full-width at half maximum from the Lorentzians fitted to all Kondo peaks versus the conductance of the baseline of the fit (fit parameter d). Each blue dot represents an IV-measurement. The solid horizontal black line is the average of all values; the dashed black lines are at one standard deviation from the average. Two data points have been left out to improve clarity, one at 16 mV and one at 17 mV but are included in the analysis. b) The proposed configuration of *para*-NRR inside the junction. Γ_L is the weak coupling of the molecule to the left electrode that changes upon separating the electrodes and Γ_R the coupling to the right electrode. c) Proposed configuration of *meta*-NRR inside the junction.

5.4. Conclusions

In conclusion, we have investigated charge transport in a *para*- and in a *meta*-configured NRR in an MCBJ setup through fast-breaking measurements at room temperature and through IVs at 6 K. At room temperature, a clear conductance plateau was observed for the *para*-NRR, while this was not the case for the *meta*-NRR. A Kondo peak was observed in the low-temperature measurements on the *para*-NRR. Analysis of this peak revealed a constant peak width, independent of the conductance of the molecular junction. We hypothesize that this is a result of a very asymmetric coupling of the molecule to the electrodes. The coupling of the radical group to one of the electrodes is stabilized by the proximity of the anchoring group. It would be of interest to perform *ab initio* conductance calculations considering the different configurations of the molecules inside the junction and to elucidate the role of the stabilization by the anchoring group. These results provide a better understanding of the effect the molecular structure has on electron pathways and the presence of magnetic fingerprints in it. Both are important considerations for creating molecular spintronic devices.

5.5. Appendix

5.5.1. Reference measurements on bare gold junctions

Prior to using a sample for molecular measurements, the sample is characterized. In case no contaminations are present on the sample, an exponential decay of the conductance as a function of electrode separation is expected. Figure 5.5 shows these measurements performed on the same junctions as those which were used for the measurements displayed in figure 5.2 of the main text. In both cases the conductance decays exponentially with increasing electrode displacement, indicating a clean junction.

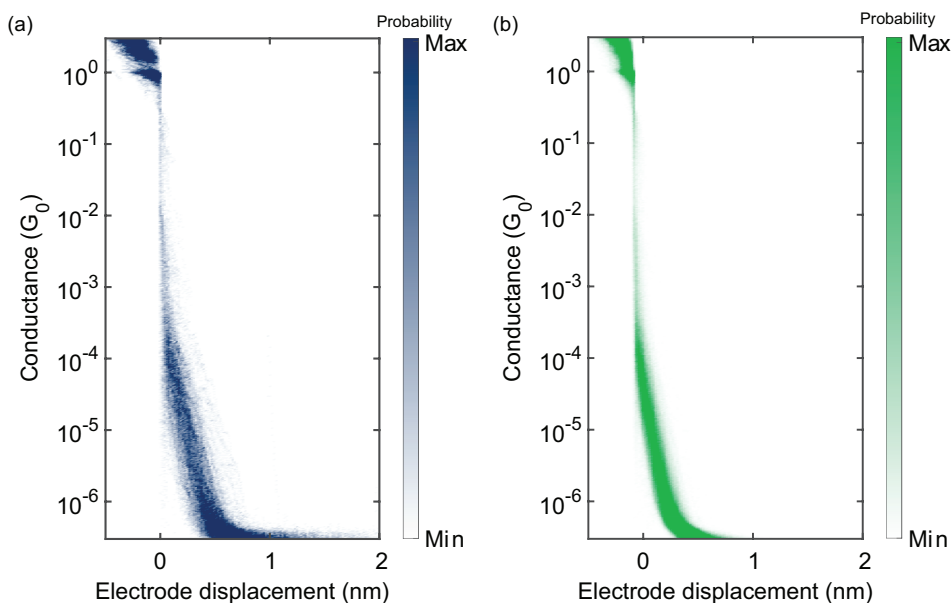


Figure 5.5: a) Two-dimensional histogram of the fast-breaking measurements on a bare gold junction. The same junction was used for the measurements on the para-nitronyl-nitroxide radical in this paper. Traces were recorded at a bias voltage of 100 mV. b) Two-dimensional histogram of the fast-breaking measurements on a bare gold junction which was later used to measure the meta-nitronyl-nitroxide radical.

5.5.2. Two-dimensional histograms of *meta*-NNR at different bias voltages

In our break junction experiments we record sets of consecutive traces at different bias voltages. For the *meta*-NNR, no clear plateaus were observed at a bias voltage of 100 mV (see figure 5.2 in the main text). Figure 5.6 shows two-dimensional histograms of sets of consecutive breaking traces recorded at 100 mV (a), 250 mV (b) and 350 mV (c). At 100 mV, the histogram is barely distinguishable from the bare gold junction (figure 5.5b). At higher bias, a feature forms at a conductance of around $10^{-5} G_0$ as more plateaus are observed.

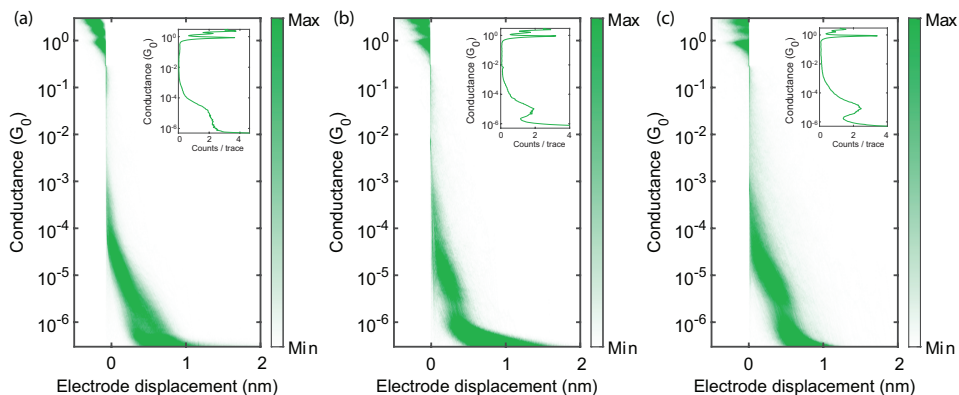


Figure 5.6: a) Two-dimensional histogram of fast-breaking measurements recorded at room-temperature in a vacuum on the meta-nitronyl-nitroxide radical at a bias voltage of 100 mV. b) At 250 mV. c) At 350 mV.

5.5.3. Clustering of the *meta*-NNR fast-breaking measurements

In figure 5.6a, around $10^{-6} G_0$ two clusters seem to be present: one which decays quickly to the noise level and one which decays slower. To better investigate this, we used a neural network model [26], which has been trained with datasets of both bare gold junctions and junctions containing molecules, to separate breaking traces of the fast-breaking measurement recorded at a bias voltage of 100 mV. The result is shown in figure 5.7. The algorithm was set to consider the region between a conductance of 10^{-2} and $10^{-6} G_0$ and between an electrode displacement of 0 and 2.5 nm. The first panel shows the two-dimensional histogram of the traces which are labeled as class 1 and the second panel shows the two-dimensional histogram of the traces which are labeled as class 2. Class 1 has a lower decay factor compared to the one of class 2, most likely due to the presence of molecules on the electrode surface. No conductance plateaus are observed, nor a clear peak in the one-dimensional histogram; hence we cannot assign a most likely molecular conductance to the molecule from this measurement at 100 mV.

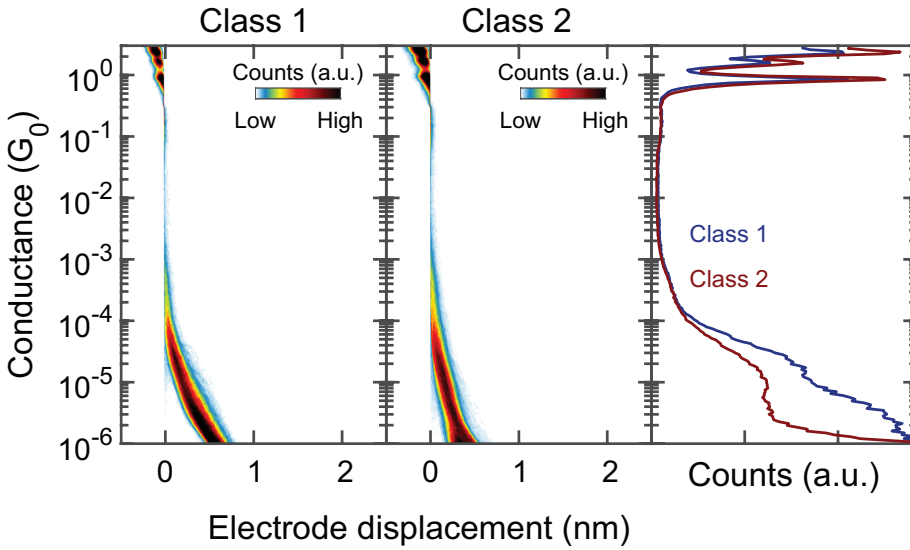


Figure 5.7: Two-dimensional and one-dimensional histograms obtained after clustering the dataset of the fast-breaking measurements on *meta*-NRR recorded at a bias voltage of 100 mV (figure 5.6a).

5.5.4. Fits on Kondo peaks

In total, 129 zero-bias peaks were observed among 3330 IVs. A Lorentzian was fitted to all these peaks in order to determine the width and the height of the peaks. In most cases, the Lorentzian fitted the data accurately. Figure 5.8 shows several more peaks with the corresponding fit.

Because several Kondo resonances displayed a small degree of asymmetry, we also fitted the peaks using a Fano lineshape [27, 28]:

$$F_{\text{ano}}(V) \propto \frac{(q + \epsilon)^2}{1 + \epsilon^2}, \quad (5.2)$$

with q the asymmetry factor and $\epsilon = (eV - E_k)/\Gamma_{\text{Fano}}$ where e is the elementary charge $1.6 \cdot 10^{-19}$, V the bias voltage, E_k the energy of the resonance and Γ_{Fano} the half-width at half-maximum of the resonance. Fits of the same resonances as in figure 5.8 are shown in figure 5.9. In most cases, good fits could be made, however, as seen in panel d this was not always the case. From the fitting of a Fano lineshape to the 129 Kondo resonances we found an average q factor of 16.6 with a standard deviation of 4.26. For a comparison between the fits with a Lorentzian lineshape and a Fano lineshape, the R^2 values for both are shown in figure 5.10. It is clear that a Lorentzian lineshape yields better fits.

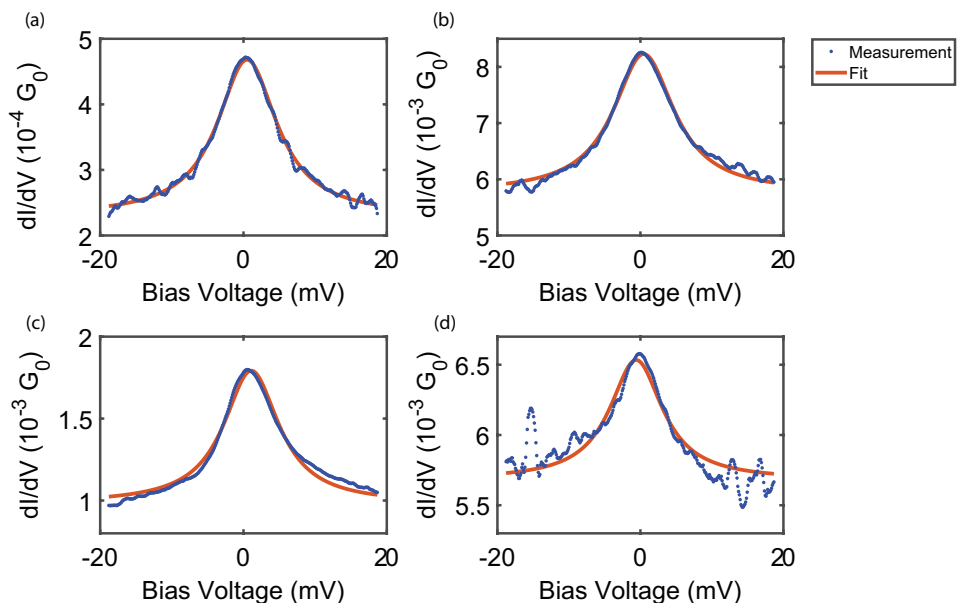


Figure 5.8: a-d) Four examples of observed zero-bias peaks in the differential conductance as a function of bias voltage (blue). Each of these peaks was fitted with a Lorentzian (orange).

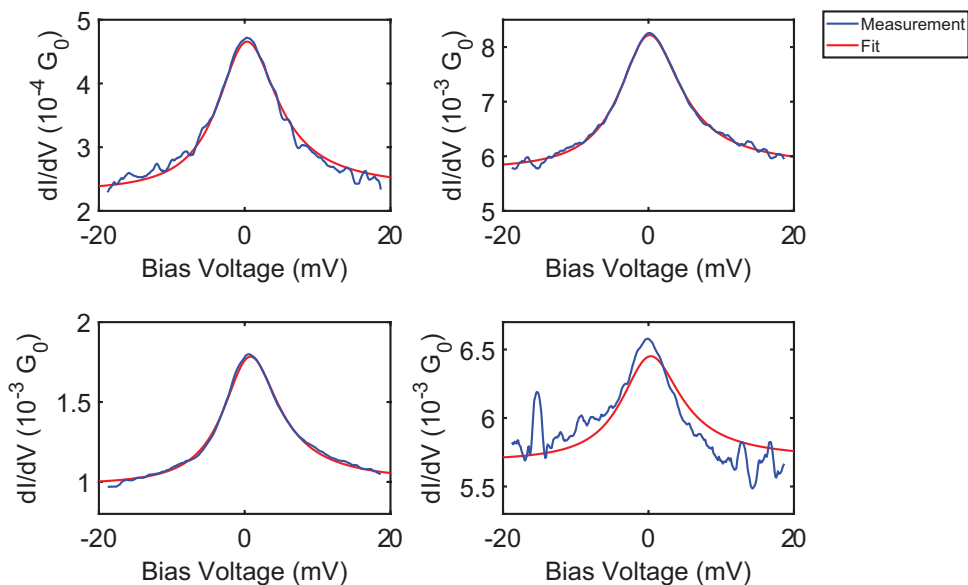


Figure 5.9: a-d) Four examples of observed zero-bias peaks in the differential conductance as a function of bias voltage (blue). Each of these peaks was fitted with a Fano lineshape (orange).

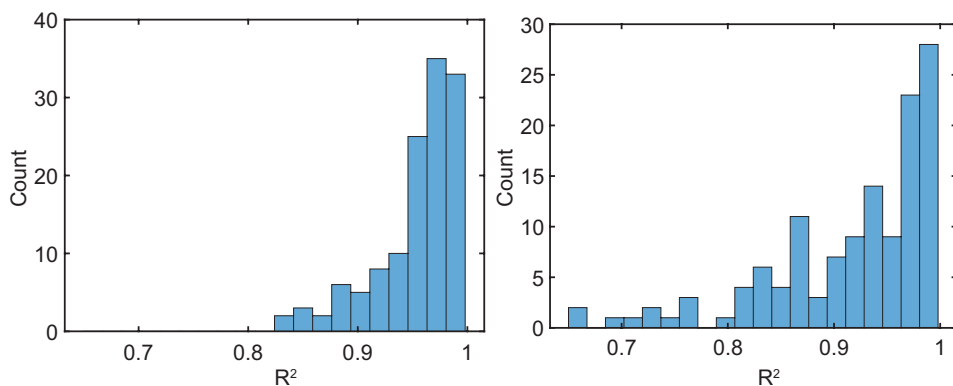


Figure 5.10: a) Histogram of the squared residuals for the fit using a Lorentzian lineshape. b) Histogram of the squared residuals for the fit using a Fano lineshape.

5.5.5. Magnetic field measurements on *para*-NNR

One key characteristic of a Kondo resonance, is that it will split under a magnetic field due to the lifting of the spin-degeneracy. Depending on the width of the peak (and thus the Kondo temperature), this is observed as either a suppression of the peak, or a full splitting. In the case of the *para*-NNR, the peak width is usually around 10 meV, which is too broad to split. In one magnetic field measurement (out of 5) however, a suppression of the peak at high magnetic fields was observed (see figure 5.11). In order to qualitatively view the behavior of the peak, the traces were all normalized with respect to the baseline (parameter d) of the fitted Lorentzian.

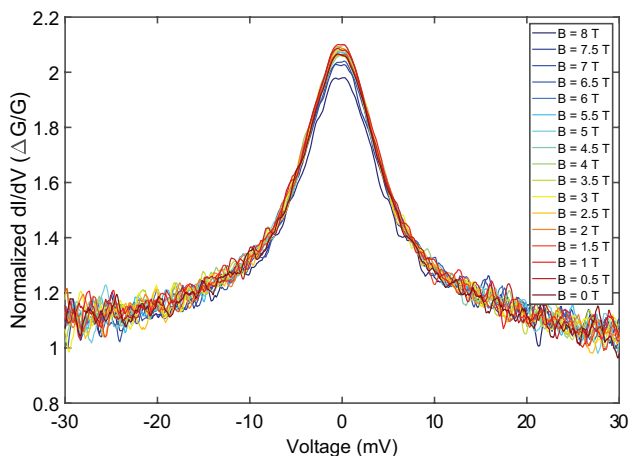


Figure 5.11: Plot of the normalized differential conductance as a function of bias voltage at magnetic fields ranging from 0 T to 8 T measured on the *para*-nitronyl-nitroxide radical. The conductance was normalized with respect to the baseline (parameter d) of the fitted Lorentzian.

5.5.6. Height of the Kondo resonances

The height of the peaks was analyzed in the same way as the width. The height of a peak was defined as the difference between the highest point of the peak and the baseline of the fitted Lorentzian. In order to compare traces which were recorded at different order of magnitude of conductance, the height was normalized with respect to the baseline of the fitted Lorentzian. This resulted in figure 5.12. No trend is observed: there is no correlation between the height of the peak and the conductance at which it was recorded, nor is it constant across different orders of magnitude of conductance. The large variation in normalized height is probably due to the changing coupling strength of the backbone of the molecule during breaking. The lack of correlation suggests that many different configurations are possible, between which the coupling of the backbone to the electrodes and the radical group to the electrodes do not depend on each other.

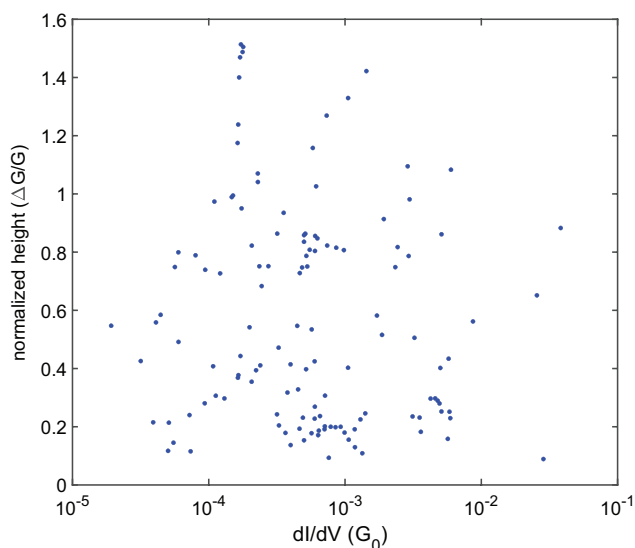


Figure 5.12: The normalized height of the Lorentzians fitted to differential conductance measurements taken on the para-nitronyl-nitroxide radical versus their baseline conductance (parameter d). The normalized height is defined as the difference between the conductance at zero-bias and the baseline conductance (parameter d), divided by the baseline conductance.

References

- [1] T. Bras, C. Hsu, T. Y. Baum, D. Vogel, M. Mayor, and H. S. J. van der Zant, *Mechanically Stable Kondo Resonance in an Organic Radical Molecular Junction*, *The Journal of Physical Chemistry C* **129**, 3152 (2025).
- [2] S. Sanvito, *Molecular spintronics*, *Chemical Society Reviews* **40**, 3336 (2011).
- [3] A. R. Rocha, V. M. García-suárez, S. W. Bailey, C. J. Lambert, J. Ferrer, and S. Sanvito, *Towards molecular spintronics*, *Nature Materials* **4**, 335 (2005).
- [4] M. Gobbi, M. A. Novak, and E. Del Barco, *Molecular spintronics*, *Journal of Applied Physics* **125**, 240401 (2019).
- [5] S. Sangtarash and H. Sadeghi, *Radical enhancement of molecular thermoelectric efficiency*, *Nanoscale Advances* **2**, 1031 (2020).
- [6] J. Hurtado-Gallego, S. Sangtarash, R. Davidson, L. Rincón-García, A. Daaoub, G. Rubio-Bollinger, C. J. Lambert, V. S. Oganessian, M. R. Bryce, N. Agrait, and H. Sadeghi, *Thermoelectric Enhancement in Single Organic Radical Molecules*, *Nano Letters* **22**, 948 (2022).
- [7] S. Naghibi, S. Sangtarash, V. J. Kumar, J. Wu, M. M. Judd, X. Qiao, E. Gorenskaia, S. J. Higgins, N. Cox, R. J. Nichols, H. Sadeghi, P. J. Low, and A. Vezzoli, *Redox-Addressable Single-Molecule Junctions Incorporating a Persistent Organic Radical***, *Angewandte Chemie* **134** (2022), 10.1002/ange.202116985.
- [8] A. Sil, L. Hamilton, J. M. F. Morris, A. H. S. Daaoub, J. H. H. Burrows, C. M. Robertson, K. Luzyanin, S. J. Higgins, H. Sadeghi, R. J. Nichols, S. Sangtarash, and A. Vezzoli, *Zero-Bias Anti-Ohmic Behaviour in Diradicaloid Molecular Wires*, *Angewandte Chemie International Edition* **63** (2024), 10.1002/anie.202410304.
- [9] L. Li, J. Z. Low, J. Wilhelm, G. Liao, S. Gunasekaran, C. R. Prindle, R. L. Starr, D. Golze, C. Nuckolls, M. L. Steigerwald, F. Evers, L. M. Campos, X. Yin, and L. Venkataraman, *Highly conducting single-molecule topological insulators based on mono- and di-radical cations*, *Nature Chemistry* **14**, 1061 (2022).
- [10] L. H. Yu and D. Natelson, *The Kondo Effect in C 60 Single-Molecule Transistors*, *Nano Letters* **4**, 79 (2004).
- [11] J. J. Parks, A. R. Champagne, G. R. Hutchison, S. Flores-Torres, H. D. Abruña, and D. C. Ralph, *Tuning the Kondo Effect with a Mechanically Controllable Break Junction*, *Physical Review Letters* **99**, 026601 (2007).
- [12] R. Frisenda, R. Gaudenzi, C. Franco, M. Mas-Torrent, C. Rovira, J. Veciana, I. Alcon, S. T. Bromley, E. Burzurí, and H. S. J. van der Zant, *Kondo Effect in a Neutral and Stable All Organic Radical Single Molecule Break Junction*, *Nano Letters* **15**, 3109 (2015).

- [13] R. Hayakawa, M. A. Karimi, J. Wolf, T. Huhn, M. S. Zöllner, C. Herrmann, and E. Scheer, *Large Magnetoresistance in Single-Radical Molecular Junctions*, *Nano Letters* **16**, 4960 (2016).
- [14] G. Mitra, J. Z. Low, S. Wei, K. R. Francisco, M. Deffner, C. Herrmann, L. M. Campos, and E. Scheer, *Interplay between Magnetoresistance and Kondo Resonance in Radical Single-Molecule Junctions*, *Nano Letters* **22**, 5773 (2022).
- [15] C. R. Arroyo, R. Frisenda, K. Moth-Poulsen, J. S. Seldenthuis, T. Bjørnholm, and H. S. van der Zant, *Quantum interference effects at room temperature in OPV-based single-molecule junctions*, *Nanoscale Research Letters* **8**, 234 (2013).
- [16] G. Yang, H. Wu, J. Wei, J. Zheng, Z. Chen, J. Liu, J. Shi, Y. Yang, and W. Hong, *Quantum interference effect in the charge transport through single-molecule benzene dithiol junction at room temperature: An experimental investigation*, *Chinese Chemical Letters* **29**, 147 (2018).
- [17] C. A. Martin, R. H. M. Smit, R. van Egmond, H. S. J. van der Zant, and J. M. van Ruitenbeek, *A versatile low-temperature setup for the electrical characterization of single-molecule junctions*, *Review of Scientific Instruments* **82**, 053907 (2011).
- [18] W. Hong, D. Z. Manrique, P. Moreno-García, M. Gulcur, A. Mishchenko, C. J. Lambert, M. R. Bryce, and T. Wandlowski, *Single Molecular Conductance of Tolanes: Experimental and Theoretical Study on the Junction Evolution Dependent on the Anchoring Group*, *Journal of the American Chemical Society* **134**, 2292 (2012).
- [19] R. Frisenda, D. Stefani, and H. S. J. van der Zant, *Quantum Transport through a Single Conjugated Rigid Molecule, a Mechanical Break Junction Study*, *Accounts of Chemical Research* **51**, 1359 (2018).
- [20] R. Temirov, A. Lassise, F. B. Anders, and F. S. Tautz, *Kondo effect by controlled cleavage of a single-molecule contact*, *Nanotechnology* **19**, 065401 (2008).
- [21] Y.-h. Zhang, S. Kahle, T. Herden, C. Stroh, M. Mayor, U. Schlickum, M. Ternes, P. Wahl, and K. Kern, *Temperature and magnetic field dependence of a Kondo system in the weak coupling regime*, *Nature Communications* **4**, 2110 (2013).
- [22] T. Y. Baum, S. Fernández, D. Peña, and H. S. J. van der Zant, *Magnetic Fingerprints in an All-Organic Radical Molecular Break Junction*, *Nano Letters* **22**, 8086 (2022).
- [23] K. Nagaoka, T. Jamneala, M. Grobis, and M. F. Crommie, *Temperature Dependence of a Single Kondo Impurity*, *Physical Review Letters* **88**, 077205 (2002).

- [24] F. D. M. Haldane, *Scaling Theory of the Asymmetric Anderson Model*, *Physical Review Letters* **40**, 416 (1978).
- [25] W. H. Appelt, A. Droghetti, L. Chioncel, M. M. Radonjić, E. Muñoz, S. Kirchner, D. Vollhardt, and I. Rungger, *Predicting the conductance of strongly correlated molecules: the Kondo effect in perchlorotriphenylmethyl/Au junctions*, *Nanoscale* **10**, 17738 (2018).
- [26] F. van Veen, L. Ornago, H. S. van der Zant, and M. El Abbassi, *A generalized neural network approach for separation of molecular breaking traces*, *Journal of Materials Chemistry C* **11**, 15564 (2023).
- [27] U. Fano, *Effects of Configuration Interaction on Intensities and Phase Shifts*, *Physical Review* **124**, 1866 (1961).
- [28] M. Gruber, A. Weismann, and R. Berndt, *The Kondo resonance line shape in scanning tunnelling spectroscopy: instrumental aspects*, *Journal of Physics: Condensed Matter* **30**, 424001 (2018).

Acknowledgements

During my years as a PhD student there have been many people who in some way had an impact on my life. Here, I would like to take the opportunity to thank those people. If I happen to forget someone, I apologize.

Allereerst wil ik graag **Herre** bedanken. Als masterstudent begon ik in uw lab, waar ik het meteen naar mijn zin had. Zodanig naar mijn zin dat ik graag ook een PhD in uw groep wilde doen. Hoewel ik niet altijd makkelijk was en best wel pessimistisch kon zijn, probeerde u mij altijd in te laten zien dat het allemaal niet zo erg was als ik dacht. U was altijd beschikbaar voor vragen of een meeting en u was altijd betrokken bij alles wat er gebeurde in het lab. Als het niet goed liep had u ideeën over wat de oorzaak kon zijn en als het wel goed liep was u druk aan het beredeneren wat de beste verklaring voor de metingen was. U pushte mij om meer uit mezelf te halen en een betere onderzoeker te zijn. Bedankt voor de afgelopen jaren, u was een hele fijne begeleider. **Ferdinand**, bedankt voor je rol als promotor en het leuke gesprek over mijn stellingen. **Jaime**, it was great to get to know you better during your visit here and to learn DFT from you. Thank you for being part of my committee. **Abhishek**, I remember our first meeting when you visited Delft where you showed us all the things that you were working on in your lab. It was a pleasure to work on the spin crossover molecules. **Talal**, although our communication was mostly through email, I want to thank you for being available whenever I had questions and for supplying us with the nanoparticles. Thank you for being part of my committee. **Pascal, Laurens and Sander**, thank you for being part of my committee and for assessing my dissertation.

Next, I would like to thank the people with whom I have worked. I would like to start with my paranymphs, Cosimo and Yongqing. **Cosimo**, the last six months I had the pleasure of working on the cable bacteria with you. You are a very kind-hearted and caring person and we share many interests, which made it easy and fun to work together. Thank you for having me and getting me into Ravenswatch, I wish you all the best. **Yongqing**, your dedication to and your interest for your work are inspiring. You are always positive and interested in what others are doing. I am happy I got to show you around in the lab and help you with your measurements. Thank you and good luck.

I also want to thank the many people who have been part of the van der Zant group at the same time as me. **Sebastiaan**, wij begonnen op dezelfde dag met onze projecten en werkten in hetzelfde kantoor. We discussieerden vaak over wat er gaande was in onze projecten en konden altijd even bij elkaar klagen als dingen weer eens niet soepel liepen. De koffiepauzes waren altijd een erg welkome afwisseling. Ik wens je het beste in de toekomst. **Jacqui**, it always brightened my day a little when you were around. What started as trying to solve the fabrication issues in the cleanroom developed into a great friendship. I happily think back to

the 'fancy' coffee breaks and our well-earned dinners at Hummus. **Chunwei**, you supervised me during my master thesis and taught me many of the skills I needed during my Ph.D. It was great to work with you and learn from you and I wish you a great future. **Luca**, you taught me how to work in the cleanroom and your great sense of humor often made for a good laugh. **Thomas**, your crazy and creative ideas made for interesting conversations. Let's go bouldering again sometime soon. **Talieh and Josep**, your passion for research and Physics were very motivating. It was great to work with you and get the measurements going in the attocube. **Damian**, you were always ready to help and interested in how things were going. And yes, I really believe it is a particle. **Serhii**, you were always ready to help me if I had issues in the lab or discuss measurements. **Raul**, you are always joyful and laid-back. Thank you for the sourdough starter and advice on how to bake the best loaves. I'm not quite there yet but I will keep trying. **Alvaro**, it was fun to show you how the attocube works. You learn quickly and your jokes make it a pleasure to work with you. **Riccardo**, it was great to work with you on the MCBJs. You are always trying to completely understand how things work and your joyfulness makes it great to be around you. **Linde**, your jokes made the group meetings a bit more bearable. **Daan**, je was een fijne student om te begeleiden. Je bent een extreem harde werker en was al snel in staat om zelf te beslissen wat logische stappen waren om te nemen. Veel succes in de rest van je carrière.

There were also some people from outside the group to whom I want to express my gratitude. **Tino**, thank you for all the help over the years. Whenever the attocube had issues again I could always count on you. My officemates, **Jan and Harmen**, thank you for the conversations, for the nice atmosphere and for the help.

Among the cleanroom staff there were a few people whom I regularly had contact with and got help from. **Eugene**, over the years you have helped me more times than I can count. **Bas**, you were helping Jacqui with the fabrication process when I also came into the picture. Over the years I could always count on you for help and for ideas. **Brian**, anytime I had a problem or a question I could come to you. I also want to thank the staff that I had less interactions with, but who have helped me nonetheless, **Mark, Charles, Roald, Marinus, Hozanna, Lodi, Arnold, Anja, Ewan and Esther**.

The people from DEMO also deserve a special thanks. **Jack, Erik and Yannick**, you helped me with putting together the SPI rack for the attocube setup. Without your advice and help I could not have done this. You were always ready to help, it didn't matter whether it was a module that needed to be calibrated or whether the soldering of one of our sticks needed to be redone. Thank you for all the help and conversations during my time here.

Finally, I would like to thank my family and friends. **Emma**, bedankt voor de afgelopen jaren. Je bent er altijd om mij te steunen als ik het even moeilijk heb en om lekker gek mee te doen. Ik hoop op nog vele mooie jaren en trips naar de bergen. **Papa, mama en Tijmen**, jullie zijn er altijd wanneer ik jullie nodig heb. Bedankt voor alle steun en motivatie door de jaren heen en voor het gevoel dat ik met jullie over alles kan praten. **Bas, Flo en Am**, jullie zijn me extreem dierbaar. Bedankt voor alle gesprekken, avonden dat we spelletjes speelden en trips naar

Schotland. **Storm**, bedankt voor de vele slechte grappen, de spelletjesavonden, de PoE sessies, maar ook de goede gesprekken. **Emma MEP**, we raakten bevriend tijdens onze masterprojecten. Ik heb veel goede herinneringen aan de vele piano, yoga en zelda sessies die we door de jaren heen hebben gehad. **Henk**, bedankt voor de leuke discussies en de vele whiskies, biertjes en burgers. Tot slot wil ik graag de vele mensen bedanken die hier niet genoemd zijn, maar die de afgelopen jaren wel een rol hebben gespeeld in mijn leven.

Curriculum Vitae

Tristan Bras

25-01-1996 Born in Amsterdam, The Netherlands.

Education

2008–2014 VWO
St. Michael College, Zaandam, The Netherlands

2014–2018 Bachelor of Science in Applied Physics
Delft University of Technology, Delft, The Netherlands
Thesis: Quantum Dynamics of Excitons in Organic Photovoltaic Interfaces
Supervisors: Prof. dr. F. C. Grozema
Dr. M. B. Fridriksson

2018–2020 Master of Science in Applied Physics
Delft University of Technology, Delft, The Netherlands
Thesis: Quantum Interference in Mechanosensitive Molecules
Supervisors: Prof. dr. ir. H. S. J. van der Zant
Dr. C. Hsu

2020–2025 PhD. Physics
Delft University of Technology, Delft, The Netherlands
Dissertation: Contacting Magnetic Nano-Objects for Quantum Transport Measurements
Promotors: Prof. dr. ir. H. S. J. van der Zant
Prof. dr. F. C. Grozema

List of Publications

2. **T. Bras**, C. Hsu, T. Y. Baum, D. Vogel, M. Mayor, H. S. J. van der Zant. *Mechanically Stable Kondo Resonance in an Organic Radical Molecular Junction*, *J. Phys. Chem. C* **129**, 6, 3152–3157 (2025).
1. T. S. Ghiasi, D. Petrosyan, J. Ingla-Aynés, **T. Bras**, K. Watanabe, T. Taniguchi, S. Mañas-Valero, E. Coronado, K. Zollner, J. Fabian, P. Kim, H. S. J. van der Zant. *Quantum Spin Hall Effect in Magnetic Graphene*, under review, available on [arXiv](#).